Neurotechnology for multiplexed interrogation of brain circuits and synaptic activity

Thesis by

Alice Hsu

In Partial Fulfillment of the Requirements for the

Degree of

Doctor of Philosophy

CALIFORNIA INSTITUTE OF TECHNOLOGY

Pasadena, California

2023

(Defended May 30, 2023)

Alice Hsu

ORCID: 0000-0001-6609-2559

ACKNOWLEDGMENTS

I would like to first and foremost thank my advisor, Professor Michael Roukes, for all his guidance, advice, expertise, motivation, and patience during the course of my PhD study and research. I would like to give a special thanks to Professor Lin Tian for her support and insight during the microfluidics project and Professor Kenneth Shepard for his help and expertise with interposer design and ephys assembly packaging.

I would like to give my sincere thanks to Dr. Laurent Moreaux, Dr. Warren Fon, Dr. Jessica Arlett, Zachary Blumenfeld, Guilia Cifani, Tracy Mikuriya, Nancy Roth-Rapport, Avedis Tufenkjian, and Dr. Nicole Kubat in the Roukes group for their help. I especially thank Dr. Laurent Moreaux for all his guidance and collaboration with the two-photon system and animal work throughout the neural probe project. I would like to thank Dr. Warren Fon for all his guidance with printed circuit board (PCB) designs, neural probes, and assemblies. I would also like to thank Nikki Tjahjono, Yihan Jin, and Dr. Ruqian Liang in the Tian group for all their advice with the microfluidic project and help with the synaptic glutamate reporter. I also thank Eric Hiroshi Pollmann and Abhinav Parihar for their help with the 256-channel assemblies and interposers.

Besides my advisor, I thank the rest of my committee: Professor Lin Tian, Professor Kai Zinn, and Professor Henry Lester for their advice and insightful questions. I also thank the Center for Molecular Medicine (CMCM) center and its members Dina Malounda, Kun Miao, and Kelsey Boyle for allowing me to use the cell culture facilities and for their help. I would also like to thank the Biological Imaging Facility (BIF) and Dr. Andres Callazo and Dr. Giada Spigolon for training me on the confocal microscopes. Finally, I thank my parents and sister for all their encouragement and support during my graduate studies.

ABSTRACT

This thesis describes the development of neural technologies for 1) multiplexed brain circuit electrophysiology (ephys) recordings and control of activity in optogenetic mice lines with concurrent recording paired with two-photon imaging and 2) multiplexed measurements of synaptic release events in microfluidic platforms. The first part of this thesis describes efforts to provide deterministic correlation of excited neuron action potential with resulting ephys recordings *in vivo.* This consisted of technological development of novel, high density multisite silicon probes for electrophysiology recordings *in vivo*. The probes consist of four columns of electrodes densely packed at the shank tip. This density of electrode arrays allowed for higher resolution isolation of more distinct waveforms than previous ephys probes and benchmarking measurements to triangulate the locations of emitting neurons. These measurements help benchmark the ability of existing silicon extracellular probes to capture surrounding extracellular activity. When combined with two-photon imaging, we can simultaneously record ephys activity, image the probe and surrounding brain, quantify brain damage during probe implantation, and control neural activity using optogenetic mouse lines.

The second project described development of a microfluidic platform to monitor synaptic release of the neurotransmitter glutamate. Microfluidic devices were used to isolate synaptic processes expressing synaptic reporters and provide targeted recording of glutamate activity across the synapse. Synaptic glutamate release was monitored with a two part genetically encoded fluorescent reporter that detects glutamate released at the synapse, called split-iGluSnFR, developed in Professor Lin Tian's lab at UC Davis. We designed new microfluidic devices to better isolate neuron processes with split-iGluSnFR and be

compatible with existing fluorescent complementary metal–oxide–semiconductor (CMOS) contact imagers. Using computational fluid dynamic simulations, we demonstrate efficient perfusion in the device. The form factor of this new device is designed to be compatible with CMOS contact imagers, and that when combined will help us achieve our ultimate goal to monitor the kinetics of simultaneous synaptic release events modulated by perfused neuromodulating drugs.

PUBLISHED CONTENT AND CONTRIBUTIONS

Tjahjono, N., Jin, Y., Hsu, A., Roukes, M., & Tian, L. (2022). Letting the little light of mind shine: Advances and future directions in neurochemical detection. Neuroscience Research, 179, 65–78. https://doi.org/10.1016/j.neures.2021.11.012

A.H. contributed to writing and tables in this review.

Peng, S., Zaretsky, J. M., Ng, A. H. C., Chour, W., Bethune, M. T., Choi, J., Hsu, A., Holman, E., Ding, X., Guo, K., Kim, J., Xu, A. M., Heath, J. E., Noh, W. J., Zhou, J., Su, Y., Lu, Y., McLaughlin, J., Cheng, D., … Heath, J. R. (2019). Sensitive detection and analysis of neoantigen-specific T cell populations from tumors and blood. Cell Reports, 28(10), 2728-2738.e7. https://doi.org/10.1016/j.celrep.2019.07.106

A.H. contributed to experiments performed in this study.

Evans, C. J., Olson, J. M., Mondal, B. C., Kandimalla, P., Abbasi, A., Abdusamad, M. M., Acosta, O., Ainsworth, J. A., Akram, H. M., Albert, R. B., Alegria-Leal, E., Alexander, K. Y., Ayala, A. C., Balashova, N. S., Barber, R. M., Bassi, H., Bennion, S. P., Beyder, M., Bhatt, K. V, … Banerjee, U. (2021). A functional genomics screen identifying blood cell development genes in Drosophila by undergraduates participating in a course-based research experience. G3 Genes|Genomes|Genetics, 11(1). https://doi.org/10.1093/g3journal/jkaa028

A.H. contributed to experiments performed in this study.

Contributions: electrophysiology recording system, setup, and specification: Alice Hsu, Laurent Moreaux, Warren Fon, and Michael Roukes; neural probe design: Warren Fon; PCB component design and assembly: Alice Hsu with input from Michael Roukes, Warren Fon, and Laurent Moreaux; AutoCAD EAGLE PCB schematics and designs: Alice Hsu, polyimide flexicable design: Warren Fon; interposer design: Abhinav Parihar, Warren Fon, and Alice Hsu; system packaging: Alice Hsu; system electroplating: Alice Hsu; build of 256-channel assembly: Eric Hiroshi Pollmann; system bench-top evaluation and electrical characterization: Alice Hsu; Autocad Fusion 3D modeling: Alice Hsu and Guilia Cifani, *in vivo* experimental protocols: Laurent Moreaux and Alice Hsu; AAV protocols and AAV vector and mouse strain selection: Laurent Moreaux, Nicole Kubat, and Alice Hsu; surgery: Alice Hsu and Zachary Blumenfeld; animal work, AAV delivery, and surgery: Alice Hsu; system *in vivo* evaluation: Alice Hsu, Laurent Moreaux; two-photon microscopy: Laurent Moreaux, Alice Hsu; histological processing of brains: Alice Hsu; split-iGluSnFR AAV and capsid packaging: Ruqian Liang, Yihan Jin, and Nikki Tjahjono; microfluidic design and simulations: Alice Hsu with input from Nikki Tjahjono and Lin Tian; writing and figure preparation: Alice Hsu with input from Michael Roukes and Laurent Moreaux.

Acknowledgements: We thank Ken Shepard, Eric Hiroshi Pollmann, and Abhinav Parihar at Columbia University for design of the interposer and foundry fabrication at TSMC. Multisite silicon neural probe foundry fabrication was carried out at CEA/LETI, Grenoble under the aegis of the Alliance for Nanosystems VLSI.

Project Background: Alice Hsu carried out research on the multisite silicon neural probe project in the group of Michael Roukes and research on the microfluidic project in the group of Lin Tian.

TABLE OF CONTENTS

Acknowledgments iii
Abstract iv
Published Content and Contributions vi
Table of Contents viii
List of Illustrations xii
Chapter 1: Introduction 1
1.1 Motivation 1
1.2 Review of multisite silicon neural probes for electrophysiology and microfluidic devices for imaging synapses 2
1.2.1 Electrophysiological recordings using multisite silicon neural probes 2
1.2.2 Microfluidic platforms for isolating and imaging synapses glutamate release with contact imager 4
1.3 Thesis Overview 5
Chapter 2: Theory and Assembly Packaging Considerations 9
2.1 Introduction 9
2.2 Probe and assembly design considerations 9
2.3 Mechanical design of the probe 9
2.3.1 Probe Geometry 9
2.3.2 Shank deformation under insertion 10
2.4 Electrical design of the probe 12
2.4.1 Probe wiring and interconnect parasitics 12
2.4.2 Maximizing signals 13
2.5 Biological and biocompatibility design considerations 14
2.5.1. Neural probe considerations 15
2.5.1.1 Parylene for biocompatibility, biostability, and sterilization 15
2.5.1.2 Minimizing damage 15
2.5.1.3 Rodent neural probe: Experimental constraints for brain insertion 16
2.5.1.4 Non-human primate (NHP) neural probe 17
2.5.2 Passive printed circuit board (PCB) connecting board bonded to rodent neural probe 17
2.5.2.1: 32-channel acute assemblies 18
2.5.2.2 256-channel assemblies 19
2.5.3. Flexicable considerations: Polyimide flexicable for chronic recordings and decoupling head motion 19
2.5.4 Headstage and DAC considerations 20
2.6 Conclusion 21
Chapter 3: Neural Probe Fabrication 22
3.1 Introduction 22
3.2 Neural probe fabrication steps 23
3.2.1 Substrate SOI wafer (1) 24
3.2.2 Bottom insulator layer (2) 24
3.2.3 Metal interconnect (3) 24
3.2.4 Top insulator (4-5) 25

3.2.5 Electrode and interface pads (6) 25
3.2.6 Top side device definition (7) 26
3.2.7 Biocompatibility coating (8) 26
3.2.8 Back side device definition (9-11) 26
3.3 Conclusion 27
Chapter 4: Assembly, Packaging, and Electrical Characterization 28
4.1 Introduction 28
4.2 32-channel assemblies 28
4.3 256-channel assemblies 30
4.4 Electroplating 33
4.5 Electrical characterization 34
4.6 Conclusion 36
Chapter 5: *In vivo* Recording Setups with Imaging Systems 38
5.1 Introduction 38
5.2 Animal procedures 39
5.3 Surgical procedures 40
5.4 Description of setups 40
5.4.1 Setup 1: Quick probe testing with adjustable levels of anesthesia 40
5.4.2 Head-fixation strategy imaging setups (for setup 2 and 3) 41
5.4.2.1 Head-fix piece attachment procedure 43
5.4.2 Setup 2: Confocal imaging with probe insertion 44
5.4.3 Setup 3: Two-photon imaging with simultaneous e-phys probe recording 44
5.4.3.1 Two photon considerations: imaging at depth 44
5.5 Acute *in vivo* recording set-ups 45
5.6 Demonstration of successful imaging of neural probe and surrounding neurons *in vivo* 47
5.7 Data acquisition workflow 51
5.8 Conclusion 51
Chapter 6: Mapping Neurons with Juxta-Positional Recordings Combined with Two-Photon Imaging *in vivo* 53
6.1 Introduction 53
6.2 Theoretical distance dependence of extracellular measurements 53
6.3 Quality of ephys recording and mapping of neuron locations in literature 55
6.3.1 Importance of site density to spatially sample individual neurons 57
6.3.2 Benchmarking spike and recording quality 58
6.3.3 Examining drift of probe relative to brain during recording 58
6.3.4 Temporal filtering and spatial whitening 61
6.3.5 Spike recording and waveform quality 63
6.3.6 Single unit isolation with dense electrode array neural probes 63
6.3.7 Detection limits of electrodes 70
6.4 Extracellular recording combined with two-photon imaging 73
6.5 Conclusion 73
Chapter 7: Quantification of Probe Invasiveness using Vasculature and Neuron Staining *in vivo* 75
7.1 Introduction 75

7.2 Invasiveness of probe insertion 76
7.2.1 Traditional methods of accessing probe damage and limitations 77
7.2.2 Why measure tissue damage in vivo 77
7.2.1.1 Intravascular staining for examining tissue damage *in vivo* 78
7.3 Evidence of minimal invasiveness of probe insertion 82
7.3.1 Vasculature stain during probe implantation and probe removal 82
7.3.2 Time-series during probe implantation 84
7.3.3 Neuron displacement 85
7.4 Vasculature modeling and damage quantification 87
7.4.1 Quantification of vasculature displacement 90
7.4.2 Visualization of vasculature displacement caused during probe insertion 92
7.4.3 Examination of vasculature and morphological changes over time during probe implantation 92
7.5 Conclusion 94
Chapter 8: Channelrhodopsin Mice Lines for Deterministic Control of Neuron Activity and Benchmarking of Neural Probes 96
8.1 Introduction 96
8.2 Why channelrhodopsin? 96
8.3 The importance of sparse channelrhodopsin labeling 97
8.4 Why label GABAergic interneurons (with *Gad2* expressing promoter) 97
8.4.1 GABAergic interneuron expressing channelrhodopsin line: Gad2-IRES-Cre infected with Cre-activated AAV expressing humanized ChR2 98
8.4.2 Intravenous viral infection with retro-orbital injection 100
8.4.2.1 Histology: Examination of expression sparsity in channelrhodopsin mice lines 101
8.4.2.2 Confocal imaging of fixed brain slices 101
8.4.3 Gad2-IRES-Cre infected with Cre-activated AAV expressing humanized ChR2 102
8.4.4 VGAT-ChR2-EYFP 103
8.5 Two-photon imaging of optogenetic models and neural probe ephys recording 104
8.5.1 Light delivery method 105
8.5.2 Imaging with ephys recording 108
8.5.3 Photo-electric effect of two-photon absorption on probe surface 111
8.5.4 Ephys recording of channelrhodopsin models under two-photon imaging 112
8.6 Limitations 114
8.7 Silencing spiking activity with blue light LED in VGAT mice 115
8.8 Future Directions: GCaMP6 lines with probe recording and two-photon imaging. 118
8.9 Conclusion 118
Chapter 9: Microfluidic Platform for Measuring Synaptic Glutamate Release and Response to Neuromodulating Drugs 120
9.1 Introduction 120
9.2 Split-iGluSnFR sensor for detecting synaptic glutamate release 120
9.3 Microfluidic design to isolate synaptic processes 124
9.3.1 Fluid isolation in microchannels for compartmental viral infection of pre and post-iGlu components 124

9.3.1.1 Infecting pre-iGlu and post-iGlu expressing neurons into separate compartments 127
9.3.2 Improving neuron viability in microfluidic devices 128
9.3.2.1 Reduced evaporation in microfluidic device for improved neuron health 128
9.3.3.2 Device coating to increase neuron adhesion 129
9.3.3 Sparse split-iGluSnFR reconstitution along microchannels 130
9.3.4 Decreased microchannel length for increased neurite compartmentalization and infiltration 131
9.4 New microfluidic design: revised microchannel lengths for axons and dendrites and central chamber for reconstituted synapses and perfusion 132
9.4.1 Simulation of perfusion in microfluidic design 134
9.4.1.1 Particle path predictions using simplified glass, open-surface microfluidic design 136
9.4.1.2 Fluid simulations in glass device 139
9.4.1.3 Particle flow simulation 139
9.4.1.4 Velocity of particle pathlines 141
9.5 Future directions 142
9.6 Conclusion 143
Chapter 10: Conclusion 145
10.1 Comparison with previous work 146
10.2 Future directions 148
Bibliography 149

LIST OF ILLUSTRATIONS

Number		*Page*
2.1	**Picture of rodent probe and dimensions.** Shank tip was thinned to a thickness of 20 μm. Pads were spaced apart 20 μm horizontally and 14 μm vertically. Rodent probes were designed by Dr. Warren Fon ……	16
2.2	**Non-human primate probe dimensions**. The probe tips of various probe designs are shown ……..……	17
2.3	**32-channel passive PCB connecting neural probe.** a) Dimensions listed in mm of 32-channel acute PCB. b) Acute 32-channel PCB board. c) Acute board with rodent neural probe mounted to PCB. Neural probe is electrically connected to PCB via wire bonds and encapsulated with epoxy (clear brown) ……	18
2.4	**Polyimide flexicable.** a) Dimension of flexicable in mm. b) Ball bumps on either end of flexicable. Image credits: Warren Fon…….	20
3.1	**Neural Probe Fabrication Steps.** Figure modifed from (Rios et al., 2016)……...	27
4.1	**32-channel rodent assembly with holder mounting to micromanipulator.** The holder is designed to insert into a rod (through the hole at its base). This rod was then mounted to the micromanipulator. *Left:* Actual assembly with rod that mounts to micromanipulator on bottom…….	30
4.2	**256-channel passive PCB connecting rodent neural probe**……	31
4.3	**256-channel assembly connecting non-human primate (NHP) probe assembly**…….	31
4.4	**256-channel rodent probe assembly** ……..……..……	32
4.5	**256-channel non-human primate probe assembly**…….	33
4.6	**Neural probes with unplated and plated sites.** a) Plated (*black*) and unplated (*yellow*) sites. b-c) Scanning electron microscope images of neural probe shank with unplated and plated sites. Roughened surface indicated the deposition of the nanoporous gold layer during plating. The parylene layer is shown as a smooth, light, gray layer around the electrode pads…….	34
4.7	**Electronic characteristics of Caltech/LETI probe.** a) Impedance measured at various frequencies of neural probe electrode sites before (orange) and after (blue) electroplating. b) Decrease in input noise (μV_{RMS}) as measured from 3 Hz to 10 kHz bandwidth after electroplating. Plot of impedance measured at 1 kHz versus input noise. Electroplated sites are shown as blue dots and unplated sites are shown as red dots. …….....	35
5.1	**Recording setups**……...	39
5.2	**Recording setup.** Probe with amplifier board mounted to holder connected to micromanipulator. The amplifier board is connected to a	

recording controller for recording and visualization of electrophysiology signals ……... 41
5.3 **Headfix piece.** a) Dimensions of headfix piece. b) Attachment of headfix piece to skull and microscope platform…….. 43
5.4 **Widefield imaging with ephys probe**……... 44
5.5 **Model of two-photon setup with inserted ephys probe.** Mouse skull is shown in purple. Setup enables simultaneous ephys recording with two-photon imaging…… 46
5.6 **Two-photon imaging setup with mouse during imaging.** a) Two-photon imaging setup with ephys probe inserted under imaging window. b) Side view with probe's shank inserted shallowly under coverslip. c) View down probe shank inserted under coverslip…… 47
5.7 **Insertion of probe into cortex**. a) Position of inserted probe in mouse brain represented by Mouse Brain Atlas (Franklin & Paxinos, 2008). b) Image of probe inserted into brain under coverslip……. 47
5.8 **Representative image of ephys probe with stained neurons.** Electroplated pads appear red and surrounding interneurons expressing GFP are white. Images were obtained via 2P setup *in vivo* when neural probe was inserted into Layer 1 of the cortex. Figure credit: Laurent Moreaux ……..... 49
6.1 **Minimal electrode drift during recording.** a) Drift map of spikes over time as dots mapped by spatial depth. Larger amplitude spikes shown as darker dots. b) Spikes batches have minimal spatial drift $< \pm 15$ μm over the course of the recording…….. 59
6.2 **Drift correction to sorting.** a-b) Drift map and correction applied to spiking output (using Kilosort)…… 61
6.3 **Temporal filtering and spatial whitening.** a) Temporal filter to whiten data. Spatial matrix for whitening of 32 electrodes. b) Amplitude of each spike cluster unit versus spike count for each amplitude……. 62
6.4 **Spike recording from consecutive recording sites of nanoprobe.** a) Broad-band (1 Hz-10 kHz) filter of LFP signal. Channels are ordered by their position on the probe (with top traces located at the probe tip and bottom traces located towards the probe base). b) Spike frequency (300 Hz - 10 kHz) filtered signal of the same recording. ……. 63
6.5 **Multiple spike waveforms measured on one electrode pad**. a) Overlay of spike waveforms from different cluster units on electrodes. b) Principal component analysis (PCA) features of selected waveforms shown in a). Individual graphs show relevant channels (shown by numbers). A, B, and C refer to the first, second, and third (respectively) dimensions of the principal components. …… 65
6.6 **Example waveforms clusters units recorded across each channel.** Waveforms from individual neurons detected across multiple electrode sites. Spike sorting was performed using Spyking-Circus and results were visualized and validated on phy (x-axis is time in μs)……. 66

6.7 **Single unit isolation.** Analysis performed with Spyking-Circus sorting. a) Annotated recording electrodes of neural probe pads. b) Representative mean waveforms for putative single neurons on each channel. Each waveform cluster is represented with a different color…. 67

6.8 **Neuron units isolated per electrode.** a) Plot of mean waveform for all isolated neuron units plotted by electrode position on the neural probe. b) Box and whisker plot of neuron units isolated on each electrode. With our probe, we detected a maximum of 5-18 putative neurons isolated on each electrode pad. c) Mean waveform of each isolated neuron on one electrode site. On this pad, we detect 18 distinct neuron units…… 68-69

6.9 **Single unit isolation and limits of detection.** Analysis performed with Spyking-Circus sorting. a) Annotated electrodes on nanoprobe pads. b) Representative mean waveforms for putative single neurons on each channel. Each waveform cluster is represented a different color. c) Overlay of representative mean waveforms for seven putative single unit neurons. d) Three neuron units with mean waveforms plotted on electrode. Each waveform cluster is colored by its putative neuron unit. Arrows point from the reference electrode (highest amplitude waveform) closest to neuron to furthest detecting electrode. e) Maximum detection range of neural probe plotted by their cumulative distribution. f) Maximum detection range histogram plotted by number of single units detected at each range…….. 71-72

6.10 **Single unit isolation mapped to probe and surrounding labeled neurons.** a) Two-photon imaging of GFP labeled interneurons (*white*) in the cortex with the probe (pads shown as red). b) Annotated neural probe with electrode pad sites numbered by their position. c) Spikes labeled in accordance with the electrode position……. 73

7.1 **Staining of cerebral vasculature with Texas Red Dextran (70,000 MW, neutral charge) *in vivo* with two photon imaging.** a) Maximum projection of top surface to 320 μm below surface. b) Cross-sectional view of vasculature stain across depth. Frames are 5 μm apart in the z-direction. c) Maximum projection of vasculature stain color coded by depth in z-stack…… 80-81

7.2 **Vasculature during and after probe insertion and removal.** Max projection of vasculature around probe 105 μm above and 50 μm below probe). First slice of stack begins at 125 μm and ends at 280 μm below pial surface. a) Vasculature staining around probe during implantation. Probe and vasculature shown in red. b) Vasculature after probe is removed (*green*). c) Composite overlay of vasculature projection during probe implantation and after probe removal……. 83

7.3 **Side view of vasculature during and after probe implantation**. a) Cross section of vasculature during probe implantation. Red arrow indicates position of the probe. Reflection of laser across gold electroplated electrodes on the probe leads to the horizontal white

object. b) Cross-section of vasculature after probe removal. The red arrow indicates area where the probe use to be implanted……. 84

7.4 **Time series of probe inserting into vasculature.** a) First frame in the time series (time 0). b) Last frame (after approximately 137 μm removal). c) Timeseries of probe removal with frames color coded by color map. Frames were taken at 0.74 frames per second …… 85

7.5 **Neuron cell body location before and after probe insertion** (*overlay*). a) Position of neurons during probe implantation (red). b) Neurons after probe removal (white). c) Overlay of neuron positions during probe implantation and after probe removal. Outline of probe shown in dashed yellow lines.…… 86

7.6 **Vesselness filtering for segmenting vasculature for 3D modeling.** Slice in z-stack of vasculature staining (*white*) taken at 130 μm below pial surface (*left image*). Areas recognized as a vessel by the filter are shown in red (*right image*). Vesselness was filtered on each slice of the stack…… 87

7.7 **Model of vasculature in wild-type mouse.** Model is derived from a C57BL/6 mouse brain with brain vasculature stained with Texas-red dextran. 3D rendering performed in 3D slicer and derived from vesselness filtering. a) Side view. b) Top view from dorsal (top) to ventral (bottom)……... 88

7.8 **Model of vasculature during probe implantation and after probe removal.** Outline of probe is shown with dashed lines. Vasculature model during probe implantation is shown in red. Vasculature after probe removal is shown in green. a) Cross sectional view (posterior facing outwards to anterior). b) Dorsal to ventral view (from brain surface towards deeper layers). c) Ventral to dorsal view. d) Side view… 89-90

7.9 **Histogram of vector magnitude displacement between probe implantation and removal models.** a) Bin set to 5 μm. b) Bin size reduced to 0.2 μm……... 91

7.10 **Model to model distance output showing points sampled along the model during analysis and corresponding displacement between models.** a) Orientation of brain vasculature b) Output displacement model with orientation shown with arrows and indicated as follows: dorsal (D), ventral (V), anterior (A), and posterior (P). c) Zoom-in of displacement models with points along the surface color code by their displacement between models……. 91

7.11 **Color map of displacement in vasculature system between probe implantation and removal**. Absolute displacement is measured in units of mm and color coded. At most points there is little displacement (below 20 μm) ……..... 92

7.12 **Displacement of surrounding structures following apoptosis of damaged neuron.** Temporal color coding of each frame in the time series. Each frame was taken after a second. a) Neuron staining. b) Vasculature staining…… 94

8.1 **Channelrhodopsin model and infection strategy for sparsely labeled cortical GABAergic interneurons**……..... 99

8.2 **Distribution of hChR2-eYFP (yellow) labeled GABAergic interneurons in fixed slices infected with various viral titers.** a) Mouse infected with PHP.eB with $5x10^{11}$ vg of AAV through retro-orbital injection (P52). Virus incubation time 21 days b) Mouse infected with 3 x 10^9 vg PHP.eB for 52 days…… 102

8.3 **Cortical distribution of GABAergic interneurons labeled in VGAT transgenic line.** Images taken from fixed cortical brain slice. GABAergic interneurons were labeled with EYFP (*yellow*)…… 104

8.4 ***Gad2-IRES-Cre* infected with $3x10^9$ vg PHP.eB AAV under two-photon imaging**. Maximum intensity projection of layer 1 cortex (obtained from z-stack spanning the surface to 565 μm below the surface) ……. 107

8.5 **ChR2-eYFP cortical expression in VGAT mice line *in vivo***. Expression is shown for the Layer 1 mouse cortex using two-photon imaging *in vivo*. Darker areas are from blood vessels…… 108

8.6 **Neural probe inserted in *Gad2-IRES-Cre* infected with AAV-PHP.eB injected intravenously**. ChR2 labeled with EYFP is in white and electroplated pads are red. A viral titer of $3x10^{10}$ vg per mouse was used …… 110

8.7 **Neural probe inserted in VGAT transgenic line**. VGAT interneurons expressing ChR2-EYFP are white and electroplated pads are red…… 111

8.8 **Photoelectric effect from two-photon on nanoprobe.** a) Photoelectric artifacts in spike frequency bandwidth (300 Hz - 10 kHz). b) Zoom-in of biphasic wave from two-photon absorption detected on electrodes…… 112

8.9 **Channelrhodopsin PHP.eB transfected Gad2-IRES-Cre mice**…… 113

8.10 **VGAT line with corresponding waveforms ordered by position on electrode**…… 113

8.11 **Blue light induced silencing in consecutive recording sites of spike bandwidth.** Times when blue LED was applied are indicated by blue bars. a) Spike frequency bandwidth (300 Hz - 10 kHz). b) Spike raster… 117

8.12 **Spikes during blue light and without widefield blue light exposure.** Blue dotted box shows spikes, possibly from activated interneuron, when widefield blue light was applied. Red dotted box shows spikes, possibly from pyramidal neurons, where blue light was not applied……. 118

9.1 **Cartoon of split-iGluSnFR parts and synaptic glutamate detection**. a) The two parts of the split-iGluSnFR are labeled pre-iGlu and post-iGlu. Each part consisted of the one half of the glutamate binding protein and cpGFP. b) At the synapse, the pre and post parts of the split-iGluSnFR are brought close together, bringing the beta-barrel close enough that it is distorted but able to fluoresce dimly. c) In the presence of glutamate, the glutamate binding protein binds to the glutamate,

which induces a conformational change that restores the beta-barrel increasing the fluorescent brightness ……. 122

9.2 **Primary hippocampal neurons expressing split-iGluSnFR.** Reconstituted synaptic glutamate sensor (consisting of a post-synaptic and pre-synaptic glutamate sensor) are shown as green puncta (a-b). Cells expressing the post-synaptic component of the split-iGluSnFR sensor are shown in red. a-b) Primary hippocampal neurons expressing split-iGluSnFR. c) Fluorescence of split-iGluSnFr expressing neurons in media with 0 mM glutamate. d) Reconstituted split-iGluSnFR (green) fluorescent increases with addition of glutamate…… 123

9.3 **Microfluidic design for separating synapses and pre-iGlu and post-iGlu infections**. a) Microfluidic device consisting of separate chambers where neurons are infected with either pre-iGlu or post-iGlu sensor. b) Microchannels in device are just wide enough to allow processes to infiltrate and not cell bodies. This allows the synapses to form within microgrooves and be isolated in one part of the device for imaging. c) Along microchannels, reconstituted split-iGluSnFR can be viewed as green puncta…… 124

9.4 **Pressure head used to isolate volumes into compartments in microfluidic-based neuron platform.** A volume difference between the compartments allows isolation of solutions. A higher volume of solution in the middle chamber (red dye) creates a high fluidic resistance across the microgrooves preventing solution from the side (blue dye) from escaping. Volume difference can be reversed to allow for isolation of solutions to the opposite compartments. Fluid isolation test was demonstrated on XonaChip three-chamber device (XC-T500). a) A higher volume (150 μL) of red dye was added to the middle chamber and lower volume (120 μL) of blue dye to left and right chambers. b) After 24 hours, no dye entered from lower volume chambers (blue) into the middle red chamber indicating successful fluid isolation…… 126

9.5 **Fluid isolation in device.** Middle chamber had higher pressure head from volume differential and prevented neighboring solutions (red and green) from escaping chambers. The red solution was EtD-III (dead cell stain) and the green solution was calcein AM (a viability stain) that stained viable cells green …… 127

9.6 **Split-iGluSnFR infection strategy in microfluidic devices.** Post-iGlu infection chambers are red and pre-iGlu infection chambers are green…. 128

9.7 **Effect of PDL incubation time on neuron adhesion.** a) Neuron clumping. b) Single layer neuron growth…… 130

9.8 **Reconstitution along microchannels.** Cartoon of neurites captured in microchannels with reconstituted sensor (*left image*). Image of two microchannels with post-iGlu labeled processes (*red*) and reconstituted split-iGlu sensor (*green puncta*) (*right image*). Channels were 500 μm long……. 131

9.9 **Dendrite compartmentalization in microchannels with 150 μm.** a) Bright field of device and microchannels. b) Neuron staining with viability (green, calcein AM) and dead (red, EtD-III) cell stain. c) Zoom-in of dendrites infiltrating microchannels……. 132

9.10 **Revised microfluidic design.** a) Model of microfluidic device. Open cell chambers are created with a biopsy punch. b) Enlarged view of microchannels. Synaptic reconstitution chamber is 250 μm wide…….... 133

9.11 **Preparing microfluidic device for Ansys simulation.** a) Imported geometry of microfluidic design into Ansys program. b) Mesh generated for simulations……. 135

9.12 **Fluid path and pressure simulations**. a) Inlet port is annotated with blue arrows pointing inwards. Outlet port is annotated with red arrows radiating outwards. b) Simulation of pressure during perfusion……. 136

9.13 **Glass microfluidic device with thin coverslip bottom.** a) Fabrication and assembly of glass microfluidic device. b) Dimensions of device. Compartment chambers are 1 mm high…… 138

9.14 **Particle flow pathlines in device.** a) Top-down view. b) Side view…. 140

9.15 **Pressure contours in simplified glass model.** a) Static pressure. b) Absolute pressure…… 141

9.16 **Velocity path and magnitude (in m/s) of particles perfused through central reconstitution chamber.** a) Outline of device shown with mesh and velocity magnitude of perfused particles color mapped. b) Velocity vectors with device mesh removed…… 142

9.17 **Integrated microfluidic platform with CMOS contact imager for monitoring kinetic release of glutamate.** Microfluidic platform will consist of microfluidic device described in this chapter. Light from the excitation light will pass through the microfluidic device onto neuron cells expressing the split-iGlu sensor. Emitted fluorescent signal from the reconstituted sensor will then pass through a filter removing the excitation light and the remaining emitted light from the sensor will detected by a fluorescent contact imager. Contact image sensors will be placed along the microchannels or chambers were the processes join to form synapses ……. 143

Chapter 1

INTRODUCTION

1.1 Motivation

Brain activity, such as perception, learning, and memory, depends on the coordinated interactions between neuron ensembles. Extracellular electrodes and patch clamps remain the gold standard for monitoring brain activity since they directly measure electrical activity with high temporal resolution and sensitivity (Buzsáki et al., 2015; Kipke et al., 2008). While major progress has been made in understanding the electrical response of individual cells, circuit interactions remain poorly understood. Fundamental difficulties include understanding how many neurons in a specific volume each electrode can record, isolating each neuron's individual waveforms, and deterministically correlating spike activity to the location of each neuron relative to the probe. Research data correlating electrophysiology (ephys) signal to the distance of the neuron from the probe is limited. A theoretical distance can be estimated based on simplified assumptions that extracellular recorded spikes emanate from a point source rather than from the actual complex geometry of the neuron, where every part of the neuronal membrane can generate action potentials (Buzsáki, 2004).

To achieve our goal of benchmarking the detection limits of our multisite silicon neural probe, we developed a new assembly consisting of an ephys probe with the dense 256 electrode arrays and an imaging setup that allows for concurrent imaging of the probe relative to the *in vivo* neural tissue during ephys recordings. This dense, large-scale recording and stimulation of brain activity enables us to simultaneously record from multiple neurons at a time, discriminate multiple waveforms across densely spaced pads, and determine the

detection limits of our neural probe. Additionally, combining extracellular ephys recording and two-photon imaging allows for better quantification and benchmarking of *in vivo* insertion damage and control of surrounding neuron activity using optogenetic transgenic mouse lines.

1.2 Review of multisite silicon neural probes for electrophysiology and microfluidic devices for imaging synapses

1.2.1 Electrophysiological recordings using multisite silicon neural probes

Electrophysiological recordings play a vital role in elucidating neural circuits. A major challenge that remains is recording neuronal activity at large scale. Some difficulties in achieving this are providing stable recordings with minimized tissue damage; some possible solutions to minimize damage are to design flexible neural probe shanks (Luan et al., 2017) or to miniaturize the shank width to <10 μm in size (Welle et al., 2020). Chronic recordings in rodents pose additional difficulties such as the need to minimize impediments during head movement, which necessitates the development of small probes (Juavinett et al., 2019). Scaling up the number of recording sites while maintaining a miniaturized profile made of biocompatible materials creates several design constraints during probe fabrication.

To address these issues, we describe a novel multisite silicon neural probe. The use of silicon allows us to utilize developments in semiconductor fabrication to create features at the micro and nanoscale necessary for fabrication of the dense electrode arrays on our narrow probe shanks. Miniaturization of probe features sizes has been made possible by advances in complementary metal-oxide-semiconductor (CMOS) and microelectromechanical systems (MEMS) technologies. Successive developments in CMOS fabrication to produce integrated circuit (IC) chips have enabled the miniaturization of

features from 10 μm to 14 nm (Lojek, 2007). Additionally, advances in the MEMS industry have enabled fabrication of nanoscale devices with small, high-aspect ratio mechanical features (Crone, 2008). Bulk micromachining is used to define and etch the silicon (Lin, 2008) while surface micromachining is used to deposit material and form layers onto the silicon substrate (Bustillo et al., 1998). The use of CMOS technologies enables us to utilize the scalability and technological maturity of semiconductor fabrication industry for mass production and dissemination.

The developments in silicon-on-insulator technologies have enabled fabrication of dense 3D electrode arrays at Caltech with as many as 1,024 available recording sites (Rios et al., 2016). These passive probes enable thermal isolation of backend active electronics and prevent heat dissipation into neural tissue. Additional developments with integrated silicon CMOS technologies have also enabled the development of other neural probes such as the Neuropixel probe from the team lead by Professor Timothy D. Harris at Janelia Farms Research Campus in collaboration with IMEC fabrication foundry with total of 1,280 electrodes sites per shank, with 384 recording channels available at a time (Steinmetz et al., 2021). Together these developments with multisite electrodes enable greater volumetric coverage of electrical activity in the brain.

1.2.2 Integrated microfluidic platforms for isolating and imaging synapses glutamate release with contact imagers

While multisite silicon neural probes allow for detection of electrical activity, they lack the ability to detect chemical activity. Since neuron signals consists of an electrical and chemical component, monitoring chemical release of neurons, in particular the synaptic neurotransmitter release is vital in understanding neuron communication. The second part of this work focuses on using microfluidic devices to visualize and quantify synaptic glutamate release in neuron cultures.

We chose to monitor glutamate release because glutamate is the primary excitatory neurotransmitter in the brain and is implicated in a number of acute and chronic neurodegenerative diseases such as Huntington's, Parkinson's, and Alzheimer's disease (Meldrum, 2000). Glutamate pathways are linked to many other neurotransmitter pathways and glutamate receptors are pervasive in multiple regions of the brain (*Glutamate-Related Biomarkers in Drug Development for Disorders of the Nervous System*, 2011). Additionally, glutamate plays an important role in synaptic plasticity and is involved in learning and memory in the brain (McEntee & Crook, 1993).

Multiple methods to detect glutamate in the brain exist such as microdialysis combined with high performance liquid chromatography and tandem mass spectrometry (Buck et al., 2009), genetically encoded fluorescent reporters (Marvin et al., 2013), and silicon probes with biosensor microarrays for amperometric detection (Moldovan et al., 2021). However, with microdialysis and fast-scan cyclic voltammetry (FSCV), it is difficult to sample only synaptic release due to the large size of the microdialysis probe, which is approximately 200-500 μm in diameter (Jaquins-Gerstl & Michael, 2020), and the thickness

of the FSCV silicon probe, which is approximately 200 μm thick (Moldovan et al., 2021); both of which are larger than the synaptic bouton which ranges from 2-5 μm (Knodel et al., 2014). In contrast, genetically encoded reporters enable targeting of fluorescent reporters to the individual synapses via the use of promoters localized to synaptic vesicles such as synaptophysin (Dreosti et al., 2009).

Microfluidic devices provide a useful neuron based culture platform to orient the otherwise stochastic orientations of axons and dendrites (Taylor et al., 2005, 2010a). Additionally, multi-compartment microfluidic devices enable fluid isolation of distinct segments of neuron cell bodies, dendrites, axons, and synapses (Taylor et al., 2003, 2005, 2010a). This enables manipulation of each of these neuronal segments and visualization using high resolution imaging or contact imagers.

1.3 Thesis Overview

This thesis describes the development of novel electrophysiology neural probes with highly dense electrode arrays. We describe their design, fabrication, assembly of the ephys neural probe system, characterization of electronic noise and properties, integration with two-photon imaging, and analysis of the neural probe's detection limits. The yield and quality of electrophysiological recordings *in vivo* are demonstrated in experiments with anesthetized head-fixed mice. The invasiveness of the probe shank is demonstrated by quantifying vasculature and neuron damage *in vivo* during insertion.

Chapter 2 describes the rational design our novel neural probes. The design considerations we assessed were: 1) neural probe shank buckling caused during insertion into the brain tissue, 2) damage of surrounding brain tissue caused during probe insertion, and 3) biocompatibility of probe material with neural tissue.

Chapter 3 describes fabrication steps for the neural probe produced at the CMOS and MEMs foundry, Laboratoire d' Electronique des Technologies de l'Information (CEA-Leti). Fabrication was guided by design considerations described in the previous section.

Chapter 4 describes the assembly, packaging, and electronic characterization of 32-channel and 256-channel neural probe assemblies. This assembly consisted of the neural probe and custom passive PCB, which interfaced to a commercially available data acquisition (DAQ) headstage system. 256-channel assemblies also included a custom high-density flexible cable and interposer to interface with the neural probe and enable higher channel connections. 32-channel assemblies were designed for acute recordings while 256-channel assemblies were designed for chronic recordings. Assembly profiles were designed to be compatible with two-photon imaging setups described in latter chapters. Electronic characterization of the probe assemblies was carried out with benchtop testing in saline. Electroplating methods were used to reduce electronic impedance and noise. Finally, the probe's profile, electrode density and size, channel count, impedance, and electronic noise were compared with other state-of-the-art ephys neural probe systems.

Chapter 5 describes acute, *in vivo* recording setups in head-fixed mice for probe testing. Animal and surgical procedures are described for head-fixation, craniotomies, and imaging window preparations. Three platforms for neural probe insertion and ephys recording were deployed: 1) stereotaxic frame with adjustable anesthesia, 2) widefield imaging, and 3) two-photon imaging setups. Electrophysiology setups for *in vivo* recording paired with two-photon imaging of inserted probe and surrounding tissue are described. Lastly, data analysis workflows to analyze spiking activity are described.

Chapter 6 presents mapping of neurons with juxtapositional ephys recording to two-photon imaging of multisite silicon neural probes and surrounding tissue *in vivo*. We establish concurrent two-photon imaging, high-quality *in vivo* neural recordings, and our analysis to benchmark the detection limits of the probe and isolate single unit activity. Using this information, we can deterministically map the position of each neuron relative to the probe based on extracellular spiking activity detected on ephys probes. Using spike sorting to isolate spike waveforms, we examined the ability of our dense electrode arrays to spatially sample the location of neurons and demonstrate our ability to map single neuron units with concurrent two-photon imaging *in vivo*.

Chapter 7 presents quantification of probe invasiveness using vasculature and neuron staining *in vivo*. In this chapter, we look at the invasiveness of the probe with mice and describe for the first-time imaging of probe as it is inserted using vasculature stain *in vivo* under two-photon imaging. To quantify the probe invasiveness, we examined the displacement of neurons and vasculature during and after probe insertion and removal. A model of the 3D vasculature was created to quantify the displacement during probe insertion and after probe removal.

Chapter 8 describes the use of channelrhodopsin mouse lines to modulate neural activity in neurons neighboring the neural probe. We establish channelrhodopsin mice models with sparse labeling in the cortex. We also present two photon imaging of cortical interneurons labeled with channelrhodopsin and ephys recording with widefield blue light induced silencing. We establish recording of high quality ephys data and effective silencing of spiking activity with blue LED lights. In future studies, by combining paired ephys recording with two-photon imaging of the probe and surrounding brain tissue, we can

establish the position of each neuron and deterministically modulate the amplitude and spike frequency of the neuron, thus benchmarking the detection limits of silicon based ephys probes. The main purpose of this setup for future studies is to establish a pipeline for close-loop control of surrounding neural activity and study the effect of single neuron stimulation on local cortical circuits.

Chapter 9 describes development of a microfluidics platform for measuring synaptic glutamate release and response to neuromodulating drugs. We establish a microfluidic platform enabling isolated infection of a two-part sensor (consisting of a pre-synaptic and post-synaptic part) to detect synaptic glutamate release. We also demonstrate compartmentalization of synaptic processes to allow for easier isolation and visualization of synapses during imaging. We describe a rationally design microfluidic device whose channel lengths are based on axon and dendrite growth rates reported in literature to enable better reconstitution of synaptic processes and use computational fluid dynamic simulations with ANSYS Fluent software to model perfusion flow in the device. Our newly proposed device is designed for integration with CMOS contact sensors to enable monitoring of multiple synaptic release events at one-time point.

Lastly, Chapter 10 compares where the project stands in comparison with established efforts in literature and presents our future directions. The ultimate goals of the projects described in this thesis are to: better understand the recording capabilities of extracellular ephys probes to recapitulate the entirety of brain spiking, provide a platform for deterministically modulating neuronal circuits for close-loop feedback systems, and understand the coordinated neural activity and the kinetics of neuronal signaling.

Chapter 2

THEORY AND ASSEMBLY PACKAGING CONSIDERATIONS

2.1 Introduction

One drawback of using extracellular recording electrodes is their invasiveness. To minimize this damage while maintaining high quality recordings, we focused on increasing the number of recording sites per shank and adjusting the shank dimensions to minimize tissue displacement. Additionally, the biocompatibility of probe materials was considered to reduce inflammation during chronic recording. To reduce heating, we decoupled active electronics on the ASICs from electrodes using a flexible cable or passive PCBs connecting the probe to downstream active electronic components.

2.2 Probe and assembly design considerations

The design of assembly components was guided by the need to: 1) minimize damage in the brain tissue during insertion of the neural probe, 2) maintain mechanical stability during insertion, 3) maintain biocompatibility in the mouse brain during chronic recording, and 4) maximize the quality of recorded extracellular signals.

2.3 Mechanical design of the probe

2.3.1 Probe geometry

The upper bound of the neural probe shank dimensions was constrained to limit damage during implantation, while the lower bound was constrained by the mechanical stability of the shank and by the need to limit electrical noise and crosstalk between electrodes and wiring routes. While we want to minimize the probe dimensions to limit damage in the brain during insertion, we also want to ensure the shank cross-section area is

large enough to withstand the stress generated during insertion. To ensure mechanical integrity, the buckling threshold must compensate for the stress generated during insertion and ensure the neural probe shank does not deform significantly past its original straight position.

2.3.2 Shank deformation under insertion

For the probe to withstand forces generated during insertion, the insertion force (F_{in}) should not exceed the buckling load. Bucking helps compensate for the stress generated during insertion and prevents the probe from fracturing. To estimate the bucking of the shank during insertion into the dura and brain, we will simplify the calculation by assuming the probe is composed entirely of silicon. We will assume the column is fixed at the end near the base and can pivot on the tip. Using Euler's formula, we can estimate the buckling force threshold or the critical load P_{cr}, where E is the modulus of elasticity, I is the moment of inertia, and L is the length of the column:

$$P_{cr} = \frac{2EI\pi^2}{L^2}.$$

The moment of inertia using a rectangular cross-sectional area, where h is the thickness, can be calculated by:

$$I = \frac{wh^3}{12}.$$

Putting these measurements together, we see that for a neural probe with L= 6 mm long shank, thickness h=20 μm, and width = 160 μm (near the shank tip) has a moment of inertia,

$$I = \frac{160\ \mu m\ \times\ 20\ \mu m^3}{12} = 4 \times 10^{-18} m^4.$$

If we estimate the modulus elasticity (E) for silicon = 130-188 GPa and take the upper threshold of the modulus of elasticity value for silicon, then the probe has a buckling force threshold of around 41 mN (Hopcroft et al., 2010).

$$P_{cr} = \frac{2 \times 188GPa \times 4 \times 10^{-18} m^4 \pi^2}{(6 \times 10^{-3})^2\, m^2} = 41\ mN.$$

Experimental measurements of forces generated for a single shank probe inserted into the cortex after dura mater removal ranges from 1 to 10 mN depending on the geometry of the probe tip, insertion speed, region of the brain (e.g. cortex vs olfactory bulb), and probe surface treatment coating (W. Jensen et al., 2006; Sharp et al., 2009). Thus, buckling load of 41 mN exceeds the insertion forces of 1 to 10 mN so the probe will be able to withstand implantation.

Lateral displacement of the probe during implantation can be calculated as:

$$\sigma_{max} = \frac{6Ehu}{L^2}.$$

When the maximal lateral displacement (u) displacement exceeds the fracture stress of silicon (σ_{max} =1.7x10^7 N/m^2), the shank will break (Rios et al., 2016). Thus, if we set the σ_{max} to 1.7x10^7 N/m^2 and calculate the maximal lateral displacement for our 6 mm long shank with 20 μm thickness and modulus of elasticity = 170 GPa (for silicon), we find that u =2.86 mm. Therefore, when the shank is displaced by 2.86 mm laterally the probe will fracture.

$$u = \frac{\sigma_{max} L^2}{6Eh} = \frac{1.7 \times 10^7 \frac{N}{m^2} \times (6 \times 10^{-3} m)^2}{6 \times 170\ GPa\ \times\ 20 \times 10^{-6} m} = 2.86\ mm.$$

2.4 Electrical design of the probe

2.4.1 Probe wiring and interconnect parasitics

Key parameters of the probe design included a dense array of electrodes to allow for high resolution recording and a narrow shank profile to minimize mechanical perturbation in the brain tissue during probe insertion while maintaining low signal noise during electrode recordings. To allow for signal isolation, electrodes, interconnects, and interconnect lines needed to be spaced sufficiently apart. Sources of signal noise include thermal noise due to line resistance, crosstalk capacitance coupling, and interconnect electrical parasitic effects. Thermal noise can be calculated as using the Johnson-Nyquist noise equation:

$$v_n = \sqrt{4k_B RT\Delta f}$$

where v_n is the root mean square voltage, k_B is the Boltzmann constant, R is the resistance, T is the temperature, and Δf is the bandwidth. Thus, for a gold-plated electrode with an impedance of approximately 300 kΩ at room temperature and bandwidth of 6.4 kHz the thermal noise is approximately 5.6 μV_{RMS} and is below amplitude of action potential signals.

$$v_n = \sqrt{4 \times 1.38 \times 10^{-23}\ \frac{J}{K} \times 300000\Omega \times 300\ K \times 6400\ Hz} = 5.6\ \mu V_{RMS}.$$

To record biologically relevant action potentials of 25 μV amplitude or above, the minimum noise level for each recording size should be below 20 μV so this limits the electrode size to 16 μm^2 or larger (Najafi et al., 1990). To pack all 256 electrodes and maintain a narrow shank, we used nanoscale interconnects. However, closely spaced interconnects also increases coupling capacitance and crosstalk between neighboring lines (Du et al., 2011). To account for shunting capacitance between parallel interconnects, we

modeled two parallel interconnects of width (*w*), thickness (*t*), and length (*L*) spaced a distance (*d*) with a dielectric layer with thickness t_{btm} separating the interconnect lines from the silicon substrate ground. We used the infinite parallel line approximation to approximate the capacitance coupling, $C_{coupling}$, between two parallel interconnects:

$$C_{coupling} \approx \varepsilon_r \frac{hL}{d}$$

where the permittivity of the dielectric material is ε_r.

The shunting capacitance to the ground can be approximated by:

$$C_{shunt} \approx \varepsilon_r \frac{Lw}{t_{btm}}.$$

Putting this together, the potential crosstalk $V_{crosstalk}$ can be calculated as:

$$V_{crosstalk} = \frac{C_{coupling}}{C_{coupling} + C_{shunt}} V.$$

Resistance in the interconnects can be calculated by:

$$R = \frac{L}{A}\rho$$

where *A* is the cross-sectional area (*A*=*wh*), ρ is the resistivity of the material, and *L* is the interconnect length. To minimize interconnect parasitic, nanoscale interconnects with a cross section of 300 nm x 300 nm, spaced 300 nm apart were used (Rios et al., 2016).

2.4.2 Maximizing signals

To better correlate extracellular signals to the circuitry of simulated neurons, we used a current source density (CSD) estimate. The pitch and density of electrodes were designed to maximize the CSD. Silicon-based neural probes consisted of 256 electrodes arranged as four columns near the tip (Figure 2.1).

The current source density for a volume of tissue located at x, y, z coordinates can be modeled by:

$$I_m(x,y,z) = -\left[\sigma_x \frac{\partial^2 \phi}{\partial x^2} + \sigma_y \frac{\partial^2 \phi}{\partial y^2} + \sigma_z \frac{\partial^2 \phi}{\partial z^2}\right]$$

where ϕ is the field potential and σ_x, σ_y, and σ_z the principal conductivities relative to the axes of the tissue (Freeman & Nicholson, 1975). Increasing the density of electrodes relative to the position of neurons in the tissue helps to improve the current source density estimate (Freeman & Nicholson, 1975).

Experimentally, extracellular spikes for hippocampal CA1 pyramidal cells have been recorded as far as 140 μm from the electrode to the cell body (Henze et al., 2000; Holmgren et al., 2003). Thus, if we estimate the recordable volume around an electrode as a cylinder, we can potentially record around ~1,000 neurons in this volume of rat cortex (Buzsáki, 2004). However, in practice the limitations of resolving single neuron activity through spike sorting will greatly reduce the number of recordable neurons (Buzsáki, 2004).

2.5 Biological and biocompatibility design considerations

For the probe to be viably implanted and record relevant physiological data, we need to ensure that the probe 1) causes minimal damage during implantation, 2) can record deep brain regions of interest, 3) is biocompatible and does not lead to toxic side-effects during implantation, and 4) can be sterilized.

2.5.1. Neural probe considerations

2.5.1.1 Parylene for biocompatibility, biostability, and sterilization

One challenge to obtaining high quality neural recordings of neural probe is maintaining the chronic viability of neural probes implanted in the brain. To be biocompatible, the probe must 1) not be toxic or lead to toxic by-products, 2) avoid causing an immune and inflammation response, and 3) not lead to necrosis of surrounding tissues. To address these concerns, a layer of parylene was deposited as an outer coating over the shank. Parylene was chosen due to its biocompatibility and biostability.

Some advantages parylene provides are its excellent electrical and thermal insulation, hydrophobic coating for waterproofing, oxidation protection, reduction to friction during implantation, little cytotoxicity, and stability in biological tissues (Loeb et al., 1977). The parylene covered shank can be sterilized prior to implantation with methods such as gamma radiation, steam autoclaving, ethylene oxide, e-beam radiation, and hydrogen peroxide or ethylene oxide plasma. Parylene has been also been approved for use in medical device coatings and is United States Pharmacopeia (USP) Class VI and ISO 10993 certified (Golda-Cepa et al., 2020).

2.5.1.2 Minimizing damage

To minimize tissue displacement and damage during implantation, probe geometry was considered to minimize the surface area and volume of the shank. The tip of the probe's shank was thinned to 20 μm to minimize displacement of the tissue and in principle to allow for more accurate coverage of the surrounding neural population. Additionally, the probe shape designed with a sharp point tip and flat cutting edge parallel to insertion and the probe base (resembling a No. 11 scalpel) allowed for more precise cutting through the tissue.

2.5.1.3 Rodent neural probe: Experimental constraints for brain insertion

Shanks were 6 mm long to readily permit penetration into deep regions of the brain in rodents. The interelectrode pitch was also designed to match or be less than spacing between neurons of interest, in our case the interneurons in the cortex (Sher et al., 2007). Neuron density is highest in cerebellum at 2.6 x 10^6 neurons per mm^3 and in the neocortex it 9.2 x 10^4 neurons/mm^3 on average, while in the cortex there are approximately 100,000 neurons/mm^3 (Schüz & Palm, 1989). Thus, the probe's interelectrode pitch of 20 µm horizontally and 16 µm vertically enabled capture of surrounding neurons in the densest brain regions. At the base of the probe, gold pads were 95 µm in diameter and with a pitch of 200 µm for flip chip connection during assembly.

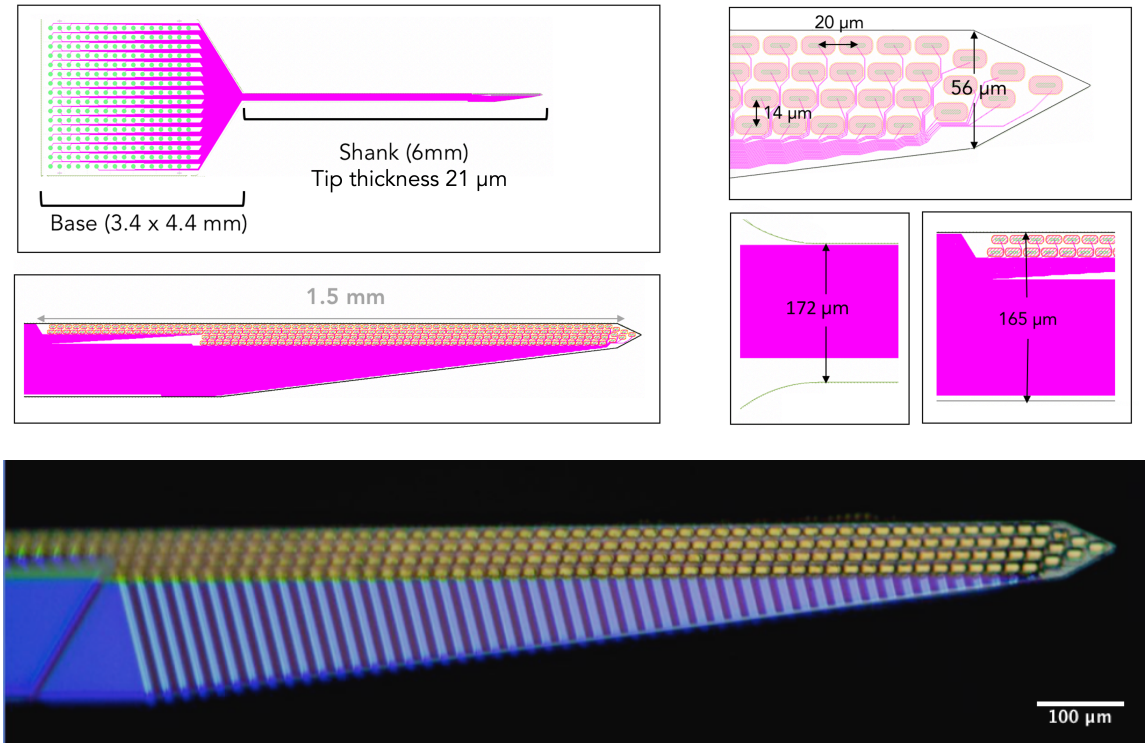

Figure 2.1 Picture of rodent neural probe and dimensions. Shank tip was thinned to a thickness of 20 µm. Pads were spaced apart 20 µm horizontally and 14 µm vertically. Rodent probes were designed by Dr. Warren Fon.

2.5.1.4 Non-human primate (NHP) neural probe

We also designed a probe with a longer 38 mm shank designed for insertion into the brain of non-human primates (NHP) (Figure 2.2). Other than the length of the shank, the composition, layers, and pad dimensions of the NHP probe were similar to the rodent probe. Like in the rodent probe, gold metal electrodes are passivated around the edge by parylene and electrode pads on the shank are 6 x 14 µm. The pitch between electrodes is 20 µm horizontally and 16 µm vertically. The first electrode is 230 µm from the probe tip.

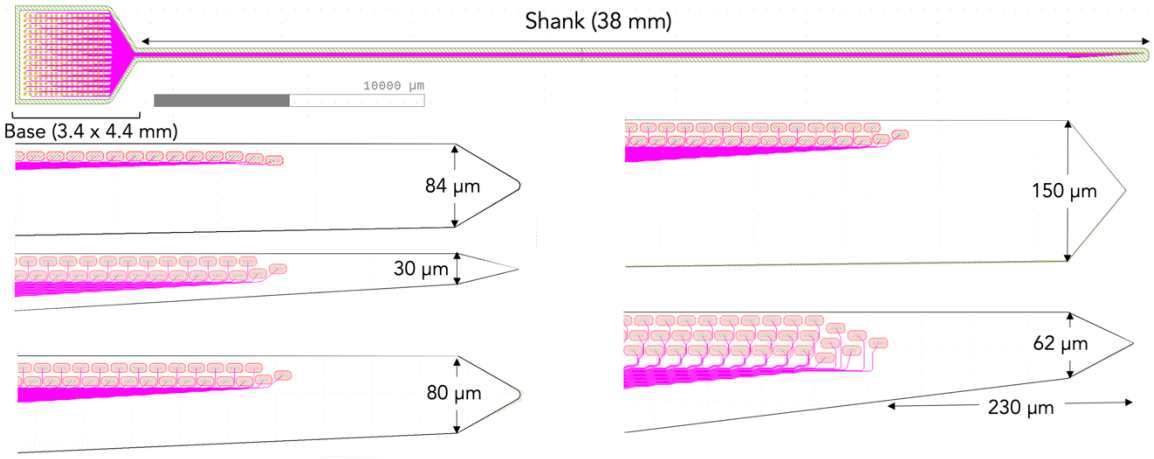

Figure 2.2: Non-human primate probe dimensions. The probe tips of various probe designs are shown.

2.5.2 Passive printed circuit board (PCB) connecting board bonded to rodent neural probe

PCBs were designed using Autodesk EAGLE and 3D models were generated using Fusion 360. PCBs were fabricated at PCBway. Assemblies consisted of either a 32-channel assembly or 256-channel assembly. Both used the same Caltech/LETI neural probe and were connected to either 32-channel or 256-channel PCB.

2.5.2.1: 32-channel acute assemblies

To minimize obstruction of PCB during two-photon image, we designed a custom PCB where the top of the PCB that the probe mounts to is narrowed to 4 mm. The bottom of the PCB mounts to a 32-channel connector (Omnetics A79024-001) that connects to a commercial stimulation and recording headstage (Intan RHS 32-channel) via a mating connector (Omnetics A79025-001). To connect the probe to PCB, probe pads were connected with aluminum wire bonding (Westbond Wedge Bonder). A layer of epoxy was applied atop wire bonds for mechanical stability of wire bond connections and waterproofing during *in vivo* insertion.

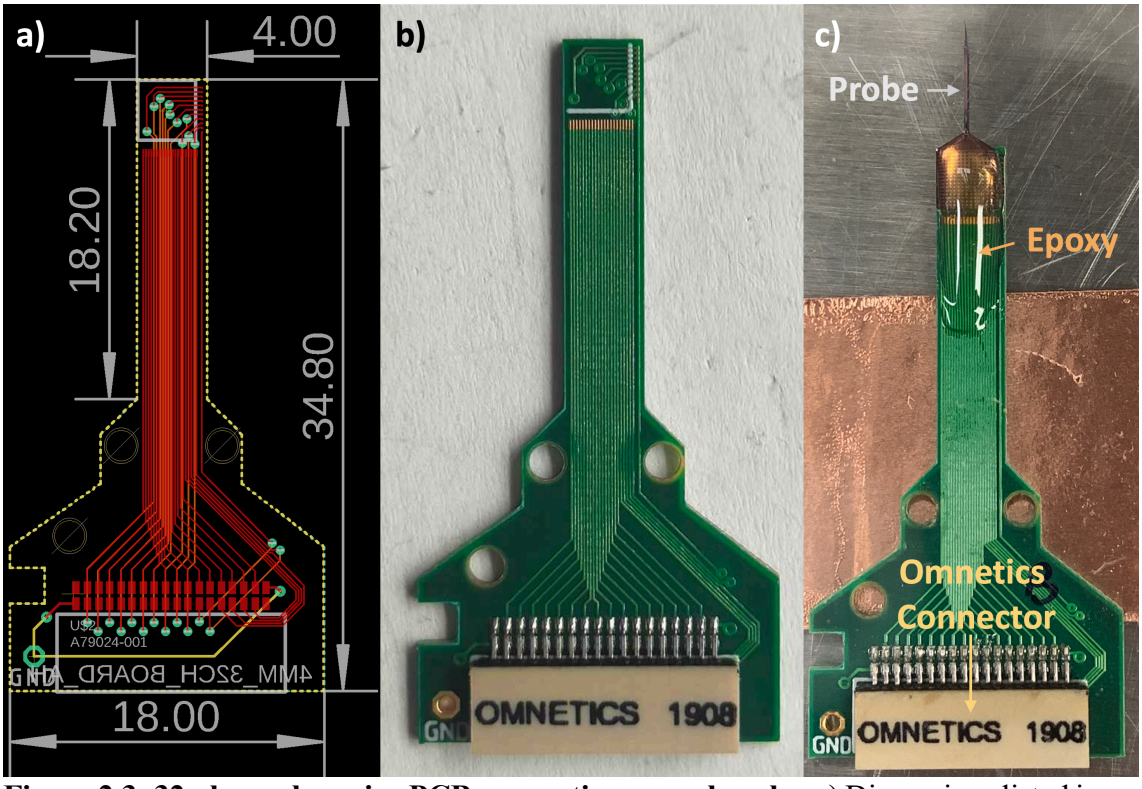

Figure 2.3: 32-channel passive PCB connecting neural probe. a) Dimensions listed in mm of 32-channel acute PCB. b) Acute 32-channel PCB board. c) Acute board with rodent neural probe mounted to PCB. Neural probe is electrically connected to PCB via wire bonds and encapsulated with epoxy (clear brown).

2.5.2.2 256-channel assemblies

To allow for chronic recording in mice with full connections to all the neural probe electrode sites, we created 256-channel assemblies. The assembly consisted of the neural probe, polyimide flexicable, and passive PCB that connected to backend recording headstages.

2.5.3. Flexicable considerations: Polyimide flexicable for chronic recordings and decoupling head motion

An ultra-flexicable (Hightec MC AG) connecting the probe to the PCB was used to decouple mechanical movement of the probe head from the rest of the assembly. This modular architecture also helps to decouple the neural probe from the digitizing back end and allows iterations of multiple probe and PCB designs to the same flexicable assembly.

The flexicable was made of polyimide, which provides a reliable electrical insulation and passivation layer with excellent dielectric properties that is biocompatible, chemically resistant, lightweight, and mechanically flexible (Stieglitz et al., 2000). Additionally, polyimide has been used as interface cables in other state-of-the-art commercially available electrophysiology systems, such as those deployed by Neuropixels (Steinmetz et al., 2021). Ball bumps were deposited on either ends of the flexicable for bump bonding to the probe and interposer on either end of the flexicable (Figure 2.4).

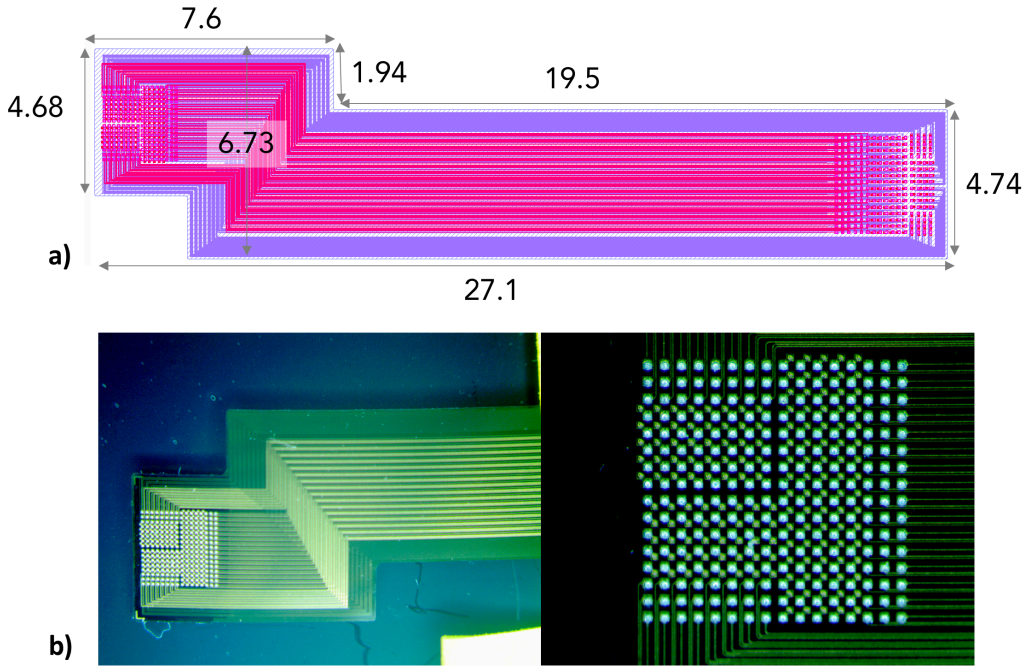

Figure 2.4: Polyimide flexicable. a) Dimension of flexicable in mm. b) Ball bumps on either end of flexicable. Image credits: Warren Fon.

2.5.4 Headstage and DAC considerations

Commercially available Intan headstage (RHS 32-channel or RHD 128-channel recording headstage) were used to allow for easier dissemination, greater interoperability with other systems, and reduced costs required to replace headstages for each probe. Headstages consisted of integrated electronic circuit chip (Intan RHS21116 for 32-channel stimulation and recording headstage or RHD2164 for 128-channel recording headstage) that multiplexed, amplified, and digitized signals (Harrison & Charles, 2003). The digitized signal is then simultaneously and continuously sampled at 30 kS/s using a controller box (Intan 128ch Stimulation/Recording Controller or 512ch Recording Controller).

2.6 Conclusion

In conclusion, we demonstrate a rationally designed dense, 21 μm thick, neural probe that is thin enough to minimize displacement and damage and thick enough to withstand buckling forces during implantation. Interconnects were spaced closely to allow for dense arrangement of electrodes, minimize tip width, and allow enough space between neighboring signal lines to minimize excessive crosstalk. Acute, 32-channel connecting PCB boards were designed to minimize obstruction on the probe end during two-photon imaging. Meanwhile, flexicable were designed for 256-channel chronic assemblies to delocalize the bulkiness and weight of downstream PCBs. Lastly, these connecting boards were designed to mount to commercially available recording systems for easier interoperability with existing ephys systems.

Chapter 3

NEURAL PROBE FABRICATION

3.1 Introduction

Electrophysiology measurements are vital in understanding neural circuitry behavior. Early extracellular recordings relied on large tetrodes that consisted of quadruple microwires twisted together, with the insulation on the wire end removed to form electrodes, that were then inserted into a cannula for implantation (Gray et al., 1995). While such technologies provide high-quality multiunit recording, the tetrode's large size and small recording area limits the ability of tetrodes to capture a large volume of neural activity. Recent developments of silicon based neural probes have enabled the miniaturization of neural probes with higher electrode counts. Scaling up the number of recording sites introduces several design constraints and difficulties during fabrication that we addressed by utilizing advances in CMOS and MEMS technologies.

To maximize the density and number of electrodes across the probe shank, CMOS and MEMS fabrication were used to fabricate nanoscale features on neural probes. The neural probe consists of six layers: a silicon substrate, bottom insulator, metal interconnect, top insulator, metal electrodes/pad, and parylene biocompatible layer. A silicon layer was used as a substrate layer atop which insulator, interconnect, and biocompatibility layers were deposited. Fabrication used a silicon on insulator (SOI wafer) consisting of a silicon device layer, buried silicon oxide (BOx) layer for insulation, and silicon support handle layer. Atop the wafer, a layer of thermal silicon oxide was deposited for insulation. A metal nanoscale interconnect layer was patterned using electron beam lithography and used to connect stacks.

Surface micro-machining was used to deposit the top insulator and a parylene biocompatibility layer, which surrounded the electrode openings. These two layers were used to insulate the metal interconnects and reduce undesirable cross-reactivity during brain implantation. Shanks were shaped with silicon etching techniques. Lastly, metal bumps were deposited on the surface to electrically connect the probe base to the rest of the assembly during flip-chip bonding. This chapter will detail the fabrication protocols used to produce the 256-channel electrophysiology neural probes at CEA-LETI, a MEMS and CMOS foundry.

3.2 Neural probe fabrication steps

The neural probe was fabricated at LETI's CMOS and MEMS foundries as outlined in (Rios et al., 2016). Probes were fabricated on silicon wafers (200 mm in diameter and silicon on insulator (SOI)). CMOS facilities were used to make nanoscale interconnects and MEMS facilities were used for the rest of the steps. The eleven key layers and steps are: 1) SOI wafer substrate consisting of Silicon/Buried Oxide (Si/BOx), 2) deposition of the bottom insulator made of SiO_2, 3) etching and patterning of copper metal interconnects, 4) deposition of top insulating layer, 5) etching of vias and copper fill, 6) electroplating gold electrodes and pads, 7) topside etching, 8) biocompatible layer made of parylene HT deposition and etch, 9) backside oxide etch, 10) handle layer etch, and 11) device release. The processes below are numbered accordingly by their layers and steps (Figure 3.1).

3.2.1 Substrate SOI wafer (1)

Fabrication used 200 mm SOI wafers consisting of: a handle layer 700 μm thick, a BOx layer 1 μm thick, and a device layer 15 μm thick. The wafer was cleaned with acetone and isopropyl alcohol (IPA) to remove oils and organic contamination prior to fabrication.

3.2.2 Bottom insulator layer (2)

Next, a layer of silicon oxide is thermally grown to a thickness of 1.2 μm. The BOx layer provides stress compensation allowing the shanks to remain straight and an etch-stop when the handle layer is etched on the wafer backside. This insulator also provides a bottom insulator layer for the metal interconnects.

3.2.3 Metal interconnect (3)

A dielectric layer comprised of silicon dioxide and silicon nitride (SiO/SiN) was deposited on the wafer and the interconnect lines (300 nm wide) were patterned with a 248 nm deep ultraviolet (DUV) stepper lithography (ASML300). This method was used because it can finish patterning of the 200 mm wafer within minutes and is significantly faster than conventional electron beam lithography, which would take days. Next, a copper layer was deposited using a dual-damascence process. This process consists of 6 steps outlined as follows:

1. Etch dielectric stack using the DUV-patterned, metal-layer photoresist as an etch mask.
2. A thin layer of tin was deposited (TiN, 20 nm) as a barrier layer to prevent copper diffusion.

3. A thin copper (200 nm) layer was deposited to seed subsequent electroplating layers.
4. A thicker layer of copper (300 nm) was deposited so it overfills the trenches using electrochemical deposition (ECD).
5. Wafer was adhesion baked at 400°C for 30 minutes.
6. Excess copper was removed using chemical mechanical polishing so that only copper lines the trenches forming the interconnects

3.2.4 Top insulator (4-5)

Plasma-enhanced chemical vapor deposition (PECVD) was used to create a SiN / SiO (40 nm 500 nm) dielectric layer to insulate metal interconnects. Next, vias were created through reactive-ion etching (RIE) through the top insulator layer to provide a connection between recording electrodes and interface pads. Another damascence process was used to line interconnects with copper.

3.2.5 Electrode and interface pads (6)

Gold is used for recording electrodes due to its low reactivity and biocompatibility. To form gold electrodes and pads, a layer of nickel (700 nm) is deposited as a seed layer atop which the gold layer (300 nm) was electroplated. Since copper is not biocompatible, cytotoxic, and can lead to oxidative stress in the brain, it is vital that the copper is covered with gold and prevented from coming into contact with the brain (Cortizo & De Mele, 2004; Scheiber et al., 2014).

3.2.6 Top side device definition (7)

The neural probe profile was then etched through dielectric layers and BOx using reactive-ion etching (RIE) while the silicon device layer was etched using deep reactive-ion etching (DRIE).

3.2.7 Biocompatibility coating (8)

A layer of parylene HT was deposited using chemical vapor deposition (Specialty Coating Systems). Paraylene HT was chosen rather than parylene C due to its higher temperature stability (up to 450 °C for short term exposure). This parylene layer also provides a biocompatible, chemically resistant, electrical insulating layer during implantation. Additionally, parylene has a low coefficient of friction, allowing it to minimize friction and damage during probe implantation in the brain. Parylene also conforms well to the features of the probe, helping to electrically insulate exposed areas on the top and sides of the shank. After deposition, a layer of photoresist is used to protect the parylene during step coverage and patterning of recording sites. Lastly, parylene is etched using RIE to expose recording and pad sites.

3.2.8 Back side device definition (9-11)

The thermal oxide layer on the backside was patterned and etched using RIE as shown in step 9 in Figure 3.1. Next the silicon device layer was etched using DRIE to the BOx layer (100 nm) that serves as an etch stop and provides a smooth backside surface for packaging (10). Lastly, the BOx layer was etched using RIE to release the probes (11). Anchors in the layer are used to keep the probes in place before manual extraction.

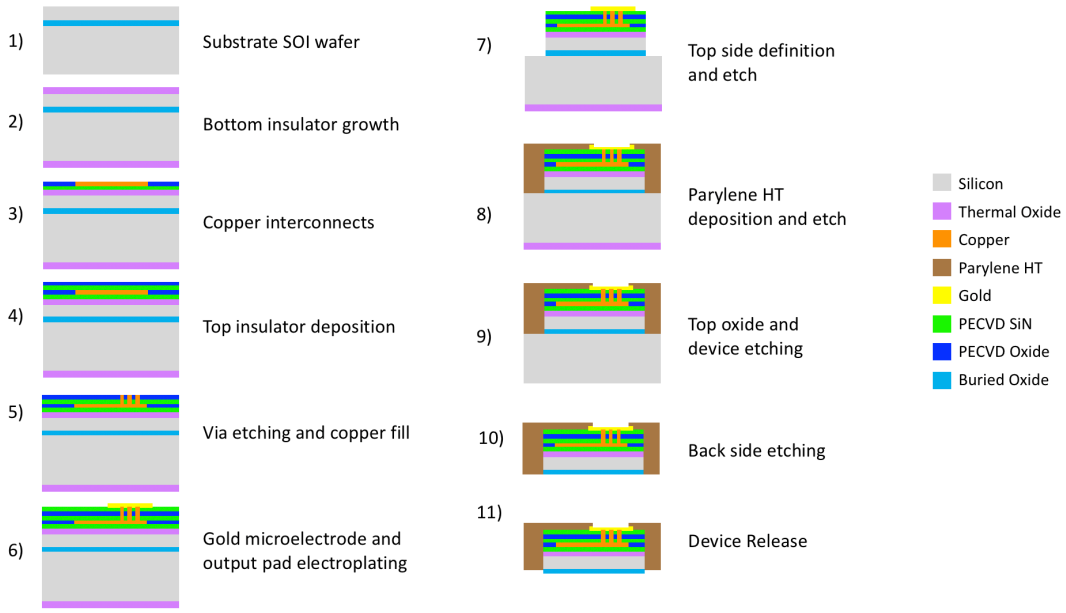

Figure 3.1 Neural Probe Fabrication Steps. Figure modified from (Rios et al., 2016).

3.3 Conclusion

In conclusion we describe the fabrication methodologies for building neural probes at the commercial CMOS and MEMS foundry at CEA-LETI. These fabrication methodologies were developed to build neural probes following design rules described in Chapter 2. The thicknesses, nanoscale features, and materials during fabrication were chosen to offer adequate stress compensation during insertion, minimize tissue damage, and provide biocompatibility with neural tissue. Additionally, the use of commercial foundries at CEA-LETI helps with mass-production and dissemination of the neural probes.

Chapter 4

ASSEMBLY, PACKAGING, AND ELECTRICAL CHARACTERIZATION

4.1 Introduction

To record relevant signals from the electrodes, the neural probes need to interface with backend electronics for signal conditioning and data acquisition systems. Some key constraints these assemblies must meet are: the cable or board connecting to the neural probe must not be too bulky else it will obstruct the objective lens during imaging, parts of the assembly in contact with the brain or skull must be made out of biocompatible materials, electronics must have low noise (to enable detection of low amplitude signals), assembly must be able to mount to a micromanipulator robot to control the position and speed of the neural probe during insertion, and electrical connections facing the insertion site must be water-proofed to enable *in vivo* experiments. This chapter describes the development of two assemblies that address these concerns: a 32-channel assembly for acute recording and a 256-channel assembly for chronic recording.

4.2 32-Channel Assemblies

The 32-channel assembly for acute recording consists of a custom 32-channel passive PCB designed to connect neural probe to active electronic components. PCB pads were coated with Electroless Nickel Electroless Palladium Immersion Gold (ENEPIG) surface finish to allow for downstream wire bonding interconnections. The backside of neural probes was attached to the custom-designed 32-channel passive PCB with a drop of heat-curable epoxy (Epoxy Technology, EPO-TEK 730). The neural probe was then electrically

connected to the pads of the custom PCB (electroless nickel immersion gold (ENIG) surface finish) via wire bond contacts made of alloyed aluminum bond wires (West-Bond Wedge Bonder). In this wire bonding process, an ultrasonic pulse was applied to either ends of the bond wire by the wedge as it met the pads on the neural probe and PCB. Due to the fine pitch of base electrode pads and large footprint of the wedge bonder, it is difficult to fit many wire bond contacts to connect to all sites in the probe base to the PCB. This limited the number of connections to 32-channels.

Next, a thermally and electrically insulating epoxy (Epoxy Technology OG116-31/3CC) with a low coefficient of thermal expansion was chosen so there would be minimal displacement of wire bonds during encapsulation and UV curing. The epoxy also protected and waterproofed the electrical connections during *in vivo* recording. The back of the connecting PCB has an Omnetics A79024-001 connector that plugs to a mating connector (Omnetics A79025-001) on the commercially available stimulation and recording headstage (Intan RHS 32-channel). To house and shield the assembly during *in vivo* recording, a custom holder was designed. This holder was mounted to the micromanipulator, which enables control of probe speed and position during insertion (Figure. 4.1).

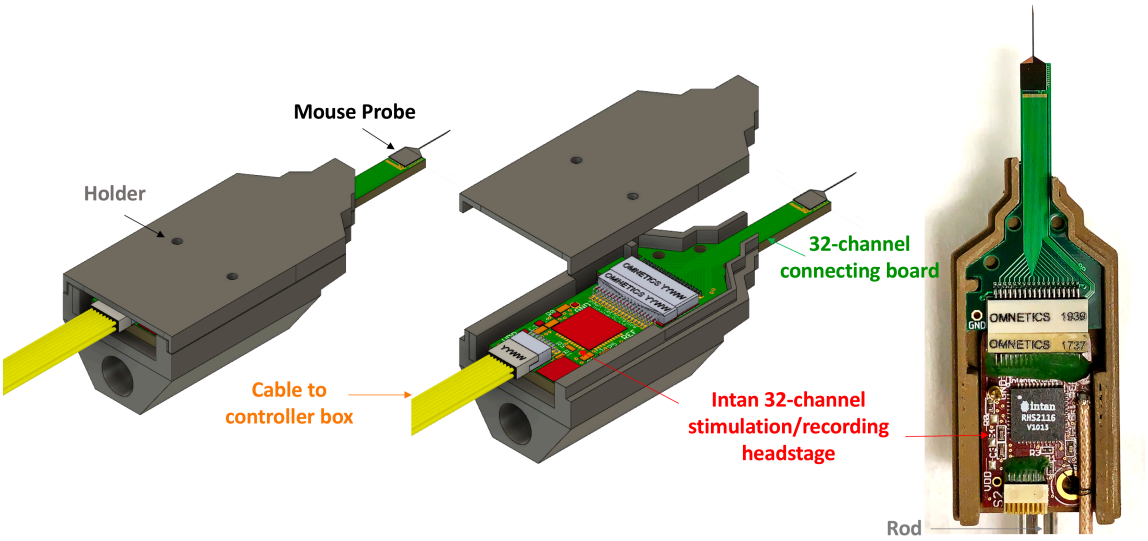

Figure 4.1: 32-channel rodent assembly with holder mounting to micromanipulator The holder is designed to insert into a rod (through the hole at its base). This rod was then mounted to the micromanipulator. *Left:* Actual assembly with rod that mounts to micromanipulator on the bottom.

4.3 256-Channel Assemblies

The assembly consisted of the neural probe (for either rodent or non-human primate designs), ultra-flexicable, and PCB (Figure 4.2). The ultra-flexicable (HiCoFlex®, HIGHTEC MC AG) was flip chip bonded together to the cable and interposer at both ends using a thermosonic flip chip bonder (Fineplacer Lambda, Finetech). In this process, conductive ball bumps (80 µm solder balls with 60 µm height) are deposited with a solder bumping machine (PacTech) on the flexicable. The solder balls on the flexicable are then flipped to face the pads of the probe (top of flexicable) or interposer (bottom). Controlled collapse chip connection (C4) was used where the solder balls were reflowed (by heating bumps above 250 °C) to partially melt the solder ball and establish an electrical connection between flexicable and interposer or neural probe pads. An electrically insulating adhesive was then underfilled to fill in the small space in between the bonded surfaces and bump

bonds. This underfill layer also helped to mechanically strengthen the connection between the flexicable, probe, and interposer. Some advantages of the flip chip assembly versus wire-bonding are the resulting flip chip connection area is much smaller as the chip sits directly on the circuit and can accommodate high numbers of connections (256 channels) to the narrow probe head. Pads on the edges of the interposer were then wire bonded with gold bond wires to the 256-channel PCB (PCBway). Wire bonds were then encapsulated with a UV-curable epoxy (Epoxy Technology OG116-31/3CC).

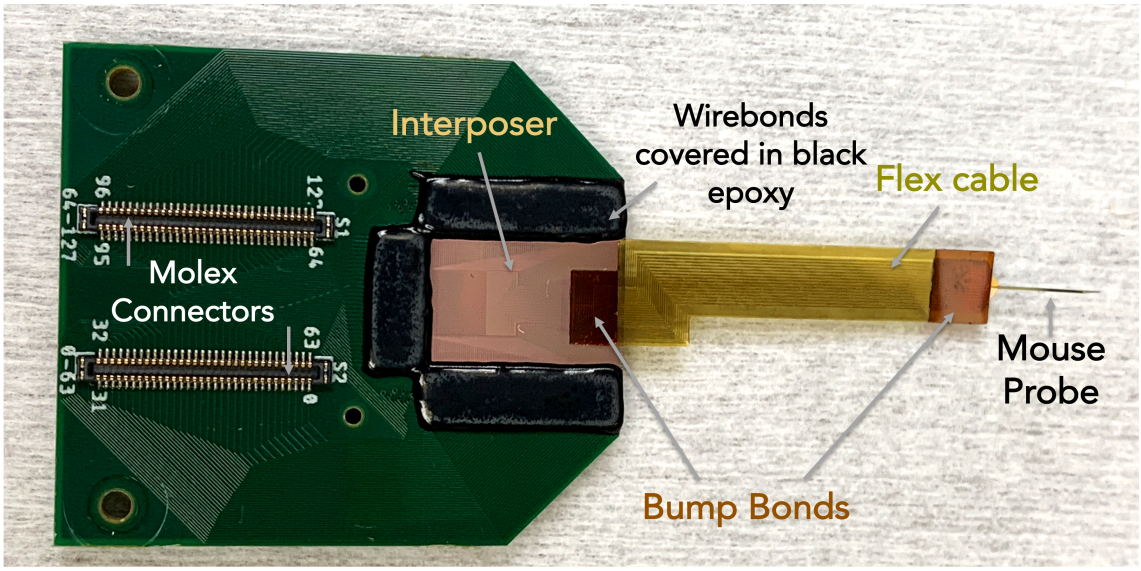

Figure 4.2: 256-channel passive PCB connecting rodent neural probe.

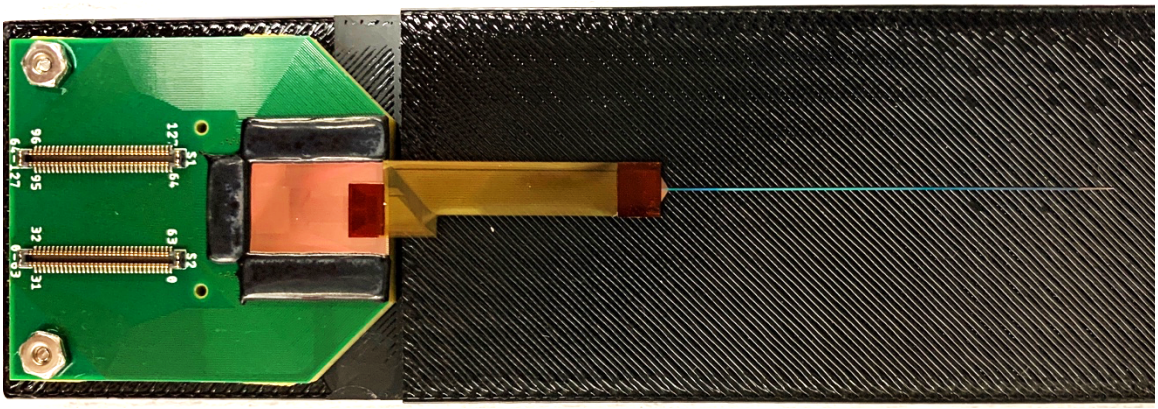

Figure 4.3: 256-channel assembly connecting non-human primate (NHP) probe assembly.

To connect 256-channel assemblies to backend recording electronics, two 128-channel headstages (Intan RHD 128-channel recording headstages), each with two 64-pin connectors (Molex SlimStack 502426-6410), were connected to a custom designed 256-channel connecting PCB via mating connectors (Molex SlimStack 502430-6412) (Figure 4.4 and 4.5).

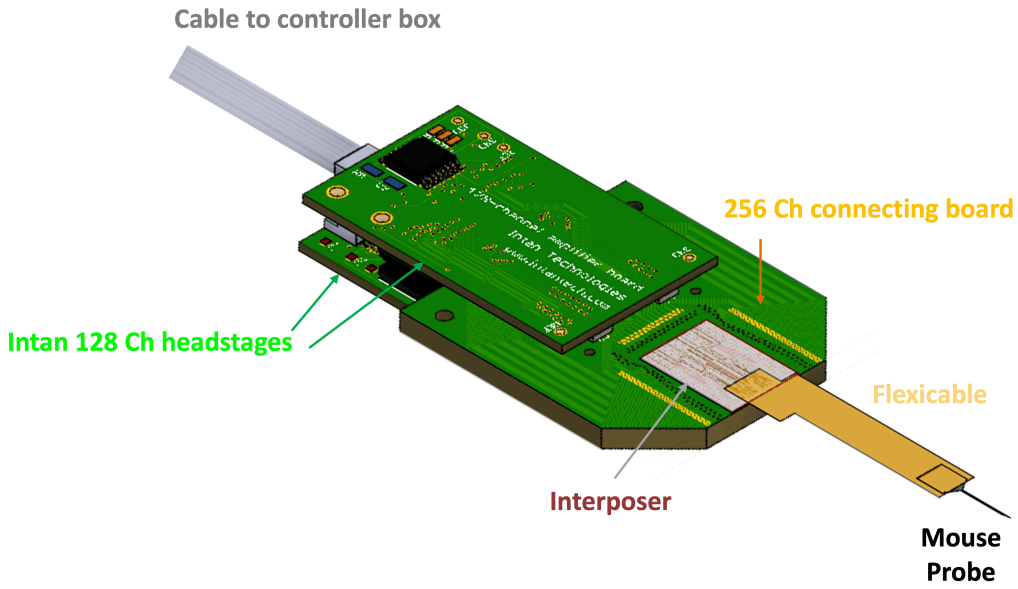

Figure 4.4: 256-channel rodent probe assembly.

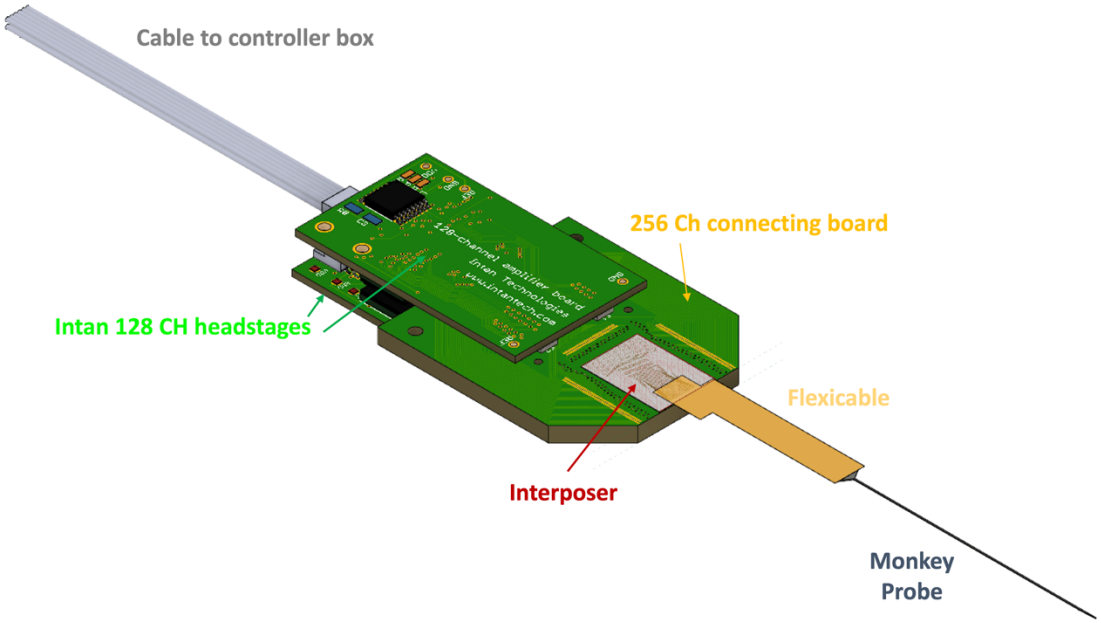

Figure 4.5: 256-channel non-human primate probe assembly.

4.4 Electroplating

The probe was electroplated to increase the surface area to volume of the electrodes. The layers of nanoporous gold formed during electroplating help increase the effective surface area of each pad, thus reducing the electrode impedance and crosstalk. This is especially important to ensure a high signal to noise ratio, which is necessary for single unit isolation of neuron activity.

To electroplate neural probe electrode pads, gold plating solution (SIFCO, Item # 80535500) was used. A constant voltage of –1.8V to –2V was applied for 1 second to each site until the target impedance of 300 kΩ or below was reached using a commercially available electroplating system (Intan Electroplating Board, Part #C3180). A wire soldered to the REF hole of the headstage was connected to an Ag/AgCl pellet and dipped into the electroplating solution as a reference during electroplating. Successful electroplating was

confirmed visually by the formation of a black nanoporous gold layer on each electrode and a decrease in impedance to 300 kΩ or less (Figure 4.6 and 4.7a).

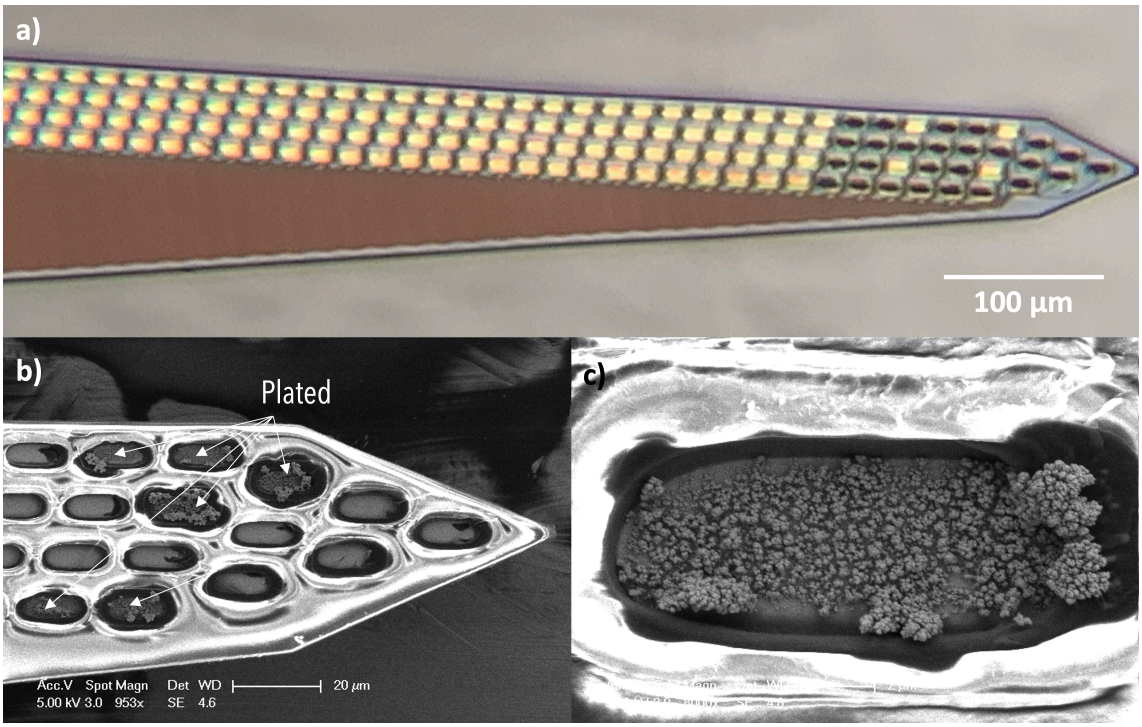

Figure 4.6: Neural probes with unplated and plated sites. a) Plated (*black*) and unplated (*yellow*) sites. b-c) Scanning electron microscope images of neural probe shank with unplated and plated sites. Roughened surface indicated the deposition of the nanoporous gold layer during plating. The parylene layer is shown as a smooth, light, gray layer around the electrode pads.

4.5 Electrical characterization

To quantify electronic noise, we measured the impedance of the electrodes at various frequencies (30 to 5000 Hz) and root mean square (RMS) noise from 3 Hz to 10 kHz (Figure 4.4). After plating, the impedance of each electrode on the neural probe decreased by more than 100-fold from an average of approximately 10 MΩ to 100 kΩ measured at 1 kHz frequency (Figure 4.7a). The RMS noise was also decreased from 50-200 µV before

electroplating to around 3-5 μV after electroplating as measured from 3 Hz to 10 kHz (Figure 4.7b).

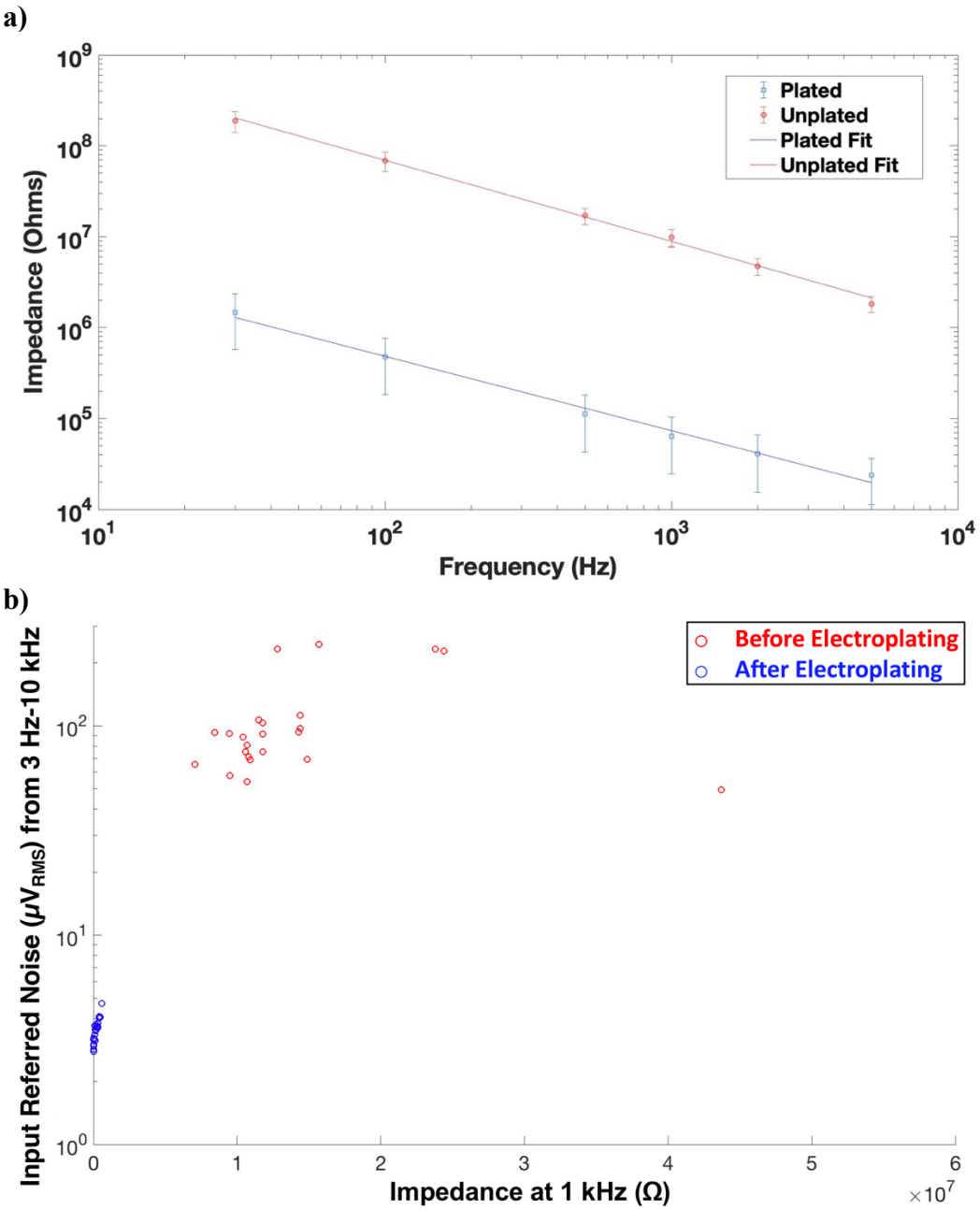

Figure 4.7: Electronic characteristics of Caltech/LETI probe. a) Impedance measured at various frequencies of neural probe electrode sites before (orange) and after (blue) electroplating. b) Decrease in input noise (μV_{RMS}) as measured from 3 Hz to 10 kHz bandwidth after electroplating. Plot of impedance measured at 1 kHz versus input noise. Electroplated sites are shown as blue dots and unplated sites are shown as red dots.

Table 1: Characteristics per shank of Caltech probe versus other state of the ephys technologies.

	Neuropixel[1]	Neuronexus (A1x32-Poly3)[2]	UCLA (64H or 128K)[3]	Neuralink[4]	Caltech/ LETI
Shank length	10 mm	5 mm	7 mm	20 mm	6 mm
Shank width	70 μm	62-114 μm	80 μm	5-50 μm	56-172 μm
Thickness (at tip)	20 μm	15 μm	23 μm	4-6 μm	21 μm
Electrode Size	12 x 12 μm	15 x 12 μm	23 x 85 μm	14 x 24 μm	6 x 14 μm
Electrode Pitch	20 μm	22-25 μm	22.5 μm	50 or 75 μm	20 μm
Number of Channels	384 (192 active at time)	32	32	32	256
Recording span	1.9 mm	275 μm	330 μm	~1.6 mm	1.5 mm
Electrode Density (per 100 μm)	10.1 active electrodes	11.6 electrodes	9.7 electrodes	2 electrodes	17.1 electrodes
Impedance (at 1 kHz)	148 ± 8 kΩ	50–100 kΩ	300 kΩ	36.97±4.68 (PEDOT) 56.46 ± 7.10 kΩ (IrOx)	≤ 300 kΩ
Input referred noise (3 Hz-10 kHz) μV_{RMS}	5.4-7.2	5.2-5.9	2-3	5.9	3.3-5

1. (Steinmetz et al., 2021)
2. (Fiáth et al., 2021; Hetke, 2022; Neto et al., 2016)
3. (Du et al., 2011; Masmanidis, n.d.)
4. (Musk, 2019)

4.6 Conclusion

In conclusion, we describe 256-channel and 32-channel assemblies that have similar electronic characteristics to other state-of-the-art ephys systems and whose packaging enables integration with micromanipulator systems. We also demonstrate successful electroplating and confirm successful reduction of noise to levels below the noise floor of

brain signals (>10 μV_{RMS}). Additionally, the level of electrical noise is either equal or below that of other commercially available ephys probes (Table 1). This illustrates successful design and function of 256-channel and 32-channel assemblies comparable to other existing state-of-the-art ephys systems.

Chapter 5

IN VIVO RECORDING SETUPS WITH IMAGING SYSTEMS

5.1 Introduction

Electrophysiology recording with neural probes combined with confocal or two-photon imaging modalities enables recording of neuron activity and localization of neurons in anatomical space. A key advantage of two-photon (2P) laser scanning microscopy is that it enables imaging of structures at high spatial resolution in light scattering tissues, such as the brain (Moreaux et al., 2020). By combining dense ephys recording with two-photon imaging using our setups, we can better achieve our goals of 1) full volumetric coverage of the neural probe's detection abilities, 2) quantification of volumetric displacement caused by probe implantation in the brain, and 3) combined extracellular ephys recording with two-photon imaging in optogenetic mice lines that we describe in later chapters. Volumetric structural imaging of neurons and blood vessels also enables us to monitor displacement of the brain tissue and vasculature changes following probe implantation (Fan et al., 2020) as we describe in Chapter 7. Additionally, combining extracellular recordings with free-space imaging of mice expressing fluorescent calcium, optogenetic, or voltage reporters enable functional imaging of neuron circuitry at sub-cellular resolution (Moreaux et al., 2020) as we demonstrate in Chapter 8.

In this chapter, we describe three *in vivo* recording setups used to test the quality of ephys recording from the neural probe with concurrent widefield and two-photon imaging. We also outline the data processing workflow for analyzing and accessing the quality of the collected ephys data. The first setup enabled quick neural probe recording and adjustment of

anesthesia levels. The second setup enabled widefield imaging with the mouse head stabilized with a head-fix piece affixed to the microscope platform. To enable concurrent imaging with ephys recording, we developed a customized head-fix piece that would enable insertion of the probe into the mouse brain directly under the imaging window, so that it would be possible to image the probe and the surrounding tissue while collecting neighboring ephys activity. The third setup enabled two-photon imaging with simultaneous ephys recording of imaged brain regions. Lastly, we describe our analysis platform to examine the quality of *in vivo* recordings.

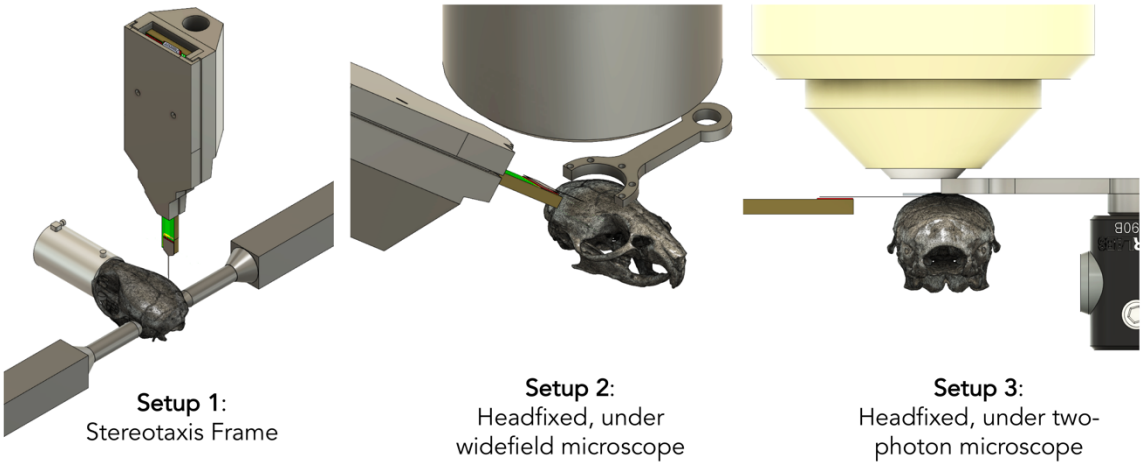

Figure 5.1 Recording setups.

5.2 Animal procedures

All procedures were approved by the California Institute of Technology Institutional Animal Care and Use Committee (IACUC) and Institutional Biosafety Committee (IBC). Male mice (GIN, strain code: 003718, Gad2-IRES-Cre; strain code: 010802; and *VGAT-ChR2-EYFP* line 8, strain code: 014548) were purchased from the Jackson Laboratory (JAX). AAV vectors (pAAV-EF1a-double floxed-hChR2(H134R)-EYFP-WPRE-HGHpA;

Addgene, 20298-PHPeB) were administered through injection in the retro-orbital sinus of adult mice (4-5 weeks of age) following three days of acclimation in the animal facilities after transportation (Chan et al., 2017). Mice were injected with 10^9 genome copies (GC) per mouse in a total volume of 80 μL. Imaging experiments were performed 3 to 5 weeks following injections to allow time for transduction of vector payload to target cells and subsequent transgene expression prior to initiating experiments.

5.3 Surgical procedures

Mice were anesthetized with 1-2% isoflurane, head-fixed in the stereotaxic apparatus (Neurostar robot stereotaxic alignment system), a 3 x 3 mm craniotomy was created by drilling over the designated coordinates on the mouse's skull (Pak et al., 2015), and a coverslip was affixed over the craniotomy. An additional smaller craniotomy was drilled over the right posterior cortex for placement of the electrical Ag/AgCl pellet reference wire (WPI or Biomed Products Inc).

5.4 Description of setups

5.4.1 Setup 1: Quick probe testing with adjustable levels of anesthesia

In this setup, the time taken to mount the head-fix piece was minimized since the ear bars hold the skull in position on the stereotaxis frame. A drill mounted on the stereotaxis frame was used to create craniotomy holes in the skull for probe insertion and reference. The probe was inserted vertically at our targeted brain area and the depth was controlled using a micromanipulator. The mouse was concurrently administered isoflurane via a nose cone to induce and maintain general anesthesia during the surgery.

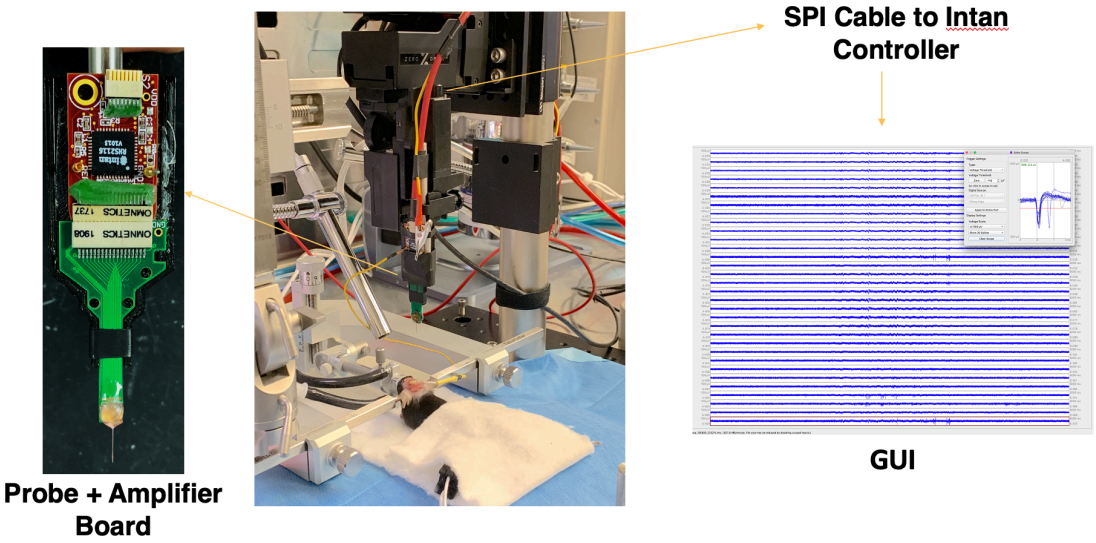

Figure 5.2: Recording setup. Probe with amplifier board mounted to holder connected to a micromanipulator. The amplifier board is connected to a recording controller for recording and visualization of electrophysiology signals.

5.4.2 Head-fixation strategy imaging setups (for setup 2 and 3)

To image the probe with the surrounding brain volume it records from, we developed a special recording setup that required the creation of a custom head-fix piece. While other strategies exist to combine electrophysiology readings with two-photon imaging in head-fixed mice, they either involve the use of transparent surface electrodes, or the ephys probe is inserted vertically or at an angle to the imaging area (Buzsáki, 2022; Groblewski et al., 2020). In contrast, our head-fixation strategy allows for concurrent visualization of ephys probes and the surrounding tissue (Table 2).

Table 2: Comparison with other head-fixation systems combining electrophysiology with imaging.

	RODIN or Brain Observatory Headframe (Buzsáki, 2022; Groblewski et al., 2020)	**This work**
Probe insertion orientation	Vertical to coverslip	Parallel to coverslip
Coverslip position	Top or side of the skull	Lateral side of skull (right) (Centered at -1.82 AP and -2 ML and 0.29 DV coordinates)
Visualization of the entirety of inserted probe shank	No	Yes
Ephys recorded brain regions	Visual/auditory sensory fields (Distal region not under imaging window)	Cortex (Layer 1 and 2) directly under imaging window

Our head-fix piece was designed to attach to the microscope platform to stabilize imaging during recording. To avoid obstructing the objective lens during imaging, a low-profile head-fix piece (1.46 mm) with a wide opening (9.57 mm) was designed (Figure 6.3). Additionally, the piece was made of stainless steel so it would be lightweight, strong, and resistant to corrosion. A hole on back end of the head-fix piece was designed to accommodate a screw which tightened into the microscope platform attachment arm. To enable insertion of the probe laterally during imaging, the head-fix piece was designed to be open on one side to allow for an open port through which the probe could be inserted.

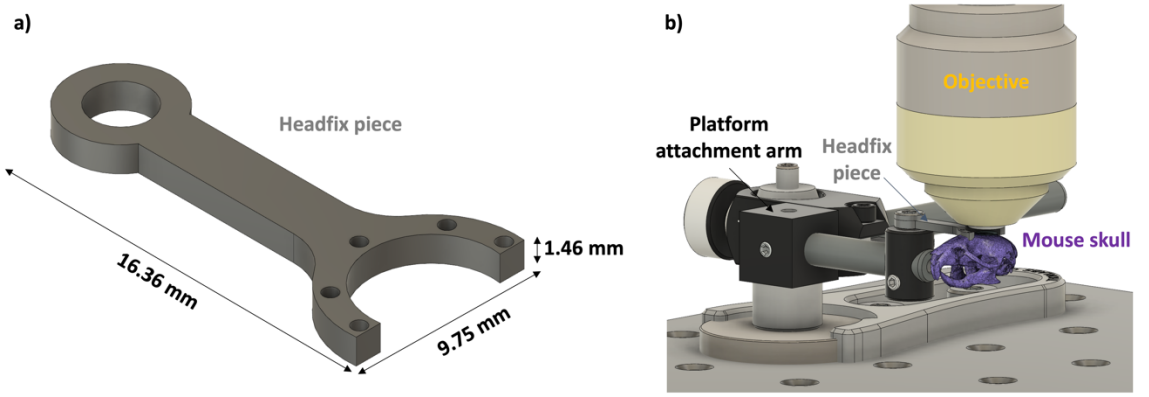

Figure 5.3 Head-fix piece. a) Dimensions of head-fix piece. b) Attachment of head-fix piece to skull and microscope platform.

5.4.2.1 Head-fix piece attachment procedure

A stainless-steel head-fix piece was affixed to the left side of the skull opposite the coverslip using dental cement to minimize head movements during imaging. The head-fix piece was then attached to the stage of the microscope imaging platform. Urethane was used to anesthetize the mice for the remainder of the experiment The urethane was diluted to a concentration of 0.1 g/1 mL in sterile saline. The urethane solution was administered using an intraperitoneal injection with a 25-gauge needle at a concentration of 1.3 grams of urethane per 1 kg of the mouse's body weight. To confirm proper anesthetization of the animal, pedal withdraw reflex (pinching the foot on both feet), eye blink reflex, and tail pinch response were tested, along with monitoring of SpO2 and respiratory rate and depth. The animal was then placed under a two-photon microscope (Thorlabs, Inc.) and imaged using a Leica 25X water immersion lens (Leica HCX IRAPO). To elicit a spike emitted from a point source, we used blue light stimulation of ChR2 with a two-photon wavelength set at 960 nm (250 kHz).

5.4.2 Setup 2: Widefield imaging with probe insertion

To maintain the position of the skull during imaging, the head-fix piece was fastened to the skull, and then screwed into a platform under the confocal lens. A 2 x 2 mm craniotomy over the target region was performed to allow for probe insertion.

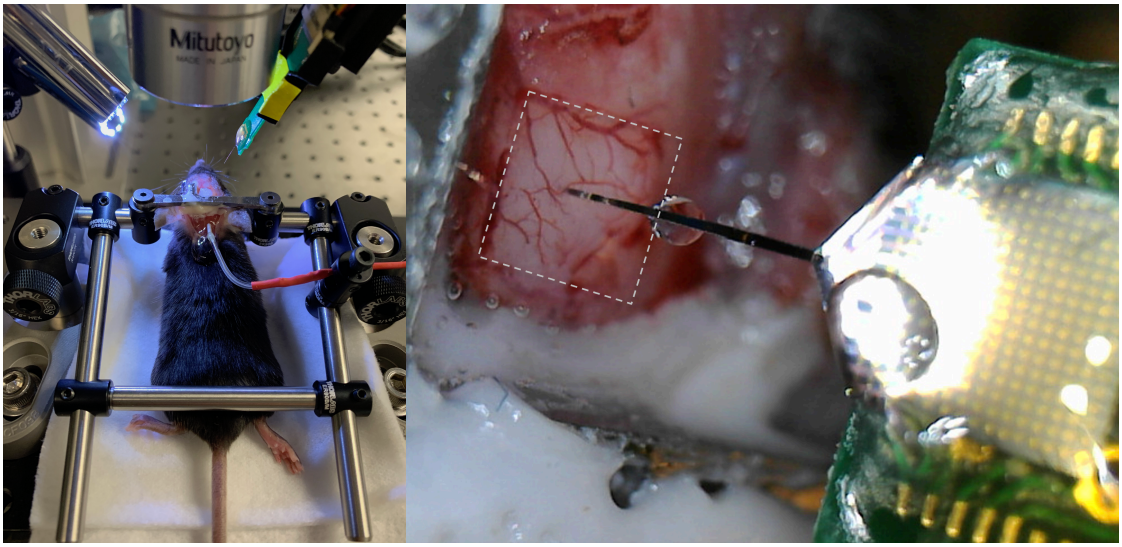

Figure 5.4 Widefield imaging with ephys probe.

5.4.3 Setup 3: Two-photon imaging with simultaneous ephys probe recording

5.4.3.1 Two photon considerations: imaging at depth

Scattering and absorption of excitation light in the biological tissue limits the delivery of ballistic, unscattered light necessary for imaging at depth. This makes it difficult to achieve sufficient excitation necessary to visualize deeper regions of the brain. Nonlinear optical microscopy, such as two-photon microscopy, helps overcome this issue because even scattered signal photons can be assigned to their origin as the result of localized nonlinear signal generation (Helmchen & Denk, 2005); thus providing a deeper depth of imaging than confocal imaging. By taking the absorption of the tissue into account, a near infrared laser will have a maximum attenuation length of approximately 500 μm (Moreaux et al., 2020).

The maximum depth the 2P laser can excite can be further raised by increasing the instantaneous laser and reducing the pulse repetition rate, thus minimizing the average power delivered to the tissue (Moreaux et al., 2020). These methods allow imaging of neuronal soma in the L5 region up to ~800 μm below the surface (Mittmann et al., 2011).

Taking the maximum depth that can be imaged into consideration, we planned the craniotomy, insertion area, orientation of the probe, and coverslip so that the probe would be inserted no more than 500 μm from the surface of the coverslip.

5.5 Craniotomy and surgery to create optical viewing window

A 3 x 3 mm craniotomy was performed over the target area (centered at -1.82 AP and -2 ML and 0.29 DV coordinates relative to bregma) using a drill mounted to the stereotaxis frame (Neurostar Robot Stereotaxic System). A coverslip was then affixed over the target area using dental cement, with a small lateral port left unglued to allow for ephys probe insertion. Wax was used to create a well around the coverslip to maintain saline immersion during imaging (Figure 5.6). Next, a head-fix piece was fixed to the skull opposite to the craniotomy to minimize head motion during imaging. This imaging setup can also be used to test for probes like photonics probe and combine probe recording with two-photon imaging of the same brain region. The two-photon setup utilizes a special objective with high free working distance (3.5 mm) and widefield of view. The probe was inserted shallowly under coverslip with the micromanipulator (Figure 5.5 and 5.6).

5.5 Acute *in vivo* recording set-ups

The probe assembly was attached to an ultraprecise micromanipulator (Sensapex uMp) and inserted parallel to the coverslip into Layer 2 or Layer 3 of the cortex. The probe was gradually inserted until clear electrophysiological signatures from the cortex were

observed (spiking and ripple oscillations). After surgery, the mouse was injected with the terminal anesthesia, urethane at a dosage of 1.3 g urethane per 1 kg mouse body weight through the intraperitoneal cavity. Urethane, in comparison to isoflurane, preserves the spike burst activity and spontaneous slow oscillations (up/down states) in the cortex (Wanger et al., 2013; Yagishita et al., 2020). After proper depth of anesthesia was established, the mouse was transferred to the imaging platform of the two-photon microscope.

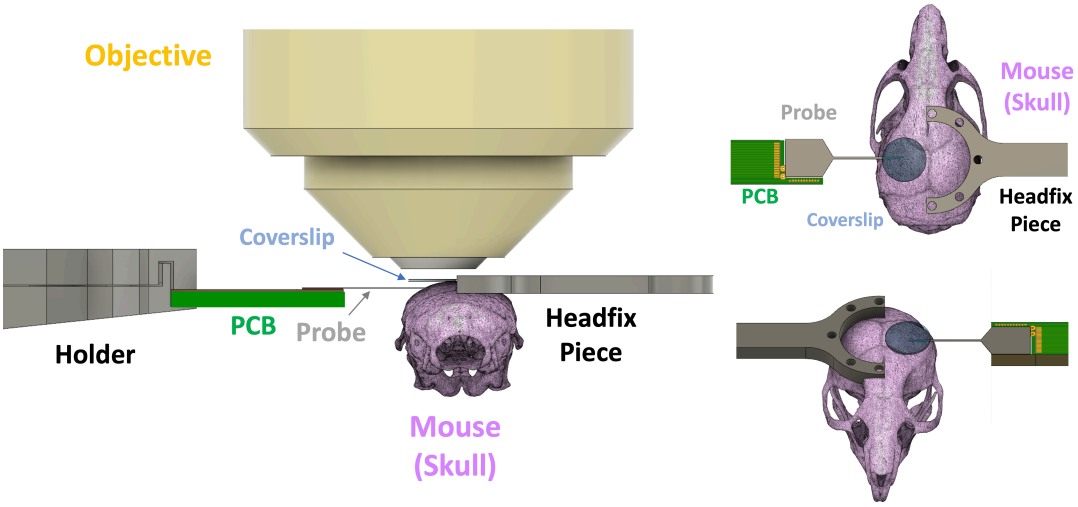

Figure 5.5: Model of two-photon setup with inserted ephys probe. Mouse skull is shown in purple. Setup enables simultaneous ephys recording with two-photon imaging.

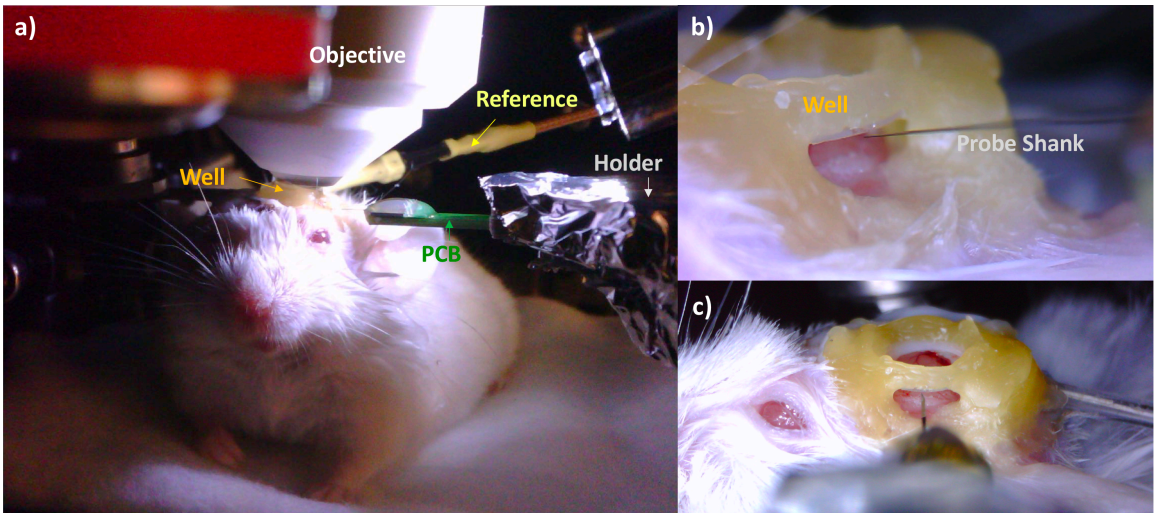

Figure 5.6 Two-photon imaging setup with mouse during imaging. a) Two-photon imaging setup with ephys probe inserted under imaging window. b) Side view with probe shank inserted shallowly under coverslip. c) View down probe shank inserted under coverslip.

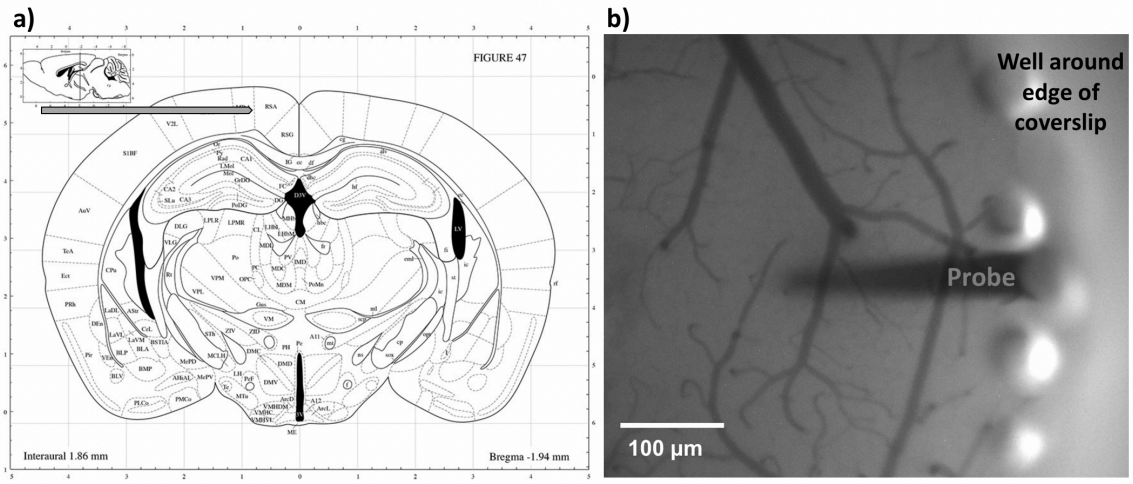

Figure 5.7: Insertion of probe into cortex. a) Position of inserted probe in mouse brain represented by Mouse Brain Atlas (Franklin & Paxinos, 2008). b) Image of probe inserted into brain under coverslip.

5.6 Demonstration of successful imaging of neural probe and surrounding neurons *in vivo*

Successful imaging of the neural probe and the surrounding tissue was confirmed with two-photon imaging. First the probe was positioned to insert into the targeted stereotaxic coordinates according to the mouse brain atlas (Figure 5.7a). The position of the probe was

monitored with brightfield illumination and a 4X objective (Nikon Plan Fluor 4X Objective) (Figure 5.7). As the probe was inserted shallowly (~200 μm), the outline the probe could be seen with bright field illumination, which helped us track position of the probe during insertion. Once the target region of the brain was reached, we switched the objective to the Leica 20X objective and imaged the area using two-photon microscopy.

To test the effectiveness of this setup, we inserted our neural probe into a transgenic mouse model whose interneurons expressed GFP (GIN, Jackson Laboratory, strain #003718). Using this setup, we can clearly visualize the probe and the surrounding neurons labeled in GFP (Figure 5.8). The probe can be visualized using an infrared laser because of the photoluminescence from the absorption and emission of the two-photon NIR excitation laser by the gold on electrode pads causes the electrodes to appear red when imaged (Figure 5.8b) (Wang et al., 2005). The ability to map the surrounding neurons in proximity to the probe is especially important to benchmark the volumetric coverage of the probe and the damage the probe causes during insertion.

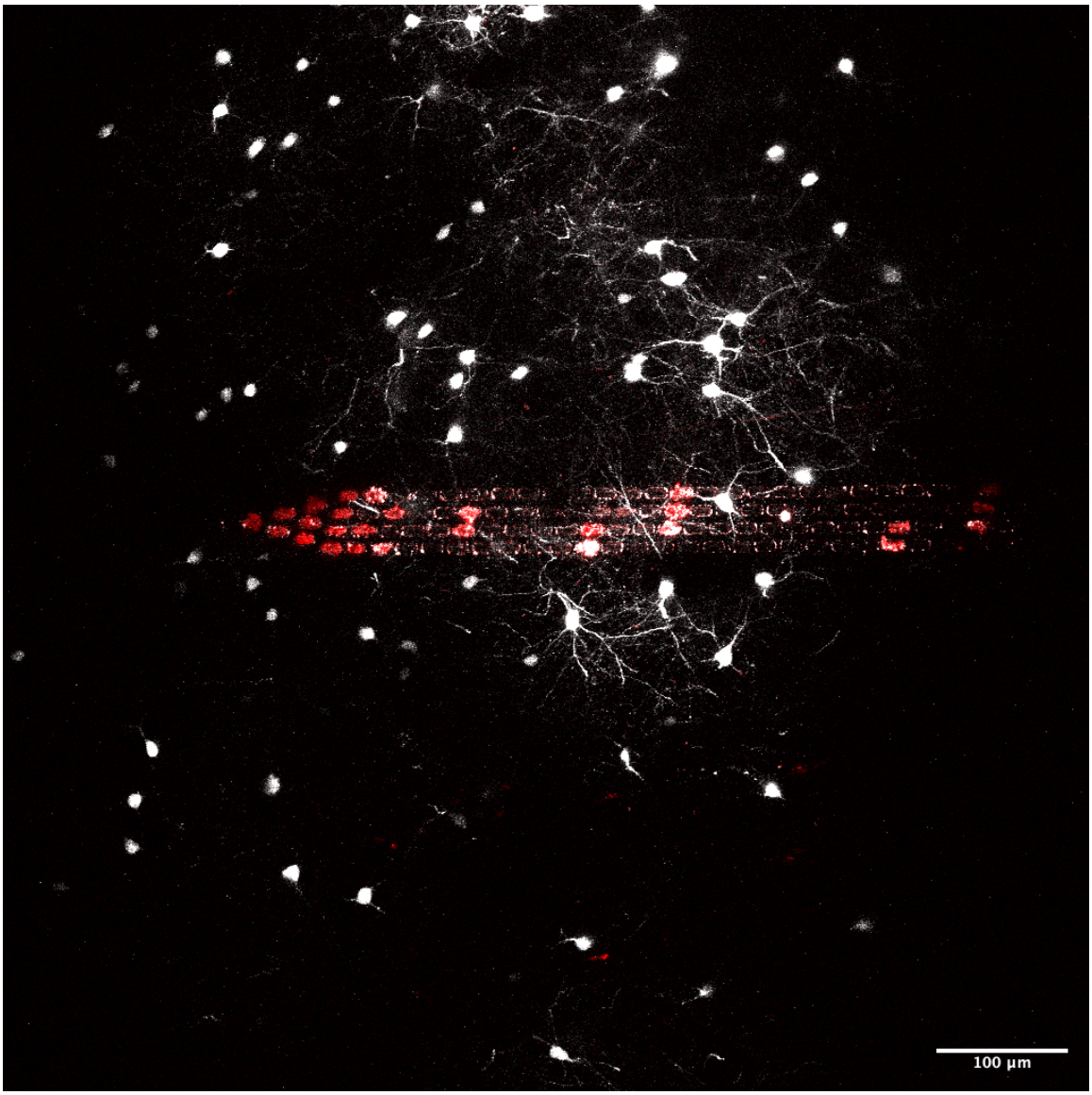

Figure 5.8: Representative image of ephys probe with stained neurons. Electroplated pads appear red and surrounding interneurons expressing GFP are white. Images were obtained via 2P setup *in vivo* when neural probe was inserted into Layer 1 of the cortex. Figure credit: Laurent Moreaux.

Table 3: Summary of Benefits and Drawbacks of Setups

	Advantages	Disadvantages
Setup 1: Mouse secured on stereotaxic frame with adjustable levels of anesthesia (isoflurane)	- Do not need to relocate animal - Do not need to attach head-fix piece - Easier to insert neural probe into targeted brain region with guidance from stereotaxic robot (Neurostar) - Adjustable isoflurane levels help control depth of anesthesia	- Does not allow imaging of the brain - Isoflurane preserves less of the brain activity than urethane (Shumkova et al., 2021)
Setup 2: Headfixed mouse with widefield imaging	- Allows for imaging of brain during probe insertion - Urethane preserves more of brain activity than isoflurane (Shumkova et al., 2021)	- Requires attachment of headfix piece - Cannot adjust depth of anesthesia
Setup 3: Headfixed mouse with two-photon imaging	- Probe is inserted parallel to coverslip and allows for imaging of the implanted probe shank - Allows for imaging of inserted probe and surrounding brain tissue - Urethane preserves more of brain activity than isoflurane (Shumkova et al., 2021) - Two-photon imaging allows for visualization of deeper brain regions (~500 μm) than confocal imaging	- Requires attachment of headfix piece - Cannot adjust depth of anesthesia

5.7 Data Acquisition Workflow

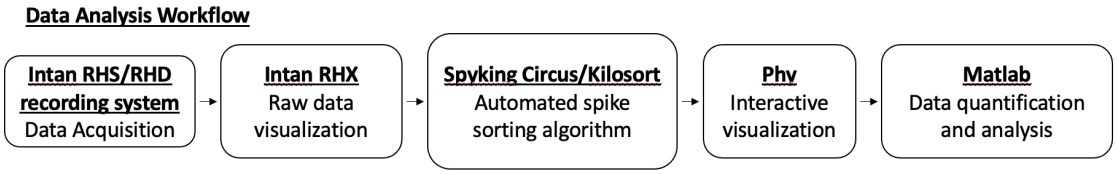

To assess the neural probe's ability to record surrounding electrophysiological activity, we used backend software to visualize the acquired data and quantify and analyze neuron spiking activity. First, ephys recordings were collected by either the Intan RHS or RHD headstage and acquired via the Intan RHS/RHS recording system. Raw data was notch filtered at 60 Hz. For LFP band data, a low pass filter with a 3rd order Butterworth filter at 250 Hz was applied with the amplifier bandwidth between 1.76 Hz to 9.99 kHz. For spike data, a high-pass filter with a 3rd order Butterworth filter cutoff at 250 Hz was applied with the amplifier bandwidth between 0.3 to 7 kHz. Data was then exported as a raw data (dat) file to Spyking Circus or Kilosort software where thresholding, merging, whitening, and clustering steps were performed (Pachitariu et al., 2016; Yger et al., 2018). To ensure the quality of the waveform clusters and remove noise or join similar waveforms, Phy was used. Lastly data was exported to Matlab for further quantification of signal and noise.

5.8 Conclusion

This chapter describes three different set-ups for *in vivo* ephys studies, summarizes the advantages and disadvantages of each setup (Table 3), demonstrates successful visualization of the probe and surrounding tissue (Figure 5.8), and outlines the workflow for ephys data acquisition and analysis. This imaging modality enables direct examination of probe damage and correlation of spiking activity to the position of labeled neurons (Chapters

6 and 7). This imaging setup can also be used for testing of other neural probes such as optical probes with detector or emitter pixels under two-photon imaging as proposed in recent literature (Moreaux et al., 2020).

Chapter 6

MAPPING NEURONS WITH JUXTA-POSITIONAL RECORDINGS COMBINED WITH TWO-PHOTON IMAGING *IN VIVO*

6.1 Introduction

In this chapter, we describe our analysis to benchmark the detection limits of the neural probe and isolate single unit activity. Using this information, we deterministically map the position of each neuron relative to the probe based on extracellular spiking activity detected on our ephys neural probes. To address this goal, we used spike sorting to isolate spike waveforms, examined the ability of our dense electrode arrays to determine the location of neurons, and demonstrate our ability to map single neuron units with concurrent two-photon imaging *in vivo*.

6.2 Theoretical distance dependence of extracellular measurements

Extracellular recordings measure the electrical potential induced at an electrode by neuron currents. These electrical potentials are generated as a result of neuronal activity that generate transmembrane currents and transient electrical potentials, which spread and travel through the extracellular medium (Buzsáki et al., 2012). The recorded local field potential (LFP) signal represents the change in the electrode's potential induced by all local currents (Buzsáki et al., 2012). In contrast, the spike activity depends on the depolarization of the membrane potential of the neuron (Yi et al., 2015). Thus, LFPs are believed to represent the synchronous input of activity in an area, while spikes are thought to represent the output (Buzsáki et al., 2012; Denker et al., 2007).

Putting this together conceptually, the relationship of the induced electrical potential to distance can be approximated by a point source equation that considers the extracellular fluid conductivity, magnitude, sign, and location of current (Buzsáki et al., 2012). The summation of multiple potentials can be measured as the voltage (V_e) (Gold et al., 2006; Michalikova et al., 2018).

$$V_e(r_e, t) = \frac{1}{4\pi\rho} \sum_{n=1}^{N} \frac{I_n(t)}{|r_e - r_n|}$$

Equation 6: The point source equation.

In this equation, V_e is the electrical potential induced at the electrode, $I_n(t)$ is the nth point current source, $r_e - r_n$ is the distance between the point source (r_n) and recording electrode (r_e), N is the number of individual point sources, and ρ is the extracellular conductivity (Buzsáki et al., 2012).

A major inaccuracy of the point source equation is it fails to consider the complex geometry of neurons. This is a major limitation because every part of the neuronal membrane can create action potentials and the extent of the somatodendritic back-propagation of action potentials varies by excitatory and inhibitory inputs to a neuron (Buzsáki, 2004). To support this point source assumption, it is assumed that the extracellular potential generated by membrane currents are weak and can be neglected, while the soma's contribution dominates so that the neuron can be treated as a point source (Michalikova et al., 2018). Due to these limitations, it is important to benchmark how accurate point source estimates are compared to the actual *in vivo* data where we know the actual position of neurons relative to the electrode and their induced electrical potential at the electrode.

6.3 Quality of ephys recording and mapping of neuron locations in literature

Literature suggests that most neurons (with an amplitude above 50 μV) can be recorded at a maximum of >100 μm away from the soma (Du et al., 2011; Henze et al., 2000), while theoretical models suggest that the limits of detection are closer to 50 μm (Table 4) (Somogyvári et al., 2012). This discrepancy can be attributed to the type of neuron and orientation of the recording sites used in the studies (Anastassiou et al., 2015). For example, if the probe is positioned along the axis of the pyramidal cell, the extracellular action potential can be recorded up to 400 μm from the cell body of individual layer V pyramidal neurons due to backpropagation of action potentials along the dendritic arbor (Buzsáki & Kandel, 1998). In contrast, if the probe is positioned perpendicular to the major axis of the neuron, the extracellular action potential will decay more rapidly over longer distances (Neto et al., 2016). In ground truth measurements with patch clamp readings alongside juxtapositional extracellular readings *in vivo* using 32-channel ephys polytrode probes, spikes from neurons can be detected at maximum 50 to 150 μm from the probe surface (Neto et al., 2016) (Table 4). *In vitro* whole cell patch clamping with cortex brain slices paired with 32-channel probes also detect neurons at maximum 150 μm away from the electrode (Anastassiou et al., 2015) (Table 4).

Additionally, the brain region determines the cellular density around the probe and thus the maximal number of neurons each electrode can record from. If we consider the cellular density of the cortex (with an average of 40,000 to 60,000 neurons/mm^3) (DeFelipe et al., 2002) and assume that the limits of detection for each probe is 50 μm, we expect that each electrode site should theoretically be able to record from approximately 10 to 15

neurons (Neto et al., 2016). The highest density of neurons in the mouse brain is in the visual cortex with a density of 155,000 cells/mm^3 (Herculano-Houzel et al., 2013; Keller et al., 2018). Thus, in the mouse brain, a theoretical maximum of 39 neurons can be detected per electrode site. The large density of neurons in these regions of the brain emphasizes the need to have dense electrode arrays able to properly resolve and detect the activity of these closely spaced neurons.

Our neural probe with dense electrode arrays will enable dense sampling of the extracellular electric fields, so that the signal of each neuron can be detected by multiple individual electrodes. This allows for detection from greater distances than previous studies and enables a high-resolution recording of the spatiotemporal profile of a neuron's extracellular action potential. Since the signal is detected on multiple pads, we can cross-validate the data and ensure that the signals detected are not noise. This detailed profile will enable better detection and isolation analysis, and help identify individual neurons near the probe with downstream spike sorting to cross-validate our analysis (Rossant et al., 2016).

Table 4: Ground truth measurements: map neurons with juxtapositional recordings

Method	Description
Cross-validated 32-ch ephys polytrode probe with patch clamp *in vivo* (Neto et al., 2016)	Twenty juxta-extracellular pairs were recorded with both 32 and 128-channel polytrodes in cortex (800 to 1,800 μm from the pial surface). Large peak-to-peak amplitude waveforms were observed < 50 μm from nearest electrodes, while smaller magnitude spikes (5-38 μV) were observed 50-150 μm from the probe (Neto et al., 2016).
Whole patch clamp recording with *in vitro prep* (brain slice) with 32-channel probe (Anastassiou et al., 2015)	Rat somatosensory cortex slice was whole cell patch clamped (for intracellular recording) and silicon probe was positioned nearby to record corresponding extracellular voltages for spike frequencies under 20 Hz. At farthest the spike can be detected 150 μm away from the electrode. Decline of extracellular amplitude as a function of distance from the soma can be fitted to $R = \frac{V_e}{I} = \frac{\rho}{4\pi r}$ (Anastassiou et al., 2015).
Concurrent two-photon imaging with 32-channel extracellular recordings*	This work. Maximum detection distance is 168 μm from estimated position of neuron soma (Figure 6.9).

6.3.1 Importance of site density to spatially sample individual neurons

High-density electrode probes enable high coverage recording of neuron's field potentials, which in turn enable single-unit discrimination of individual neurons (Blanche et al., 2005). Spatial sampling of individual neurons reveals differential spike amplitude of each unit across electrodes to provide more reliable resolution of single neuron isolation by their activity. To fully capture this activity and enable single neuron isolation, the recording sites need to have sufficient density and be configured in such a way to unambiguously resolve the activity of individual neurons across multiple electrodes sites. For areas of the brain with limited spatial field potentials, such as the interneurons of the rodent hippocampus, literature suggests an electrode spacing of < 50 μm for adequate

spatial sampling (Blanche et al., 2005). Thus, our probe with a pitch of 20 μm between electrodes should be more than dense enough to capture the surrounding neurons' field potentials.

6.3.2 Benchmarking spike and recording quality

To quantify the ability of our neuron to capture single neuron activity and the detection range of our probe, we assessed the following parameters: 1) the recording quality of electrodes and noise during recording, 2) waveform quality of recorded spikes, and 3) how many distinct spike waveforms are captured on each electrode.

6.3.3 Examining drift of probe relative to brain during recording

To examine the movement of the brain relative to the probe, we looked at the drift over the duration of the recording. Drift will lead to changes in the spike amplitude, cause changes in amplitude features over time, and in extreme cases cause loss of spike clusters in recording channels (Pachitariu, 2020). To examine the drift in our recordings, we used a drift map where spikes over time are represented as dots, with larger amplitude spikes represented as darker points (Figure 6.1a). In our recordings, the drift of spike batches over time is less than 15 μm (Figure 6.1b). A drift of 20 μm will move a neuron off the sites and cause spike clusters to appear to drop out of electrode channels (Steinmetz, 2022). Since our drift is less, the neurons do not drift and drop off the electrode channels during the duration of our recording, which is acceptable.

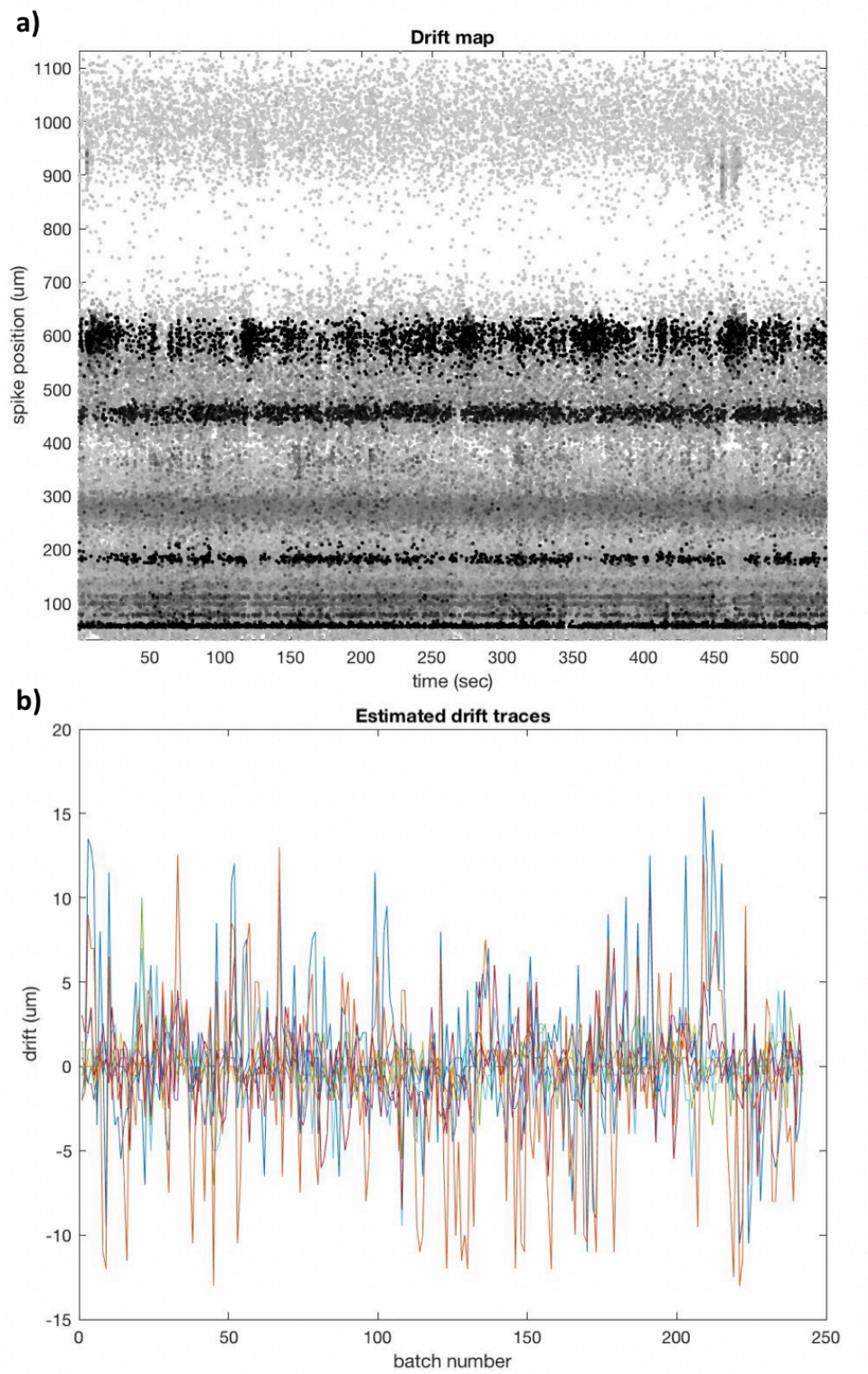

Figure 6.1: Minimal electrode drift during recording. a) Drift map of spikes over time as dots mapped by spatial depth. Larger amplitude spikes are shown as darker dots. b) Spikes batches have minimal spatial drift < ± 15 μm over the course of the recording.

To diagnose probe drift and its effect on detected waveforms, we used Kilosort 2 (Figure 6.2) (Pachitariu, 2020; Pachitariu et al., 2016). During drift correction, spikes are separated into batches by their spike template. The batches are then re-ordered by placing batches with similar drift positions next to each other and tracking incremental changes in the cluster's template through the batches. Since the similarity between batches is high and the templates do not appear to vary much over the different batches, there is likely little drift (Figure 6.2a) (Pachitariu, 2020; Pachitariu et al., 2016). After sorting, the slight changes in the waveforms of each neuron is used to adjust the templates and correct for drift (Figure 6.2a) (Pachitariu, 2020). After this adjustment, the waveform changed smoothly as a function of its drift position, which helped correct for drift (Figure 6.2b). Additionally, drift corrections help improve cluster separation by tracking neurons of similar waveforms as they shift along the probe (Pachitariu, 2020).

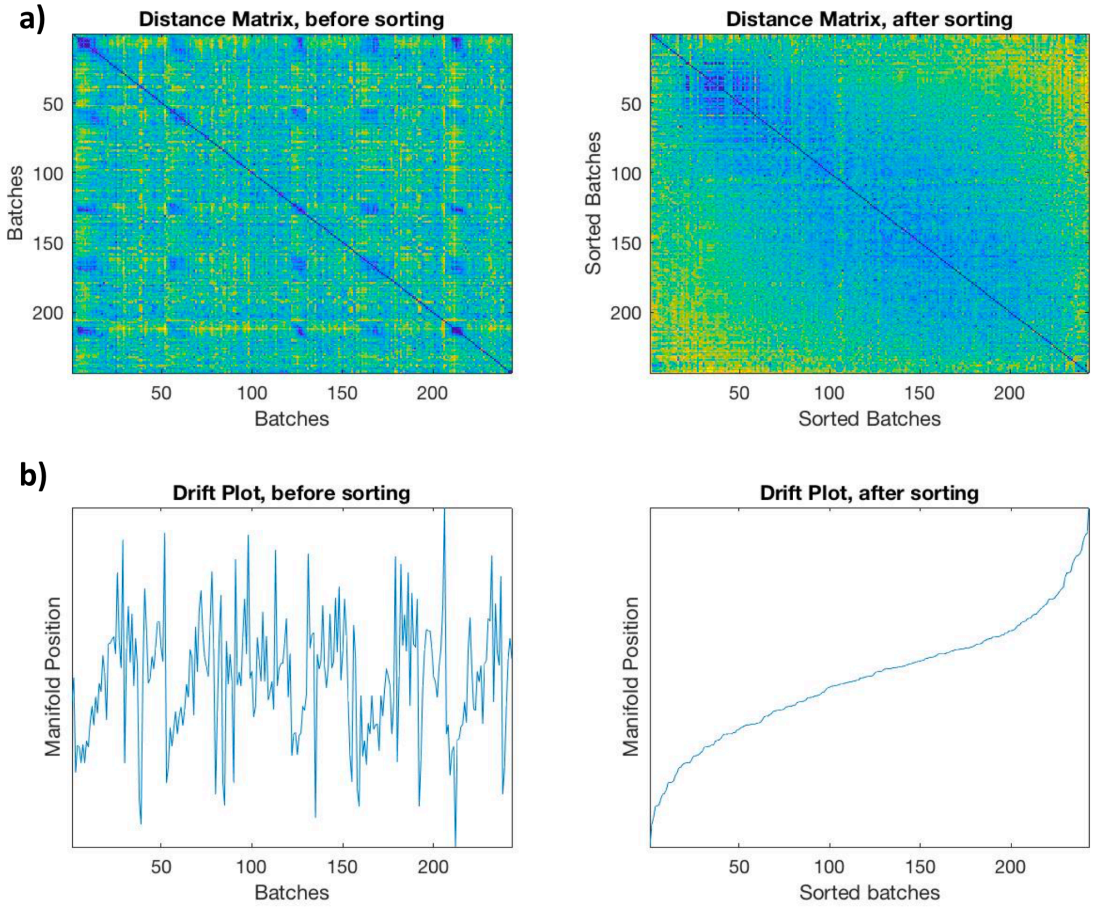

Figure 6.2: Drift correction to sorting. a-b) Drift map and corrections applied to spiking output (using Kilosort).

6.3.4 Temporal filtering and spatial whitening

Spatial whitening was applied across channels to remove spurious spatial noise from neurons far away from the probe (Figure 6.3). Spatially correlated noise arises from neurons far away from the probe with spike amplitudes that are too small to sort directly (Buzsáki, 2004; Neto et al., 2016). During preprocessing, spatial whitening removes correlation from channels caused by noise not arising from neuron signals; this step is critical to separate neighboring spike clusters (Chung et al., 2017). Temporal filtering is used to remove frequencies in the raw signal that are not of interest, which can help improve the signal-to-

noise ratio of the recording but when improperly applied leads to distortions or filtering artifacts (Widmann et al., 2015). Some examples of temporal filtering include high-pass filters that remove frequencies below a certain threshold, low-pass filters that remove high-frequency noise, notch filtering that remove powerline noise (50 Hz or 60 Hz), and band-pass filters that remove the signals outside the specific band of frequency ranges (de Cheveigné & Nelken, 2019). During temporal processing using Kilosort, temporal areas of the recording with no spikes are used to compute a spatial matrix and apply a temporal filter to whiten the data (Figure 6.3a).

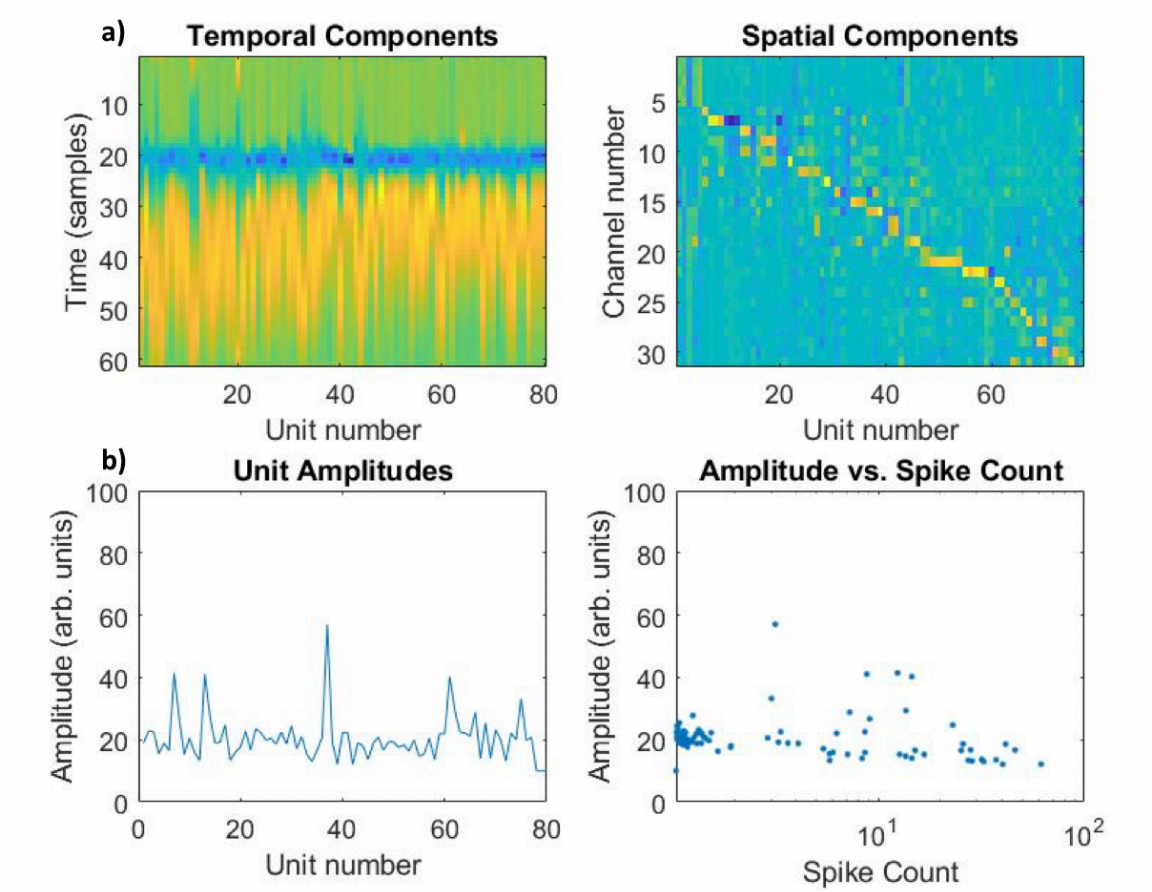

Figure 6.3: Temporal filtering and spatial whitening. a) Temporal filter to whiten data. Spatial matrix for whitening of 32 electrodes. b) Amplitude of each spike cluster unit versus spike count for each amplitude.

6.3.5 Spike recording and waveform quality

The local field potential (LFP) and the pattern of tonic spike bursts in our recording is consistent with patterns we would expect in the mouse cortex motor area and somatosensory areas (Figure 6.6) (Ruiz-Mejias et al., 2011).

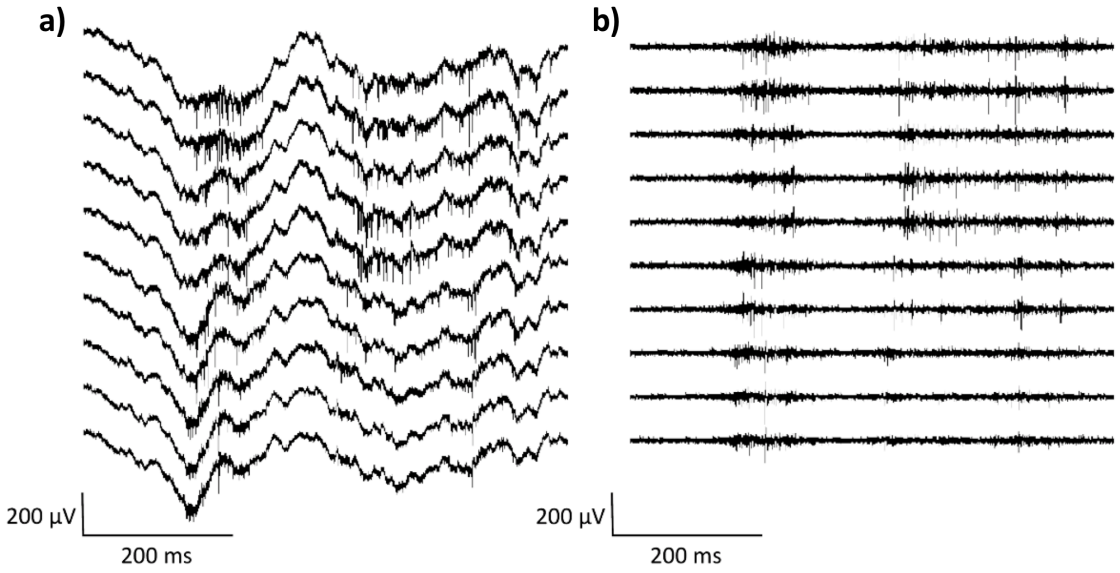

Figure 6.4: Spike recording from consecutive recording sites of neural probe. a) Broad-band (1 Hz-10 kHz) filter of LFP signal. Channels are ordered by their position on the probe (with top traces located at the probe tip and bottom traces located towards the probe base). b) Spike frequency (300 Hz - 10 kHz) filtered signal of the same recording.

6.3.6 Single unit isolation with dense electrode array neural probes

Dense electrode arrays on neural probes allow for reliable single neuron unit isolation. To sort out the spike waveforms to individual neuron units, we extracted different features of the spike's waveform such as the shape (e.g., height and width), phase, and amplitude using Spyking-Circus (Yger et al., 2018) (Figure 6.5). We then looked at the variance of these features using principal component analysis (PCA) to cluster waveforms into single neuron units. Since each neuron produces waveforms with distinct features, we

can separate spike waveform clusters into individual neuron units (Yger et al., 2018). Since each spike waveform is picked up on multiple nearby sites with different amplitudes, we can more reliably isolate the activity of individual neurons (Figure 6.7). Electrodes close together also provide more spatiotemporal resolution of the spike waveforms, which aid in spike detection and sorting procedures (Neto et al., 2016). Additionally, dense electrode arrays also allow for more reliable isolation of units by incorporating spike waveform indices from the surrounding sites, making it possible to resolve close clusters and isolate more neurons (Gray et al., 1995; Harrison & Charles, 2003). The multiple waveforms from each isolated unit detected across neighboring pads demonstrate the quality of the clustering in our recording and help us achieve more reliable single unit isolation (Figure 6.5 and 6.6).

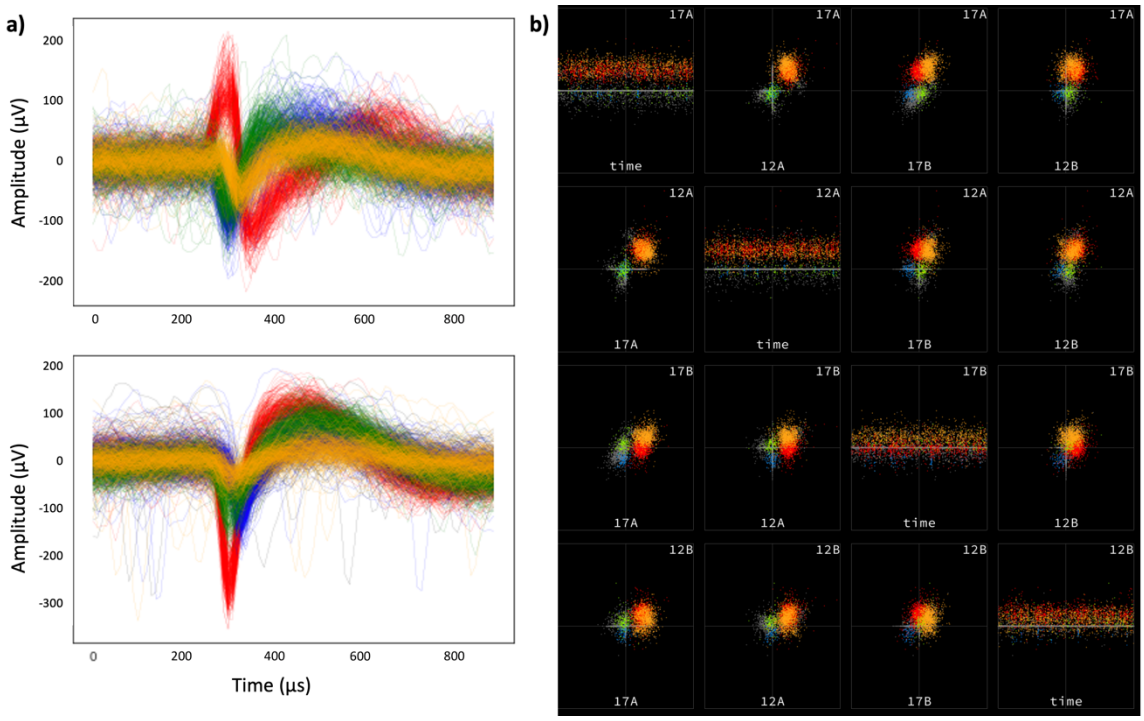

Figure 6.5: Multiple spike waveforms measured on one electrode pad. a) Overlay of spike waveforms from different cluster units on electrodes. b) Principal component analysis (PCA) features of selected waveforms shown in a). Individual graphs show relevant channels (shown by numbers). A, B, and C refer to the first, second, and third (respectively) dimensions of the principal components.

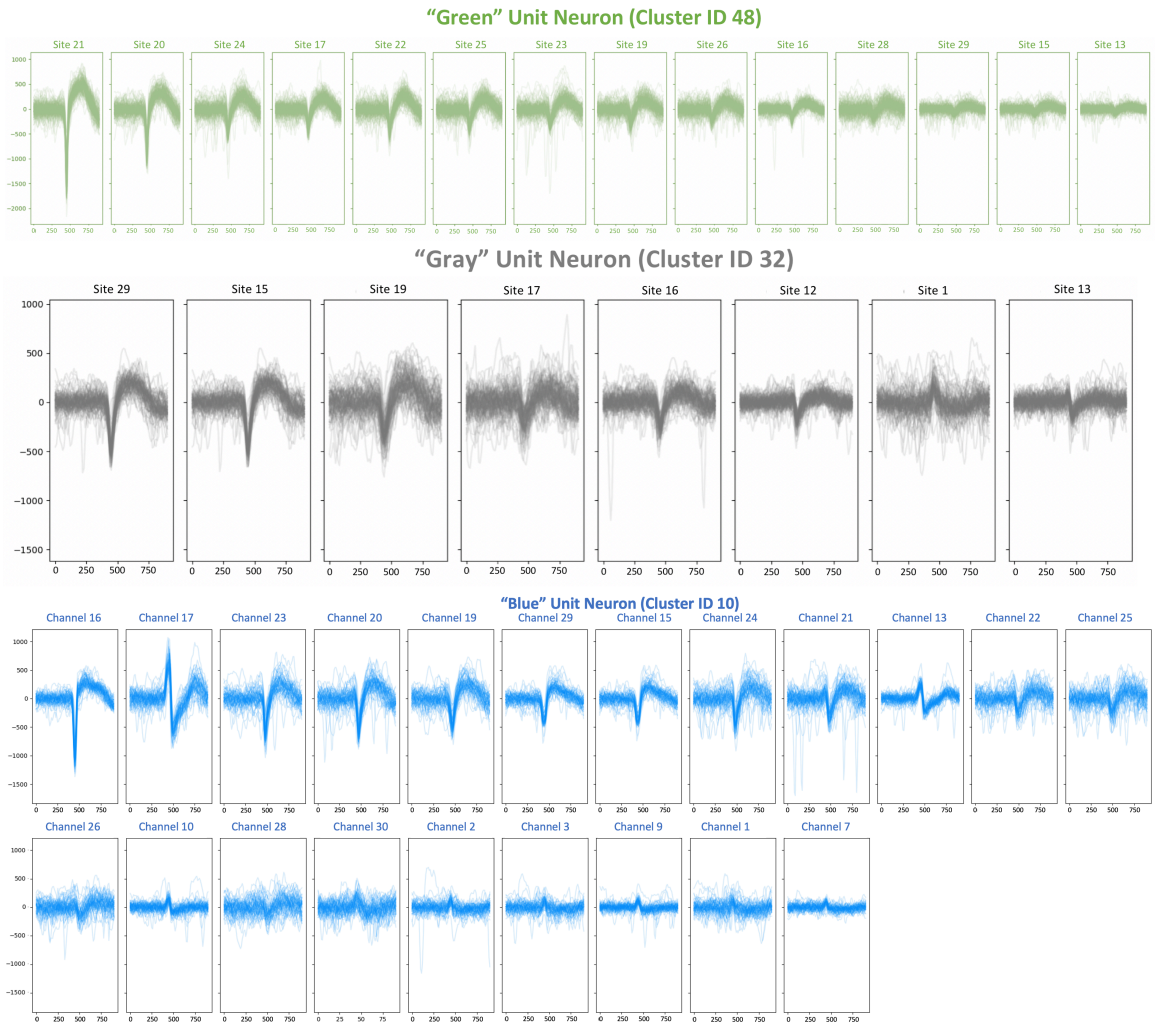

Figure 6.6: Example waveforms clusters units recorded across each channel. Waveforms from individual neurons detected across multiple electrode sites. Spike sorting was performed using Spyking-Circus and results were visualized and validated on phy (x-axis is time in μs).

Using our probes, we detected 5 to 18 neuron units per electrode (Figure 6.8), which is higher than the number of neurons isolated experimentally by other ephys probes (Table 5). The average number of neurons we detected was 9.7 ± 3.1 neurons per electrode and a median of 9 neurons detected per electrode. One reason we might detect more neuron units than other epys probe is because our dense electrode arrays allow us to more reliably isolate close waveform clusters into individual neuron units. This high number of neuron units

detected per electrode indicates good coverage of surrounding brain activity and is consistent with the maximum number of neurons using empirical estimates, which predicts a maximum of 10-15 neuron per electrode in the rodent cortex (Neto et al., 2016).

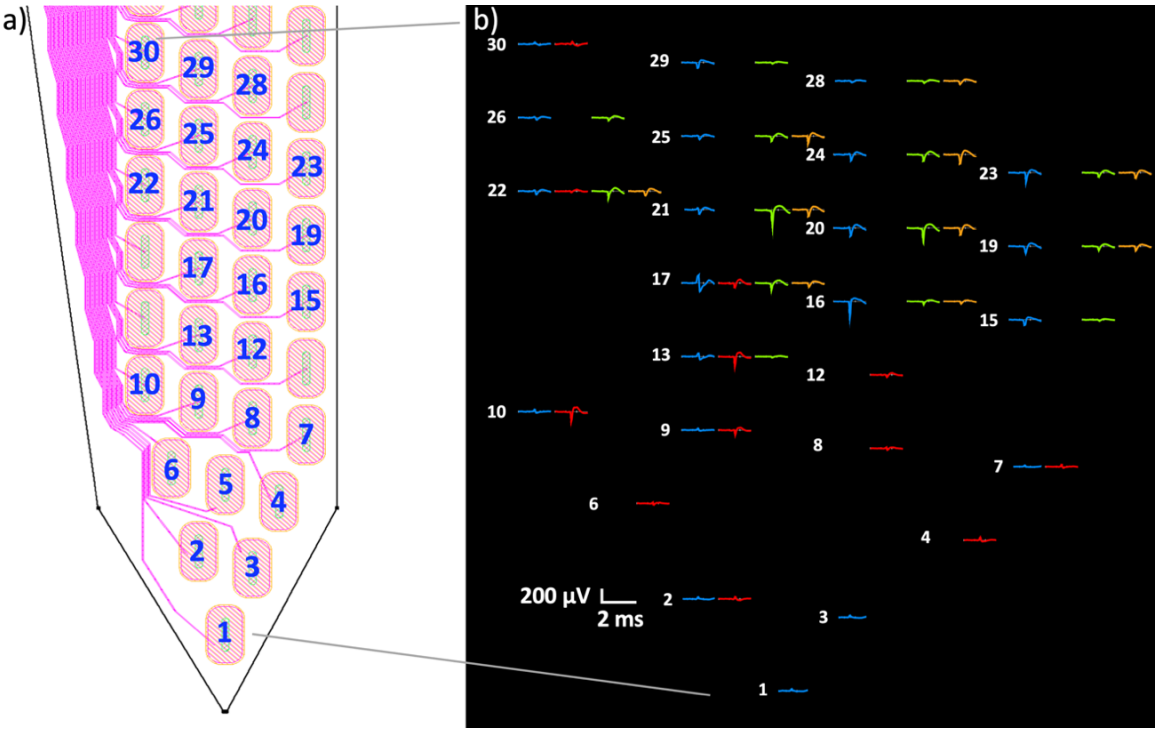

Figure 6.7: Single unit isolation. Analysis performed with Spyking-Circus sorting. a) Annotated recording electrodes of neural probe pads. b) Representative mean waveforms for putative single neurons on each channel. Each waveform cluster is represented with a different color.

a)

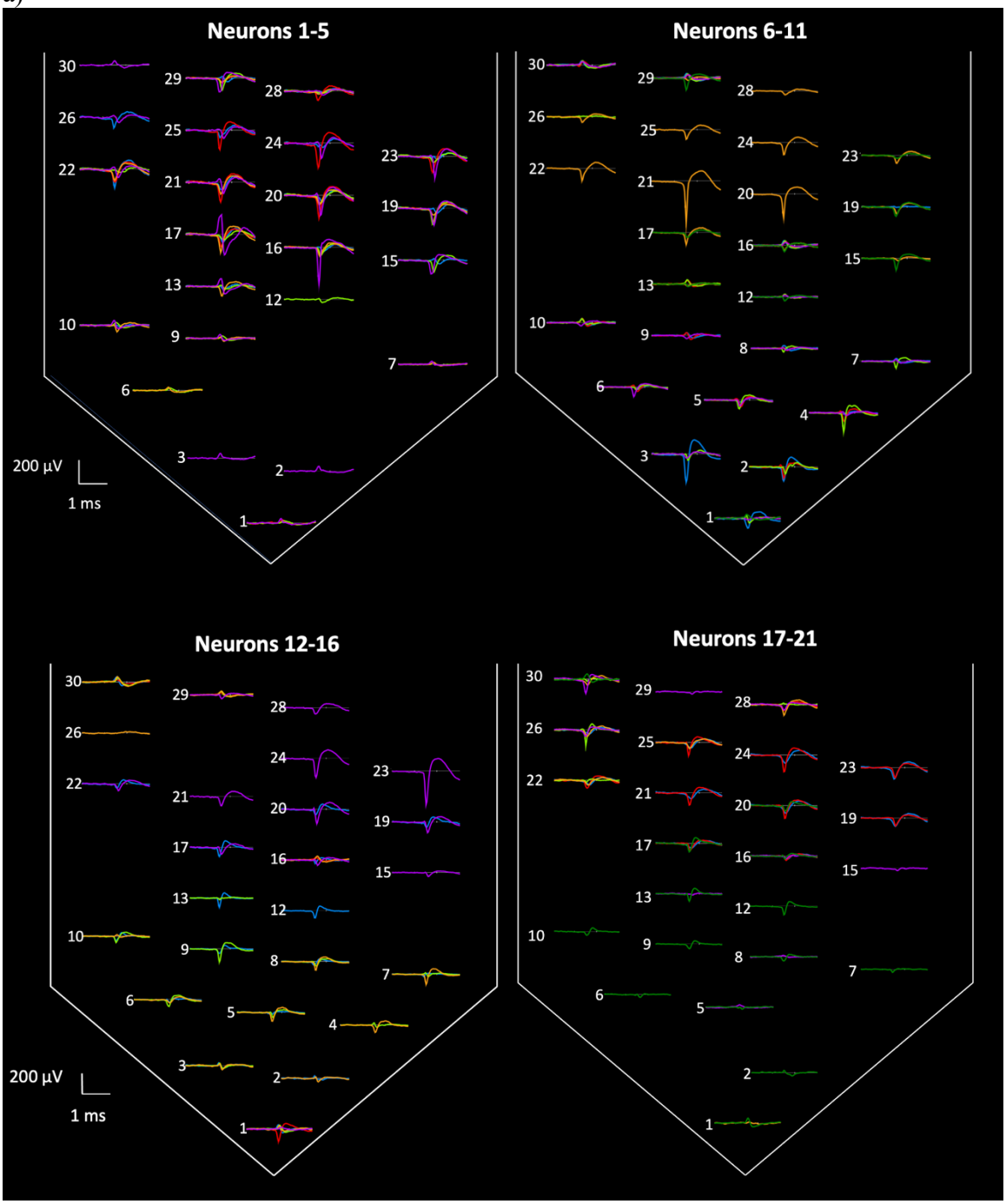
Neurons 1-5
Neurons 6-11
Neurons 12-16
Neurons 17-21
200 µV
1 ms
200 µV
1 ms

b)

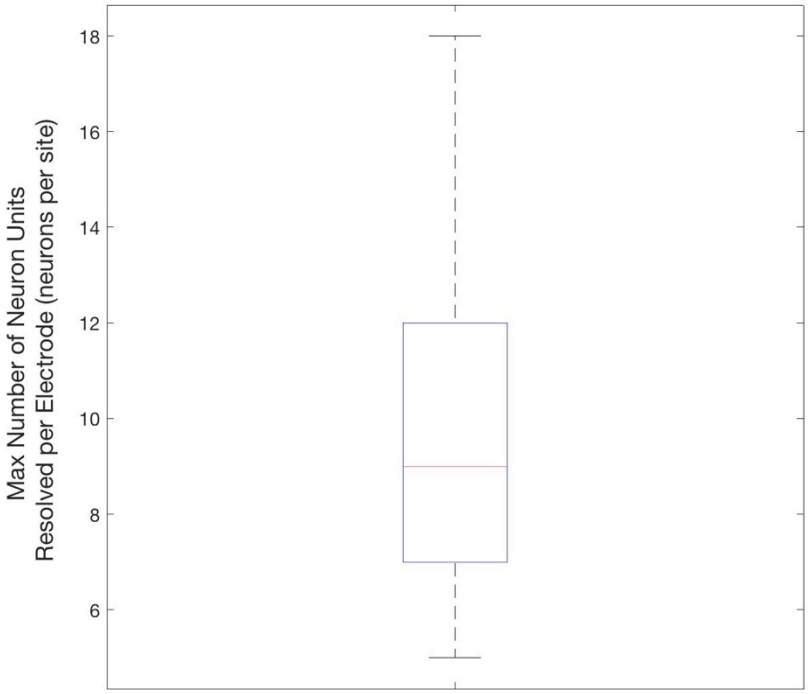

c)

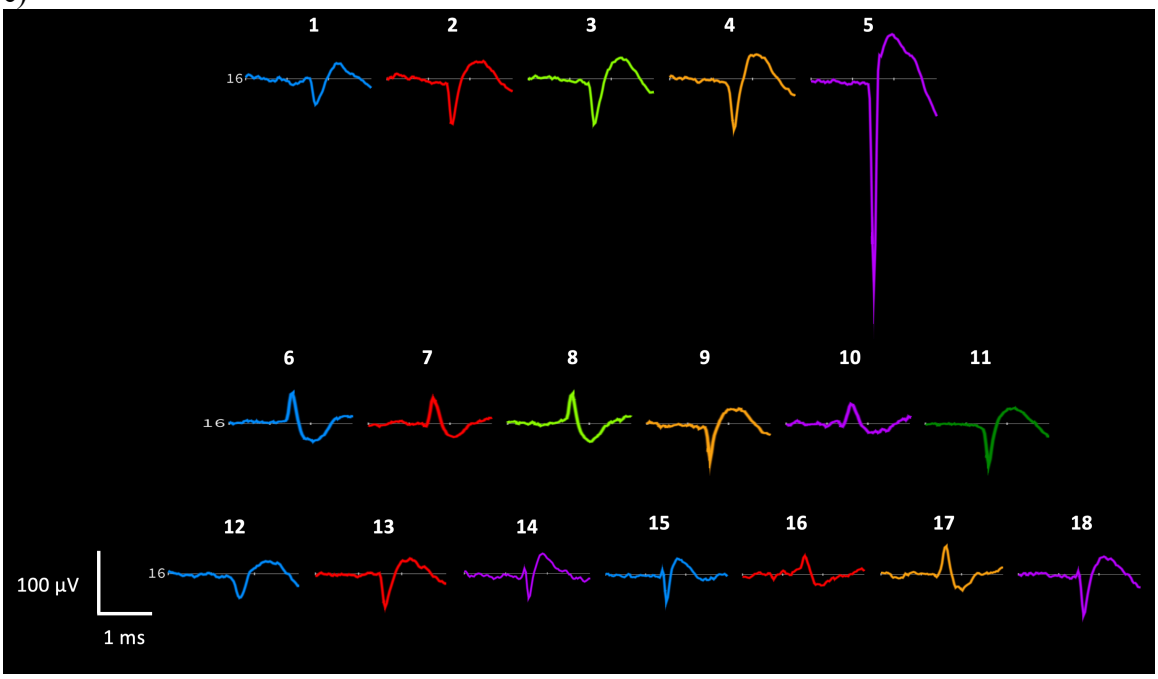

Figure 6.8: Neuron units isolated per electrode. a) Plot of mean waveform for all isolated neuron units plotted by electrode position on the neural probe. b) Box and whisker plot of neuron units isolated on each electrode. With our probe, we detected a maximum of 5-18 putative neurons isolated on each electrode pad. c) Mean waveform of each isolated neuron on one electrode site. On this pad, we detect 18 distinct neuron units.

Table 5: Comparison of maximum number of neuron units isolated per electrodes with other state of the art ephys probes.

	Maximum neurons per electrode	Average neurons per electrode	Electrode density
Neurolynx polytrode (54-channel)[1]	6 (24 per virtual tetrode)	NA	~64 electrodes/mm
Neuropixels[2]	11	6.9±5.1	~102 active electrodes/mm
Caltech probe	18	9.7±3.1	~171 electrodes/mm

[1]Values for Neurolyx probe are derived from (Blanche et al., 2005). [2]Neuropixel values were taken from (Jun et al., 2017).

6.3.7 Detection limits of electrodes

The maximum detection range was derived following methods listed in *Du et al 2011* (Du et al., 2011). Briefly the following steps were performed to determine the maximum detection range: spikes were sorted (using Spyking-Circus or Kilosort) and then the mean spike waveform of each neuron unit on the electrodes and the peak-to-peak amplitude for each spike waveform was calculated. Then, the electrode with the highest amplitude was set as the reference position since it should be the closest to the active neuron. The furthest electrode from the reference with the unit amplitude of at least 50 μV and distinct waveform was chosen as the furthest electrode. Then the center-to-center distance between the furthest electrode and reference electrode was used as the maximum detection range.

As shown in Figure 6.9, our detection range is similar to the maximum detection range reported in literature, with spikes recorded up to 168 μm from the electrode (as compared to literature with spikes recorded up to 160 μm) (Du et al., 2011). The average maximum detection range is 76.1 ± 40.7 μm and the median maximum detection range is 60 μm. This average maximum detection range is within the values predicted in literature of

between 100 to 150 µm (Anastassiou et al., 2015; Neto et al., 2016). The few neurons that can be detected as far away as 150 to 168 µm away are likely positioned along the electrodes. Since the axis of the neuron processes lie along the electrodes, the neurons can be detected further away due to neural backpropagation; thus, increasing the maximum detection range of these neuron units well beyond the median and average.

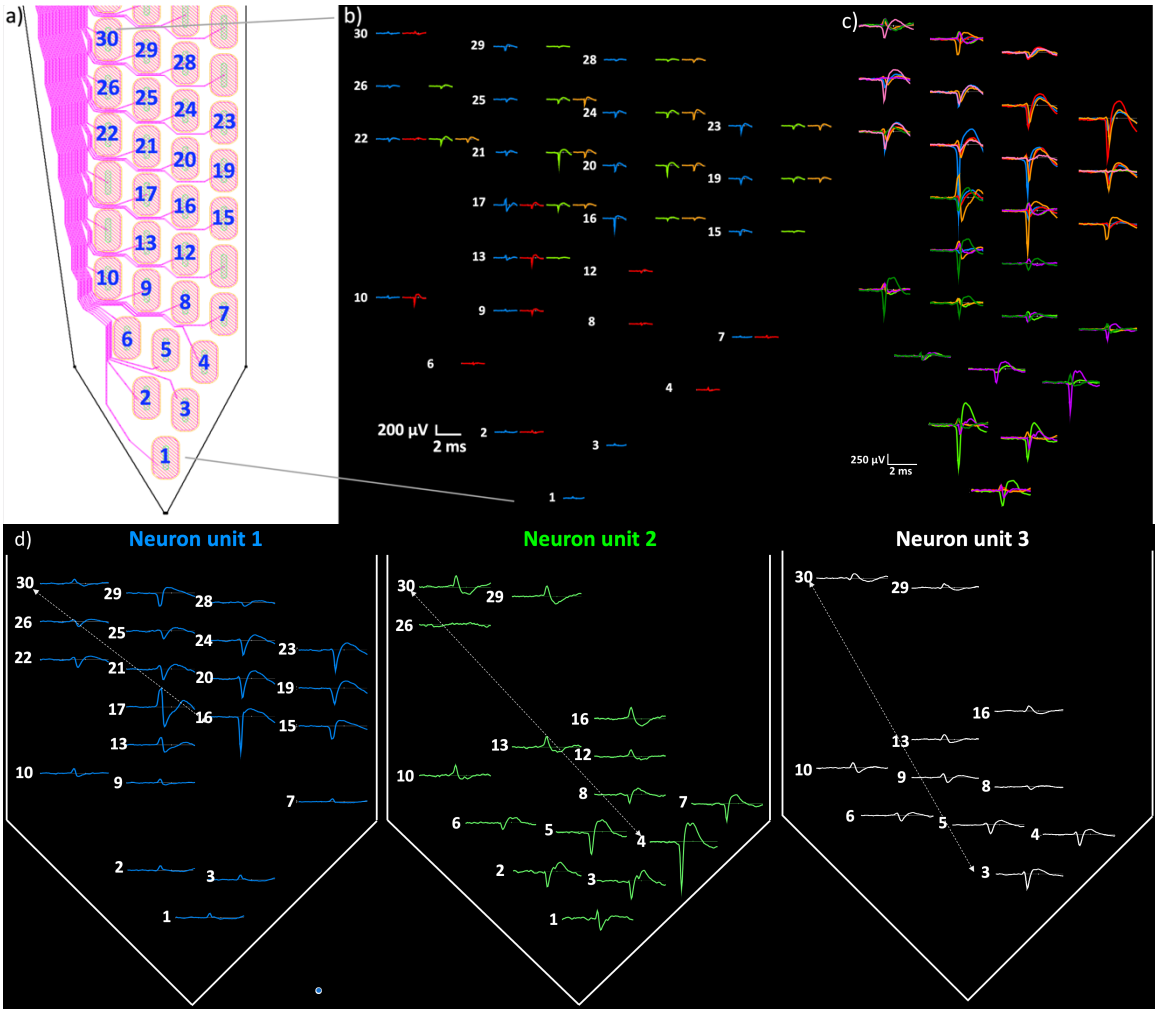

e)

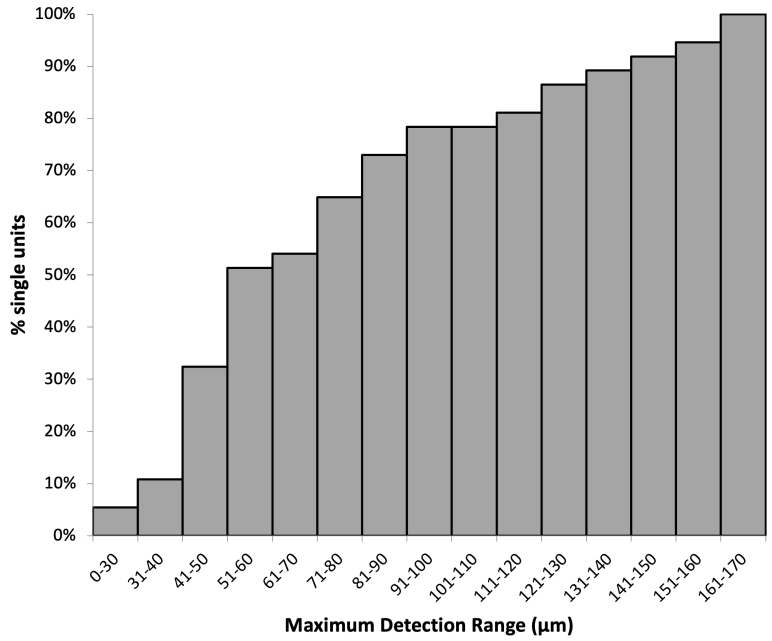

f)

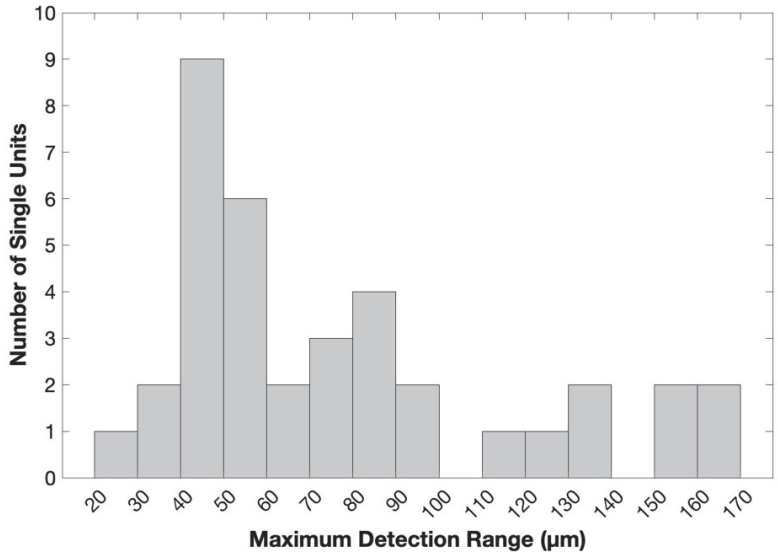

Figure 6.9: Single unit isolation and limits of detection. Analysis performed with Spyking-Circus sorting. a) Annotated electrodes on nanoprobe pads. b) Representative mean waveforms for putative single neurons on each channel. Each waveform cluster is represented a different color. c) Overlay of representative mean waveforms for seven putative single unit neurons. d) Three neuron units with mean waveforms plotted on electrode. Each waveform cluster is colored by the neuron unit it belongs to. Arrows point from the reference electrode (highest amplitude waveform) closest to neuron to furthest detecting electrode. e) Maximum detection range of neural probe plotted by their cumulative distribution. f) Histogram of maximum detection range plotted by number of single units detected at each range.

6.4 Extracellular recording combined with two-photon imaging

When combined with two-photon imaging, we similarly obtain high quality recording with single neuron activity. Through this method, we can map the position of individual neuron units along the probe while visualizing surrounding neurons with two-photon microscopy (Figure 6.10).

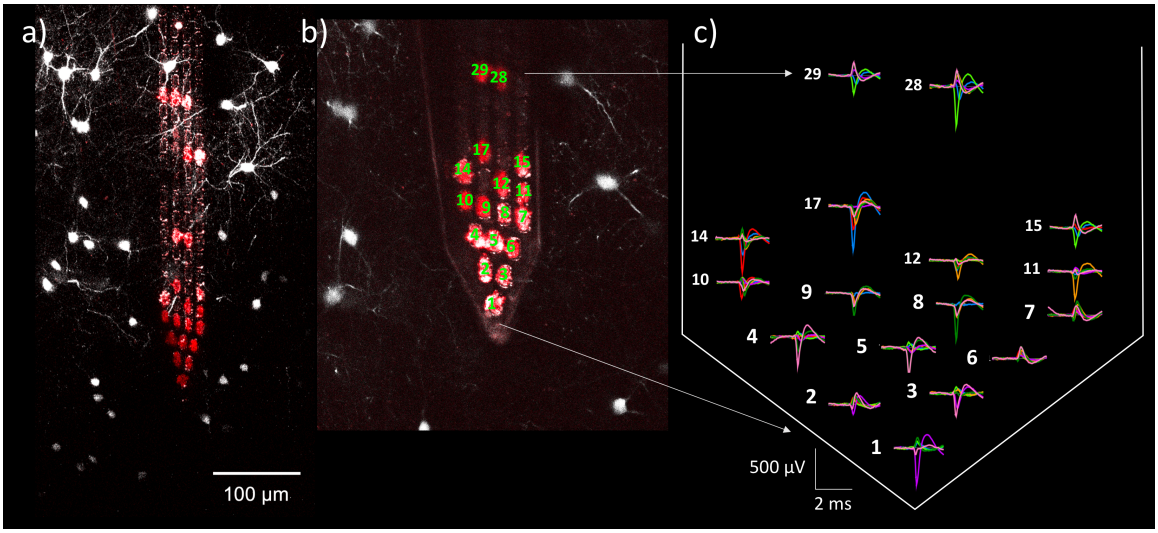

Figure 6.10: Single unit isolation mapped to probe and surrounding labeled neurons. a) Two-photon imaging of GFP labeled interneurons (*white*) in the cortex with the probe (pads shown as red). b) Annotated neural probe with electrode pad sites numbered by their position. c) Spike waveforms labeled in accordance with the electrode position.

6.5 Conclusion

In conclusion, we demonstrate high quality LFP and spike recording. Analysis of spiking units across neighboring electrodes demonstrates high-quality single neuron unit isolation with the neural probes. Our high-density neural probes also enable reliable detection and isolation of as many single neurons units (5-18 units) as other probes. We also demonstrated our limits of detection are comparable to or greater than other state-of-the-art electrodes. When combined with our platform for two-photon microscopy we are

simultaneously able to visualize labeled neurons, record their electrophysiological activity, and stimulate neuron activity with optogenetically labeled neurons.

Chapter 7

QUANTIFICATION OF PROBE INVASIVENESS USING VASCULATURE AND NEURON STAINING *IN VIVO*

7.1 Introduction

To accurately recapitulate the brain's activity, it is important to maintain the integrity of the brain and minimize damage to surrounding brain tissue during long-term ephys recordings. It is also important to consider probe invasiveness because probe implantation may result in bleeding that induce inflammation reactions, which over long time periods will degrade the quality of spike recording (Szarowski et al., 2003). In this chapter, we look at the invasiveness of the probe *in vivo* using mice whose vasculature system was stained using fluorescent dextran. To quantify the probe invasiveness, we examined the displacement of neurons and vasculature during and after probe insertion and removal. While probe damage is well characterized *in vitro* on fixed brain slices, we describe for the first-time imaging of probe invasiveness as it is inserted using vasculature stain *in vivo* under two-photon imaging. Fixation introduces artifacts such as tissue shrinkage so *in vivo* methods are more accurate when accessing tissue displacement and damage caused by implantation of the neural probe. In this chapter, we quantify the vasculature displacement of our ultranarrow neural probe using concurrent imaging of the probe *in vivo*. Using these methods, we demonstrate our neural probe, with its small cross section and passivated surface, creates minimal tissue displacement upon probe removal *in vivo*.

7.2 Invasiveness of probe insertion

During probe implantation, the shear motion between the interface of the neural probe and tissue changes the position of recorded neurons relative to the recording electrodes. The cause of the tissue deformation from the probe can be attributed to two physical parameters, the Young's modulus and bending stiffness of the probe. Compared to brain tissue, with an average modulus of 1.895 kPa, a silicon probe has a modulus of 179 GPa; this 10^5 factor difference leads to deformation of the soft tissue around the probe during implantation (McGlynn et al., 2021). Additionally, the neural tissue is extremely soft (a brain slice with a thickness of 20-100 μm has a bending stiffness of 10^{-4} to 10^{-1} nN m per unit width) (Hong & Lieber, 2019) and a silicon probe 15 μm thick is stiff (with a bending stiffness of 10^5 nN m) (Lee et al., 2005). This large difference in bending thickness leads to shearing between the brain and neural probe during implantation (Hong & Lieber, 2019). Reducing the thickness of the silicon layer helps increase the flexibility of the probe and reduce damage (Hong & Lieber, 2019).

Additionally, over time the neural probe implant generates chronic immune responses leading to the death or damage of nearby neurons and proliferation of astrocyte and microglia around the probe (Polikov et al., 2005). Plasma proteins and porphyrins released during bleeding can also be adsorbed onto the electrode (Groothuis et al., 1998; Ye et al., 2006). This bleeding can cause a substantial decrease in the offset potential of the electrodes and intense acidosis can degrade neuronal spike activity recordings (Johnson et al., 2007). For these reasons, it is vital to ascertain the damage caused by our probe and to do this we imaged the probe insertion during acute recordings *in vivo*.

7.2.1 Traditional methods of accessing probe damage and limitations

Traditional methods of quantifying probe damage rely on postmortem analysis with fixed brain slices. Some popular stains for tracing probe damage include propidium iodide stains, which intercalate with DNA but are membrane impermeable, and thus only stain cells with damaged cell membranes (Belloc et al., 1994). To visualize the track left by the probe, Dil (lipophilic fluorescent dye) is applied to the shank neural probe and stained cellular membranes the shank comes into contact with, thus marking the track left by the probe (Sariev et al., 2017). However, such stains are examined in fixed brain slices which require histological processing of brain tissue that introduces confounding tissue shrinkage (Tran et al., 2015). This tissue shrinkage makes it difficult to determine the actual displacement and damage caused by probe insertion. Additionally, the serial sectioning of the tissue used to produce brain slices is often imprecise and time-consuming (Jensen & Berg, 2016). For example, tracing the track of the probe can require several sections if the cutting angle used to slice the brain is not parallel to the neural probe track and slicing itself may distort the brain (Jensen & Berg, 2016). Another limitation is that fixed brain slices do not capture dynamic changes brought on by implantation like inflammation or bleeding from tissue damage.

7.2.2 Why measure tissue damage in vivo

We wanted to examine the displacement of the tissue *in vivo* under two photon microscopy to better observe the damage and perturbation of neural tissue caused by the probe compared to fixed post-mortem tissue, which may have tissue shrinkage or other artifacts altering the position of cells (Balaban & Hampshire, 2001; Tran et al., 2015). By looking at the insertion of the probe *in vivo*, we can observe the perturbation of the probe to

physiological, functioning, intact neurons and thus more accurately determine the location of the surrounding neurons relative to the electrodes (Balaban & Hampshire, 2001; Yoder, 2002). Additionally, *in vivo* imaging allows us to observe blood flow and avoid damaging blood vessels during probe insertion.

7.2.2.1 Intravascular staining for examining tissue damage *in vivo*

Vasculature staining was chosen as a benchmark for tissue damage because any damage in the blood vessels of the pial layer or hemorrhaging in layers being imaged or above will suppress fluorescent signals and severely degrade imaging quality (Kozai et al., 2010; Shih et al., 2012). Thus, vasculature staining is a sensitive benchmark of probe damage since puncturing vessels during insertion will lead to noticeable dark areas from bleeding during imaging. Previous literature of neurovasculature damage using *in vivo* two-photon imaging before probe insertion and after probe removal showed a vasculature deviation of more than 49 μm when the commercially available microelectrode (Neuronexus A1x16-3mm-100-177) probe was inserted near major surface vessels (Kozai et al., 2010). In this chapter, we investigated whether our revised probe shank profile would lead to less disruption and displacement of blood vessels after insertion.

To label brain vasculature, Texas Red Dextran (MW 70,000, Neutral, Invitrogen D1830) was injected via the retro-orbital sinus following methods listed in (Yoder, 2002). First, the mouse was anesthetized with urethane. Next, the Texas Red dextran was diluted with saline solution so that the total concentration of dye solution is 30 μM in the blood volume per mouse. The dextran solution was then loaded into a 1 mL syringe with a 30-gauge needle, which was inserted into the medial canthus at a 30-45° angle through the

conjunctival membrane. The dextran was then slowly injected into the retro-orbital sinus of the mouse (Yardeni et al., 2011; Yoder, 2002).

Using intravenous injection, we observed bright vasculature staining in the cortex throughout the coverslip viewing window on top of the mouse's brain (Figure 7.1). Vasculature was well stained even 320 μm below the surface of the pia matter with sufficient lateral resolution to image individual blood vessels and capillaries at depth (Figure 7.1 b and c). Capillaries appear dimmer at depth due to light scatter by the brain tissue. After demonstrating good cerebral vasculature staining and imaging at depth, we next looked at the displacement in vasculature and neurons caused by probe implantation in mice whose interneurons are labeled with GFP, and vasculature systems are stained with Texas Red dextran (70,000 MW).

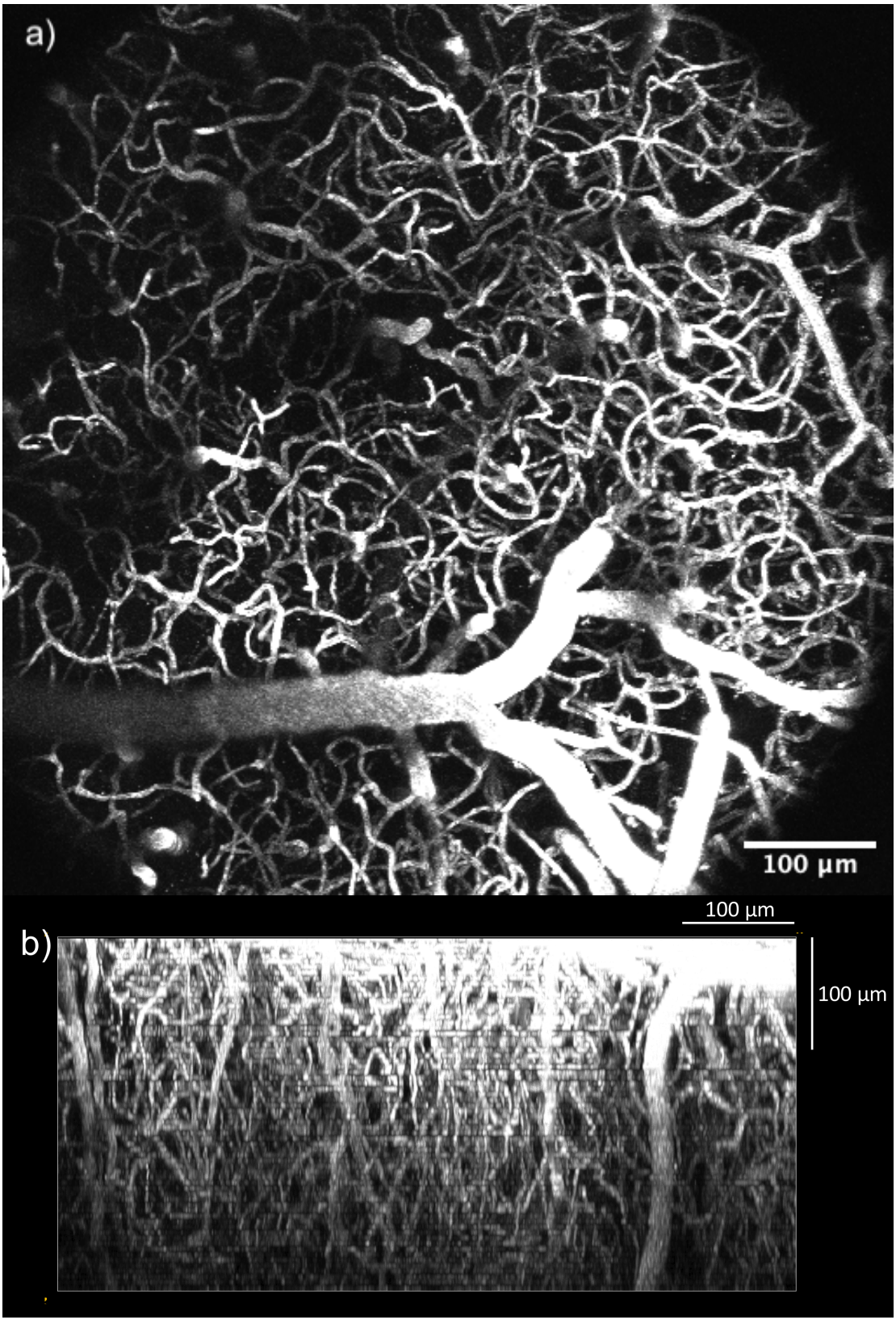
a)
100 µm
b)
100 µm
100 µm

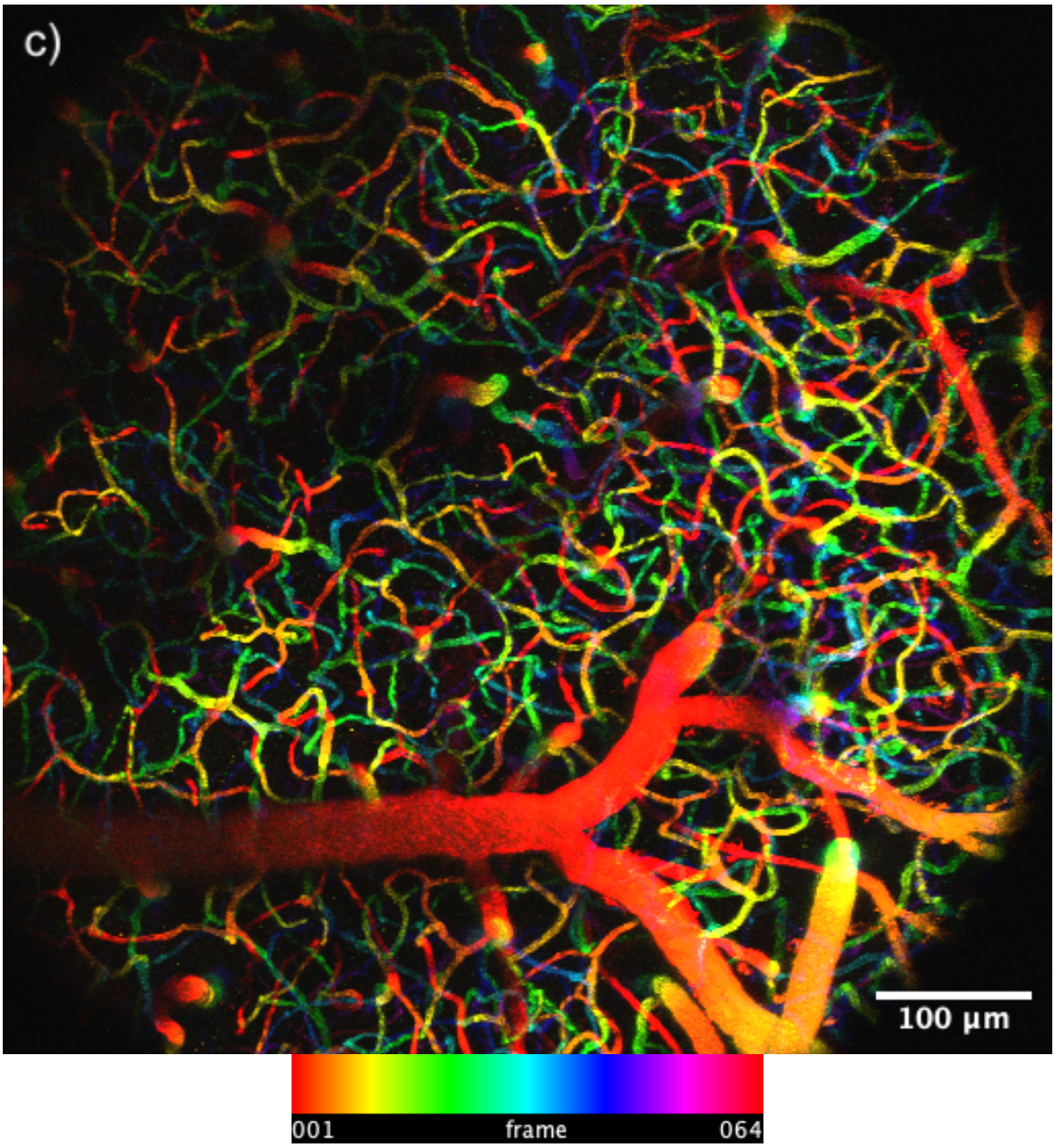

Figure 7.1: Staining of cerebral vasculature with Texas Red Dextran (70,000 MW, neutral charge) *in vivo* with two-photon imaging. a) Maximum projection of top surface of the brain to 320 µm below surface. b) Cross-sectional view of vasculature stain across depth. Frames are 5 µm apart in the z-direction. c) Maximum projection of vasculature stain color coded by depth in z-stack.

7.3 Evidence of minimal invasiveness of probe insertion

7.3.1 Vasculature stain during probe implantation and probe removal

To examine the damage and displacement caused by the probe, we imaged the vasculature of the brain, which was stained using Texas-Red dextran, during probe implantation and after probe removal. To minimize damage, the probe was inserted slowly into the brain at approximately 10 μm per second. Overlays of vasculature staining during probe implantation and after probe removal demonstrate good alignment with vasculature positions before and after (Figure 7.2). We also demonstrate minimal displacement of the vasculature around the probe with a maximum lateral displacement of approximately 10-20 μm (Figure 7.2).

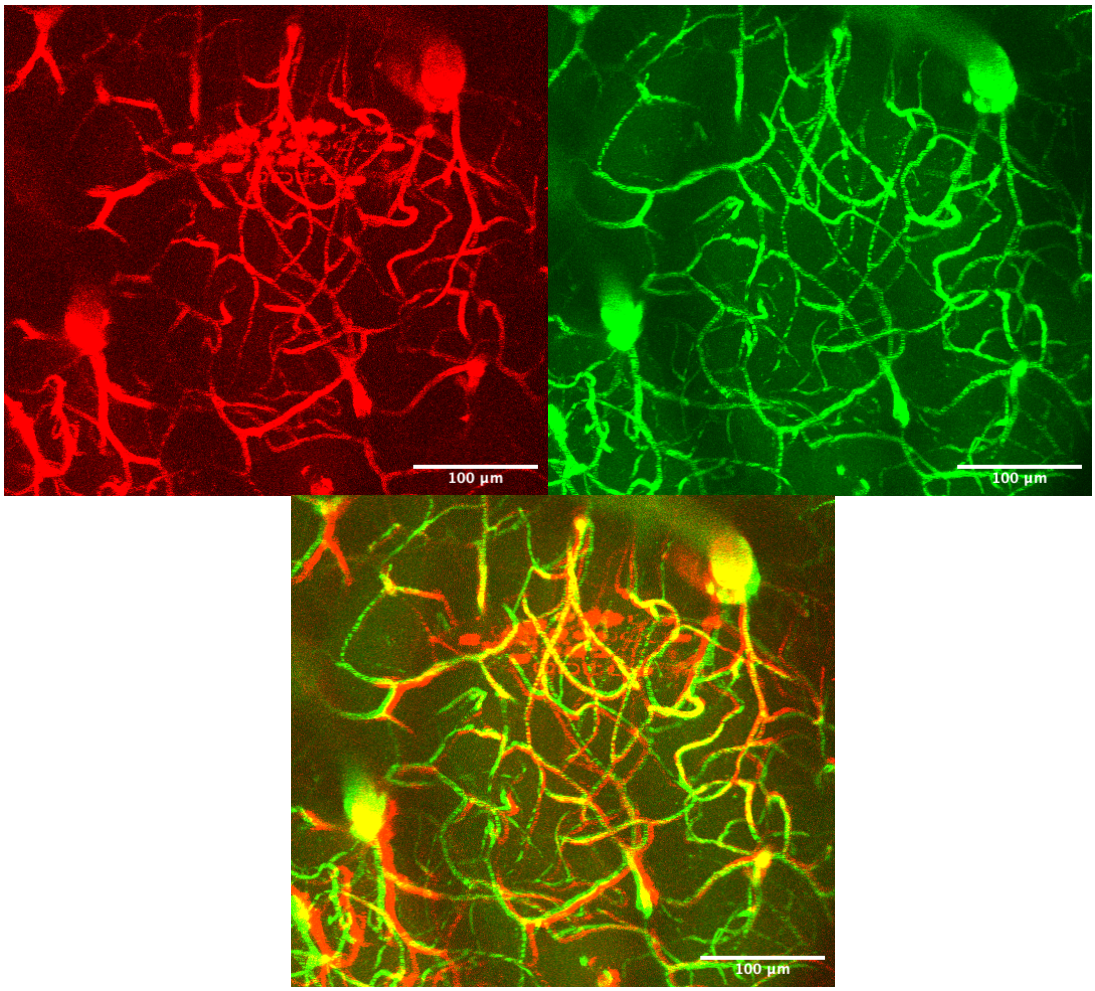

Figure 7.2: Vasculature during and after probe insertion and removal. Max projection of vasculature around probe 105 µm above and 50 µm below probe. The first slice of z-stack begins at 125 µm and last slice ends at 280 µm below pial surface. a) Vasculature staining around probe during implantation. Probe and vasculature shown in red. b) Vasculature after probe is removed (*green*). c) Composite overlay of vasculature projection during probe implantation and after probe removal.

To examine the probe damage at depth, we also looked at cross-section views of the vasculature. Cross-section imaging of the vasculature during probe implantation and after probe removal reveal the vasculature remains mostly intact around the probe insertion area (Figure 7.3). The area below the implanted probe appears dark due to the silicon probe blocking the excitation light from reaching the area directly below it (Figure 7.3a).

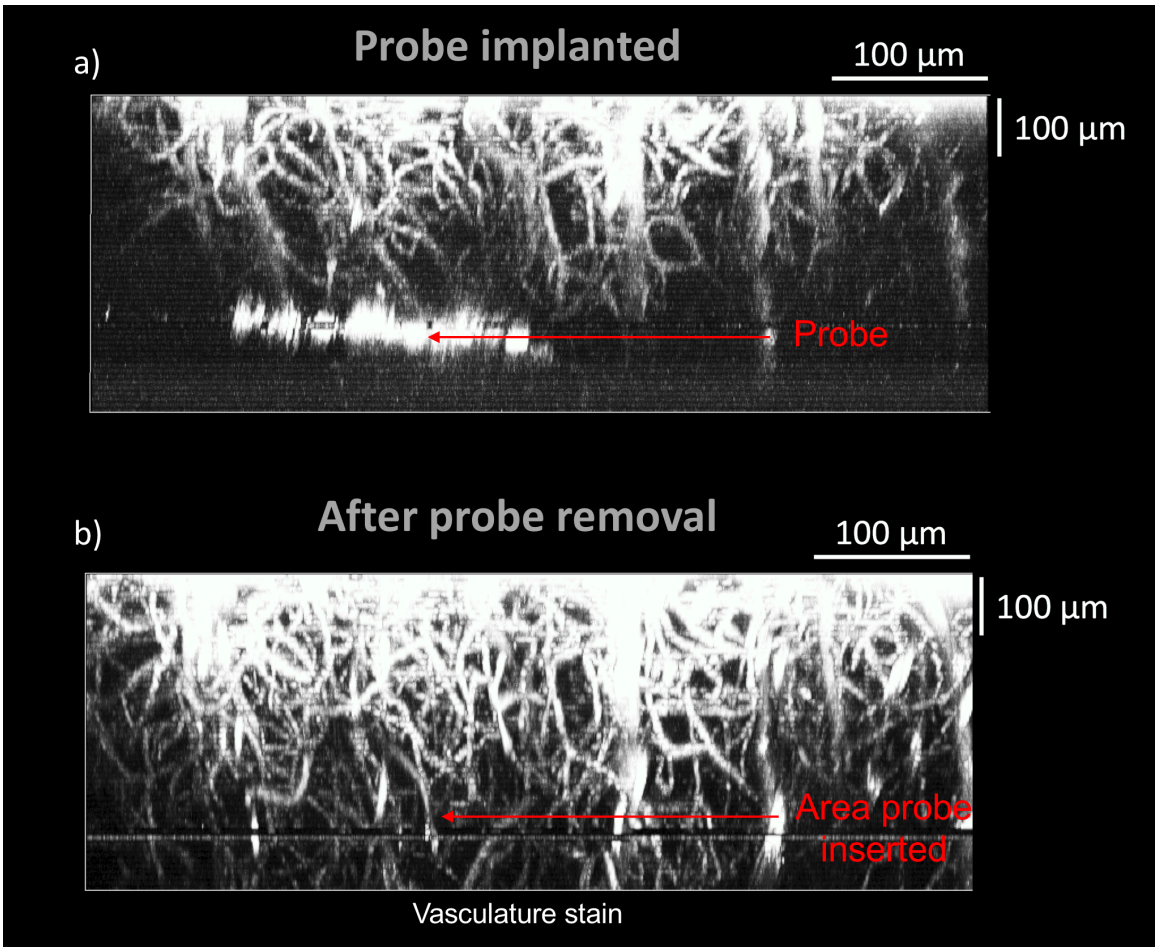

Figure 7.3: Side view of vasculature during and after probe implantation. a) Cross section of vasculature during probe implantation. Red arrow indicates position of the probe. Reflection of laser across gold electroplated pads on the probe leads to the horizontal white object. b) Cross section of vasculature after probe removal. The red arrow indicates the area where the probe was implanted.

7.3.2 Time-series during probe removal

The probe was imaged as it was inserted into the brain tissue *in vivo* to assess tissue deformation and dynamic changes in the vasculature during removal. Time-series with one frame taken every 0.74 seconds from each other reveal the position of most capillaries around the probe do not appear to drastically change as the probe is removed (probe moved 137 µm in this time series) into the brain (Figure 7.4). Using this method, we do not see noticeable tearing of surrounding capillaries in the wake of the probe as it is removed (Figure 7.4). We

also do not notice large areas of vasculature damage in capillaries at depth after probe removal (Figure 7.3). In contrast previous literature, with 2P imaging of cortical vasculature *in vivo* before probe implantation and after probe removal, shows more noticeable neurovascular damage with the formation of large dark regions in areas the probe was removed from (Kozai et al., 2010). These dark regions are probably formed because the blood from the damaged vasculature suppresses fluorescent signal (Kozai et al., 2010). Our lack of noticeable vasculature damage suggests that our probe and insertion strategy create less neurovascular damage than other commercially available probes and methods.

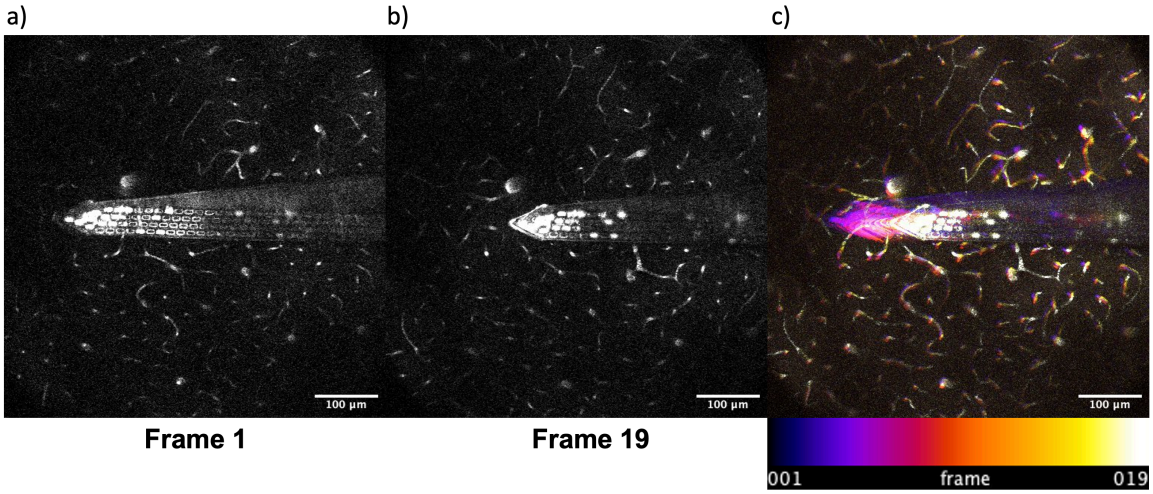

Figure 7.4: Time series of probe removal in vasculature. a) First frame in the time series (time 0). b) Last frame (after approximately 137 µm removal). c) Timeseries of probe removal with frames color coded by color map. Frames were taken at 0.74 frames per second.

7.3.3 Neuron displacement

To examine the displacement of neuron cell bodies caused by the probe, we used GIN mice, a transgenic mouse line whose GABAergic interneurons express GFP under the control of the *Gad1* gene promoter (Jackson Laboratory, strain code: 003718) (Oliva et al., 2000). Neuron cell bodies reveal a maximum displacement of around 15 µm between probe implantation and after probe removal (Figure 7.5). To better quantify the damage across the

vasculature network, especially near the probe insertion area, we mapped and modeled the vasculature based on our vasculature stain images.

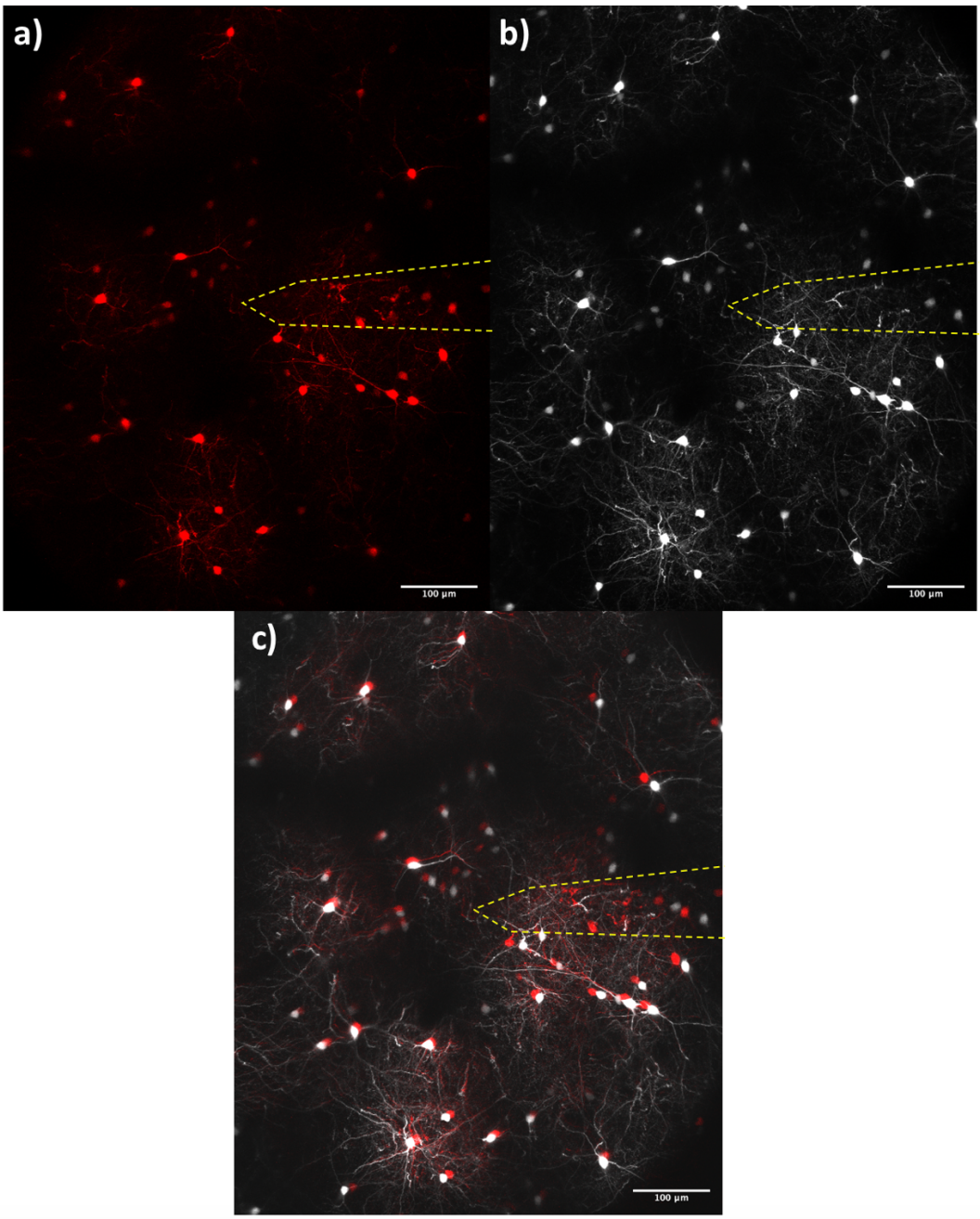

Figure 7.5: Neuron cell body location before and after probe insertion (*overlay*). a) Position of neurons during probe implantation (*red*). b) Neurons after probe removal (*white*). c) Overlay of neuron positions during probe implantation and after probe removal. Outline of probe shown in dashed yellow lines.

7.4 Vasculature modeling and damage quantification

To model and accurately quantify vasculature damage during probe implantation and after probe removal, we used the software 3D Slicer and the Vascular Modelling Toolkit (VMTK) extension for segmentation, modeling, and 3D reconstruction (*3D Slicer Imaging Computing Platform*, 2022; Fedorov et al., 2012). First, we specified the dimensions of the z-stack images using the volume module. We then used the vesselness filtering module from the VMTK plugin for vessel segmentation of the capillaries and blood vessels in the z-stack. Minimum and maximum vessel diameters were adjusted in voxels to accurately filter blood vessels and capillaries as shown by the red highlights (Figure 7.6).

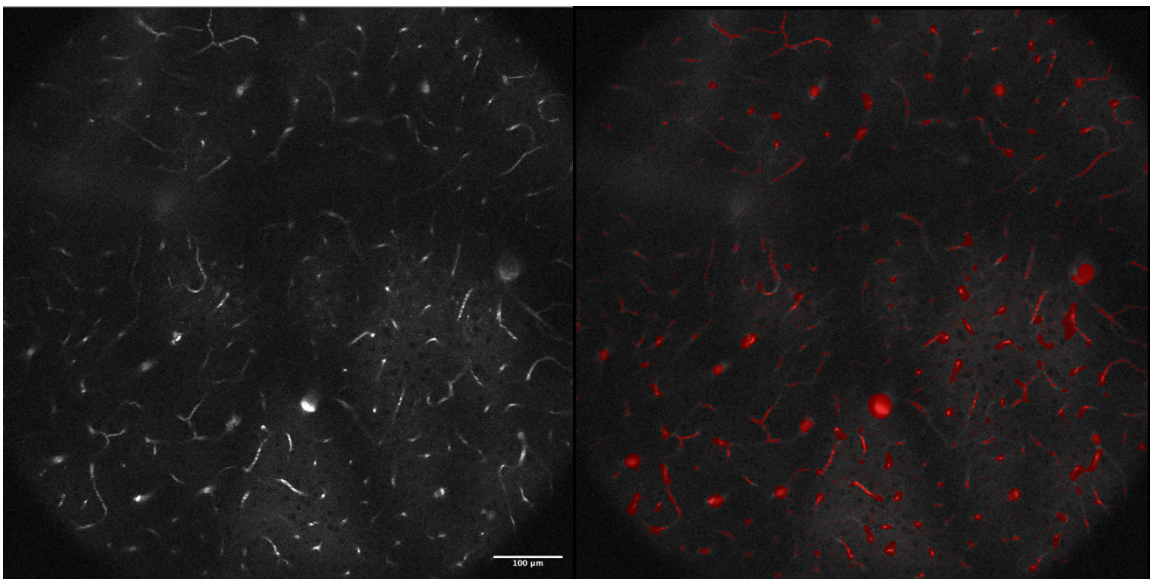

Figure 7.6: Vesselness filtering for segmenting vasculature for 3D modeling. Slice in z-stack of vasculature staining (*white*) taken at 130 µm below pial surface (*left image*). Areas recognized as vessels by the filter are shown in red (*right image*). Vesselness was filtered on each slice of the z-stack.

Next, the 3D slicer was used to render a 3D model of the segmented areas (Figure 7.7). Artifacts caused by the electroplated pads reflecting the infrared excitation light were removed using the segment editor. Examples of the vasculature model derived from a wild-

type mouse injected with Texas Red dextran are shown in Figure 7.7. We applied the same VMTK and 3D slicer pipeline to reconstruct the vasculature during probe implantation and after probe removal (Figure 7.8). Overlays of the two models show that most blood vessels remain intact after probe removal and the position does not appear to vary drastically (Figure 7.8).

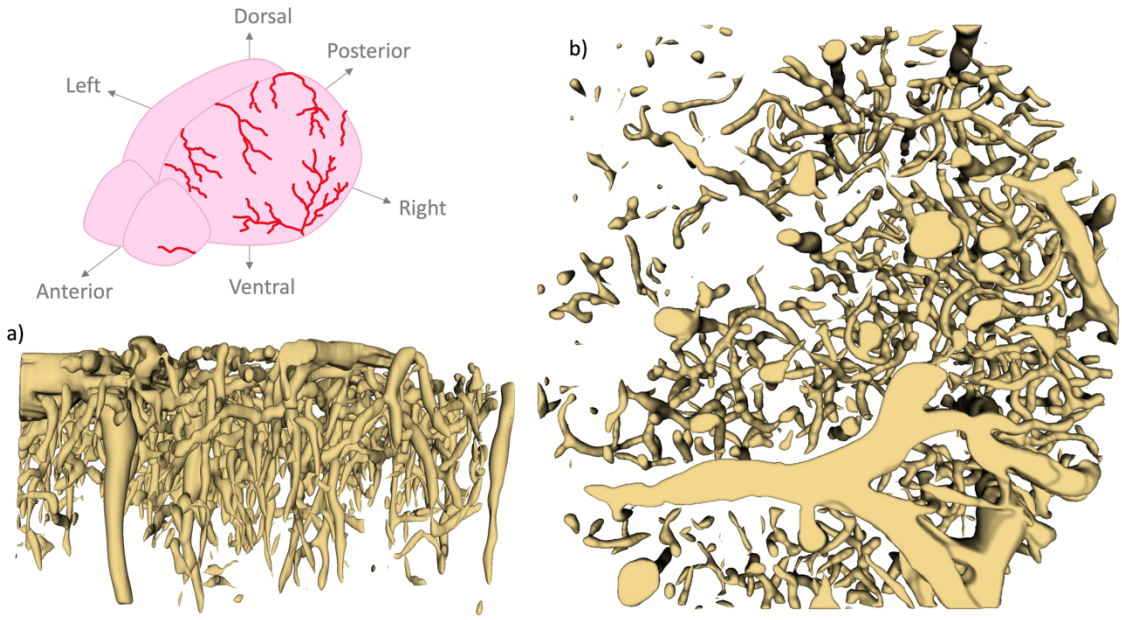

Figure 7.7: Model of vasculature in wild-type mouse. Model is derived from a C57BL/6 mouse brain with brain vasculature stained with Texas-red dextran. Vessels were recognized using vesselness filtering and 3D rendering performed in 3D slicer to generate the vasculature model. a) Side view. b) Top view from dorsal (top) to ventral (bottom).

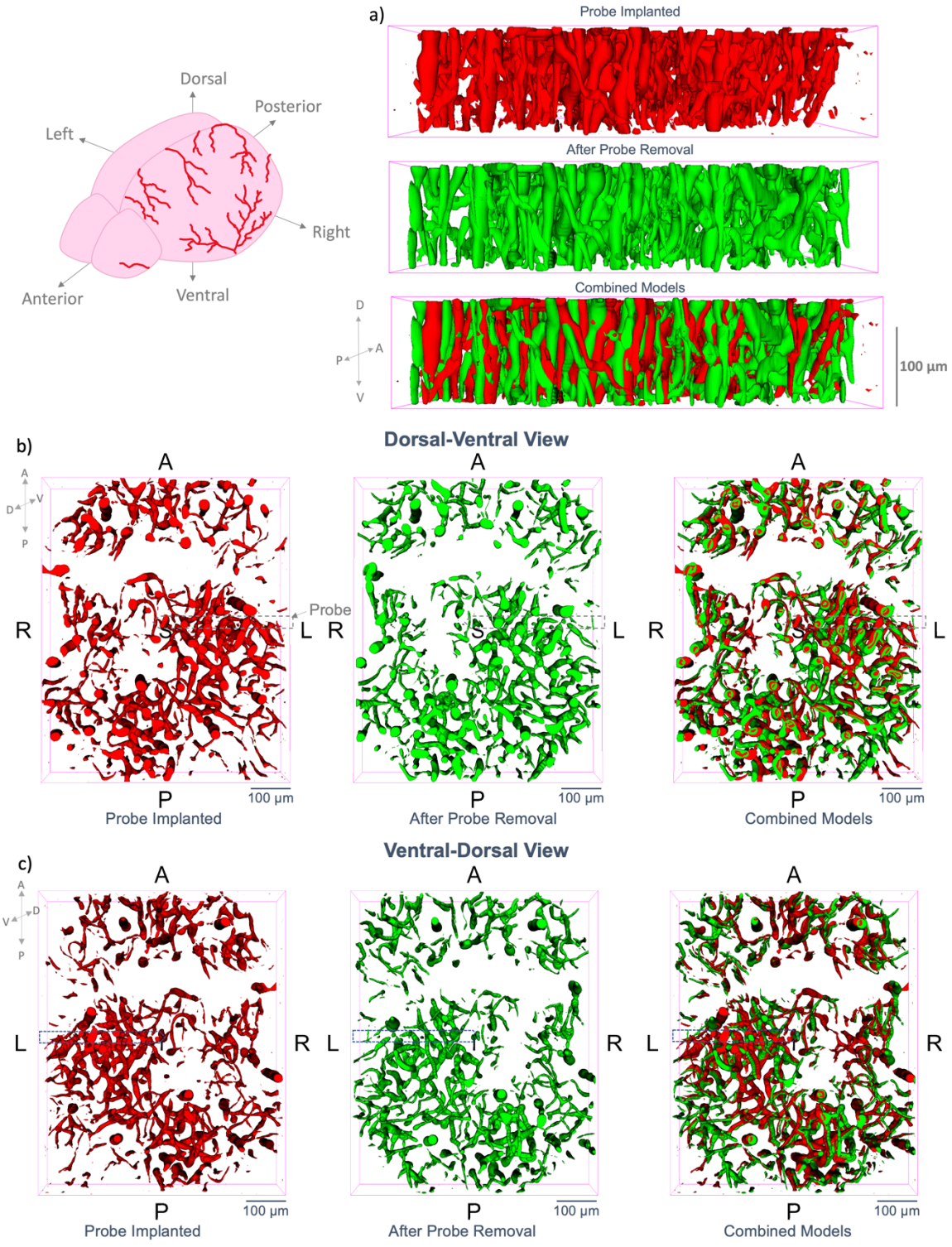
a)
Probe Implanted
After Probe Removal
Combined Models
Dorsal
Posterior
Left
Right
Anterior
Ventral
D
A
P
V
100 µm
b)
Dorsal-Ventral View
A
P
R
L
Probe
100 µm
Probe Implanted
After Probe Removal
Combined Models
c)
Ventral-Dorsal View
A
P
L
R
100 µm
Probe Implanted
After Probe Removal
Combined Models

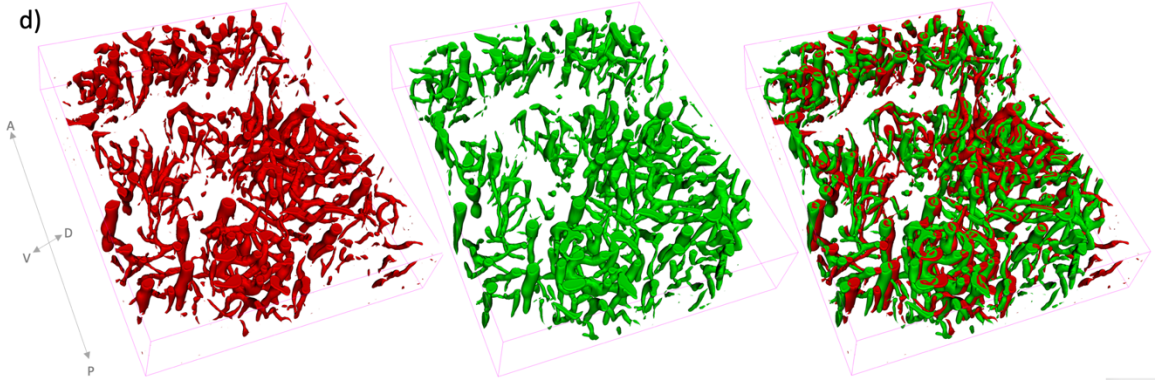

Figure 7.8: Model of vasculature during probe implantation and after probe removal. Outline of probe is shown with dashed gray lines. Vasculature during probe implantation is shown in red. Vasculature after probe removal is shown in green. a) Cross sectional view (posterior facing outwards to anterior). b) Dorsal to ventral view (from brain surface towards deeper layers). c) Ventral to dorsal view. d) Side view.

7.4.1 Quantification of vasculature displacement

Once models of vasculature during and after probe implantation were generated, we used the model-to-model distance plugin to examine displacement between the two models (Budin et al., 2015; Quammen et al., 2022). Using this quantification method, the absolute closest points between the two models were taken to determine the displacement at each point in vasculature (Budin et al., 2015). In this method, points on surfaces of the models were generated and the absolute Hausdorff distances were computed between the closest points of the two model (Budin et al., 2015). These distances were then saved as a point data array and mapped to the model's surfaces (Figure 7.10). The model's displacement values (Figure 7.11) agree with the raw projected images the models were derived from (Figure 7.2). Examination of vector magnitude displacement across all points in the vasculature models reveal an average displacement of 7±7 μm displacement and median displacement of 5 μm during probe implantation and after probe removal (Figure 7.9). This indicates that

vasculature displacement is not significant from when the probe is implanted to when the probe is removed.

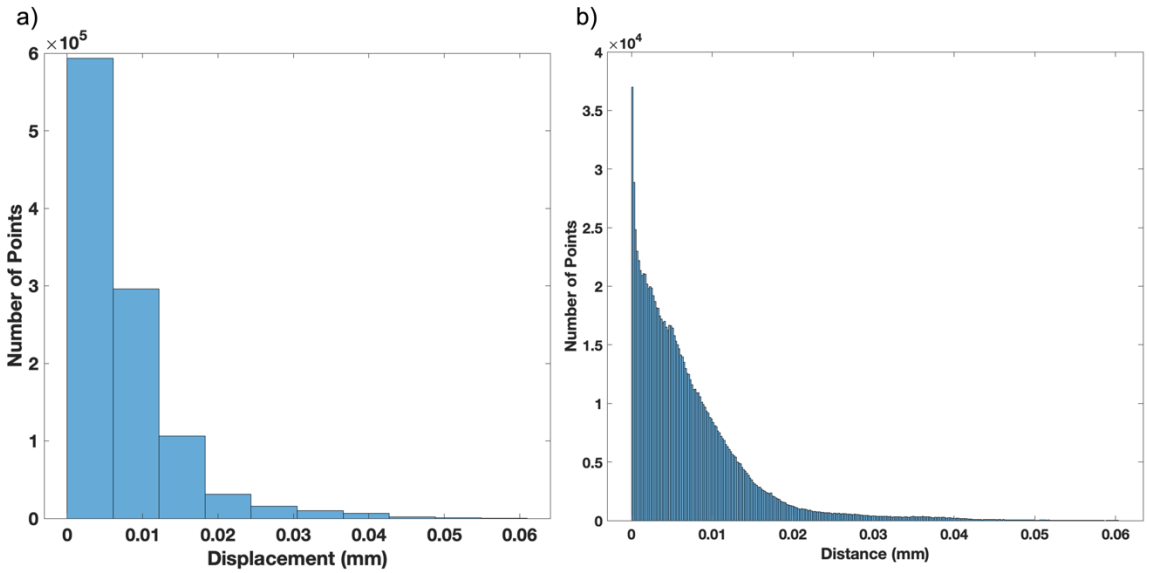

Figure 7.9: Histogram of vector magnitude displacement between probe implantation and removal models. a) Bin set to 5 μm. b) Bin size reduced to 0.2 μm.

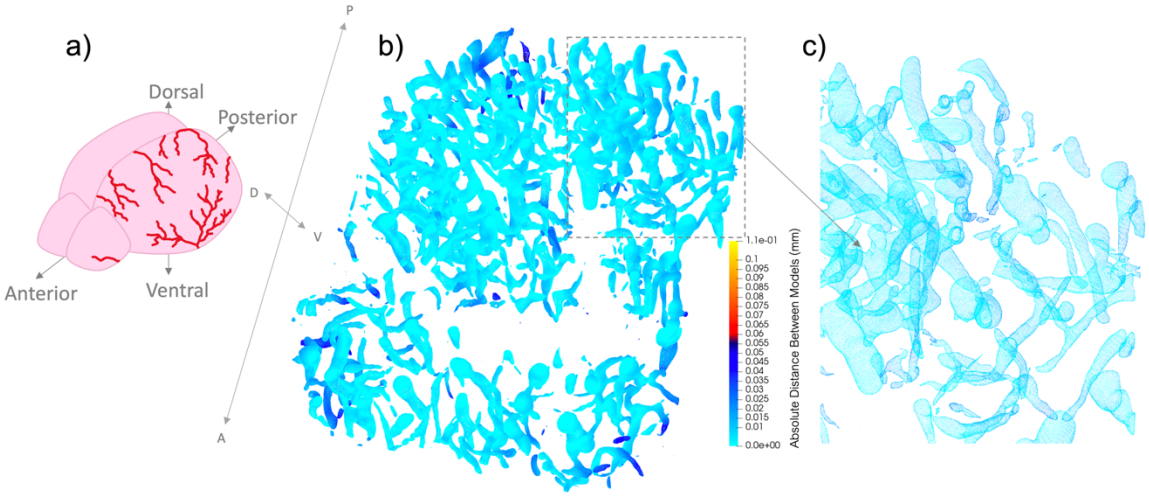

Figure 7.10: Model to model distance output showing points sampled along the model during analysis and corresponding displacement between models. a) Orientation of brain vasculature b) Output displacement model with orientation shown with arrows and indicated as follows: dorsal (D), ventral (V), anterior (A), and posterior (P). c) Zoom-in of displacement models with points along the surface color code by their displacement between models.

7.4.2 Visualization of vasculature displacement caused during probe insertion

To aid with downstream analysis and data visualization, output (vtk) files generated from the model-to-model distance plugin were imported into the data analysis and visualization platform, ParaView (Ahrens et al., 2001). In this analysis, we displayed the distances calculated by the vector magnitude between points on the two models.

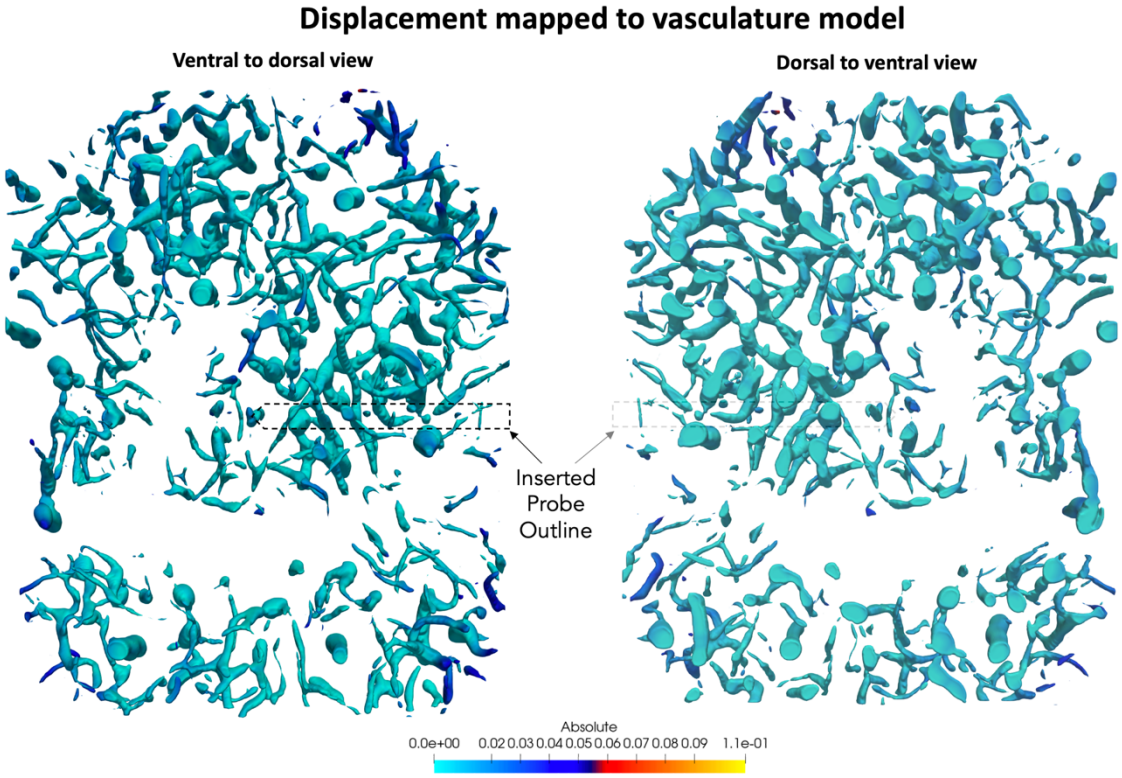

Figure 7.11: Color map of displacement in vasculature system between probe implantation and removal. Absolute displacement is measured in units of mm and color coded. At most points there is little displacement (below 20 μm).

7.4.3 Examination of vasculature and morphological changes over time during probe implantation

Examination of the probe insertion site over long periods of time additionally helps to elucidate small morphological changes such as the possible apoptosis of damaged neurons during implantation or to examine in vasculature flow at different time points (Figure 7.12).

A time-series of the probe and the surrounding tissue was taken, and color coded by time. As the neuron died, it pushed out the surrounding cell structures (Figure 7.12a) and surrounding capillaries (Figure 7.12b). The concurrent time-lapse images of the probe, vasculature, and neurons made possible by this setup can be used to monitor dynamic changes in blood flow and biological processes like inflammation caused by neural probe implants.

In future studies, this imaging strategy can be used on mice expressing markers for inflammation to examine the brain's biological response to chronic probe implants overtime. Using this method, it would be possible to monitor spatiotemporal immune responses and their subsequent effects on ephys signals. Some important biological responses to monitor are the microglia immune response, which is known to occur within minutes of implantation towards the sites of injury (Filiano et al., 2015; Kozai et al., 2012) or the recruitment of nearby astrocytes to the injured areas (Shinozaki et al., 2017).

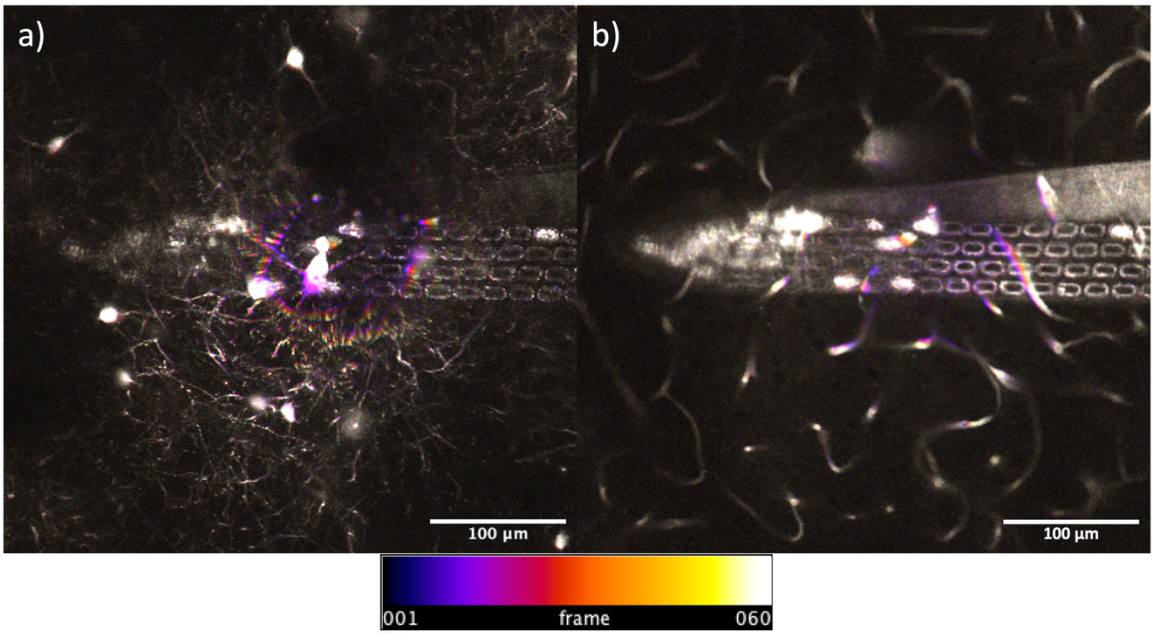

Figure 7.12: Displacement of surrounding structures over time. Temporal color coding of each frame in the time series. Each frame was taken after a second. a) Neuron staining. b) Vasculature staining.

7.5 Conclusion

In conclusion, we demonstrate minimal damage during probe implantation with little detectable bleeding during imaging and minimal displacement of vasculature structures and neurons. 3D modeling of the vasculature during probe implantation and after probe removal enabled quantification of the displacement across different areas. Using this method, we measure an average displacement of 7±7 µm and median displacement of 5 µm during probe implantation and after probe removal. We also can detect morphological changes around the probe such those caused by apoptosis from neurons damaged during probe insertion. This will be especially important to assess different probe designs and help design minimally invasive, biocompatible probes. By imaging how the brain tissue reacts in real-time to the probe, we can test different probe shank shapes and coatings, which will aid in the design of

neural probe implants with low reactivity to the brain tissue. The minimal damage demonstrated by our probes is also especially important for preserving the location of the neurons around the probe. This is important so that we can map the functional activity of each neuron to its position in the brain and minimize damage to neuron cell bodies caused by implantation during ephys recording.

Chapter 8

CHANNELRHODOPSIN MICE LINES FOR DETERMINISTIC CONTROL OF NEURON ACTIVITY AND BENCHMARKING OF NEURAL PROBES

8.1 Introduction

The main goal of this chapter is to establish a channelrhodopsin mouse model and two-photon setup that, with our neural probe, addresses our goal of benchmarking the detection limits of extracellular recording using multisite silicon neural probes. In this chapter, we describe various channelrhodopsin mouse models with moderate to sparse expression of channelrhodopsin and demonstrate effective blue-light dependent silencing. The sparse to moderate expression of channelrhodopsin enables targeted single neuron activation or silencing with blue light that is vital for deterministic control of surrounding neural circuitry activity. We also established concurrent imaging of surrounding neurons and ephys recording *in vivo* in these channelrhodopsin expressing mice. We demonstrate recording of high-quality ephys data and effective silencing of spiking activity with blue LED lights. These methods can be used in the future to study the effect of single neuron stimulation on local cortical circuits. This setup could also be used to deterministically control the amplitude and frequency of spikes from surrounding neurons at various distances to benchmark the detection limits of silicon based ephys probes in future studies.

8.2 Why Channelrhodopsin?

We used channelrhodopsin labeled neurons to enable optogenetic control of targeted single cell excitation with blue light. Additionally, adeno-associated virus (AAV) was used

to deliver channelrhodopsin driven by cell-specific promoters and allowed for targeted genetic expression of certain neuron populations. The specific neuron cell type examined in this paper is interneurons (specifically expressing the Gad2 promoter). Interneurons were chosen due to their sparsity in the cortex, role in modulating long-range sensory processing, well-defined connectivity, and established characterization of their locations with whole-brain mapping (Sun et al., 2019).

8.3 The importance of sparse channelrhodopsin labeling

For neurons to be individually stimulated, each labeled neuron needs to be sufficiently separated from other surrounding neurons so that photostimulation of one neuron will not inadvertently stimulate the processes or soma of another neuron. This allows the stimulated neurons to be approximated as point sources for easier modeling and mapping of the captured ephys signals to the stimulated neuron. Additionally, the infection should also not be too sparse or there will be too few neurons within the detection limits of the probe to stimulate. To achieve broad labeling of channelrhodopsin in the brain, we administered the viral vectors systemically. To achieve sparse labeling, we titered various amounts of virus injected into the virus and the adjusted viral incubation time (Table 6). To access the expression, we imaged the fixed histological brain slices. Additionally, we chose to label GABAergic interneurons to maintain sparsity in the brain.

8.4 Why label GABAergic interneurons (with *Gad2* expressing promoter)

γ-aminobutyric acid (GABA)ergic interneurons make up 20% of cortical neurons and are crucial for regulating neocortical development, synapse formation, and coordinating neuronal network activity (Chu & Anderson, 2015; Kepecs & Fishell, 2014). Disruption of GABAergic activity is implicated in a number of neurological diseases such as

schizophrenia, bipolar disorder, and epilepsy; understanding these mechanisms is crucial for improved treatment strategies of these neurological diseases (Benes & Berretta, 2001). Additionally GABAergic interneurons localize in precise areas in cortical layers and their distribution is well characterized (Fazzari et al., 2020; Tremblay et al., 2016). Interneurons are well separated in the cortex so individual interneuron can be more easily stimulated without unintentionally stimulating neighbors cells (Hoshino et al., 2021). We tested two mice lines whose inhibitory GABAergic interneurons expressed channelrhodopsin. In the first mice line, expression was directed to inhibitory GABAergic interneurons by the glutamate decarboxylase 2 (*Gad2*) promoter and in the second mice line, expression was direction by the vesicular GABA transporter (*VGAT*) promoter.

8.4.1 GABAergic interneuron expressing channelrhodopsin line: Gad2-IRES-Cre infected with Cre-activated AAV expressing humanized ChR2

To maintain a sparsely labeled model we titered the amount of channelrhodopsin expressing AAV used to transduce a mouse line expressing Cre recombinase in its GABAergic interneurons (Table 6). *Gad2-IRES-Cre* knock-in mice were infected with a AAV expressing Cre-activated humanized ChR2 (hChR2) (pAAV-EF1a-double floxed-hChR2(H134R)-EYFP-WPRE-HGHpA, Addgene #20298) (Figure 8.1). The *Gad2-IRES-Cre* line expresses Cre recombinase in GAD2 positive neurons (Taniguchi et al., 2011). When the AAV is injected into the mouse, expression of Cre recombinase causes serial recombination of the transgene resulting in the fixed orientation of the ChR2-eYFP transgene in the mouse. As a result, GABAergic interneurons are labeled. When infected with the Cre-activated channelrhodopsin construct, we could control GAD2 cell activity via optogenetic stimulation. The IRES (internal ribosome entry site) is used to coexpress multiple genes

under the same promoter (Shaimardanova et al., 2019). The channelrodopsin plasmid was packaged in the AAV-PHP.eB capsid because the AAV-PHP.eB capsid variant has more effective transduction of the whole brain via intravenous delivery C57BL/6J mice than Adeno-Associated Virus 9 (AAV9) (Mathiesen et al., 2020). Intravenous delivery is preferable to intracranial bolus injections because intravenous delivery is less invasive and provides widespread gene delivery throughout the nervous system (Foust et al., 2009). Additional benefits of this system are there are *Gad2* Cre-driver lines that exist and can be transduced with AAV PHP.eB capsid. Additionally, Gad2 expression is well documented, and labeled neurons are well separated in the brain (Hoshino et al., 2021; Tremblay et al., 2016). Also, the H134R mutation in the humanized channelrhodopsin-2 (hChR2) protein generates larger photocurrents compared to the wild-type channelrhodopsin-2 (ChR2) (Zhang et al., 2010).

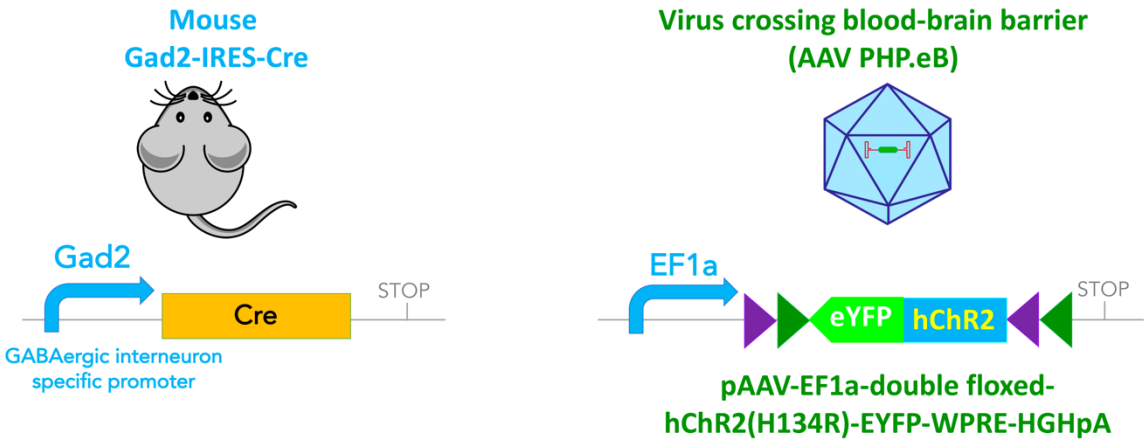

Figure 8.1: Channelrhodopsin model and infection strategy for sparsely labeled cortical GABAergic interneurons.

8.4.2 Intravenous Viral Infection with Retro-Orbital Injection

Uniform labeling of channelrhodopsin in the brain was achieved with intravenous delivery of the virus. Systemic intravenous administration into the bloodstream was preferred over direct bolus injections to the brain because it is minimally invasive. Vectors were packaged into AAV-PHP.eB capsid that is capable of crossing the blood-brain barrier with intravenous administration and allows for broad, well distributed transduction of cells in the brain by AAV vectors (Chan et al., 2017).

The animal procedures for viral infections are summarized as follows. All procedures were approved by the California Institute of Technology Institutional Animal Care and Use Committee (IACUC) and Institutional Biosafety Committee (IBC). Male mice Gad2-IRES-Cre (strain code: 010802) and VGAT-ChR2-EYFP line 8 (strain code #014548) were purchased from Jackson Laboratories. AAV vectors (pAAV-EF1a-double floxed-hChR2(H134R)-EYFP-WPRE-HGHpA; Addgene, 20298-PHPeB) were administered through injection in the retro-orbital sinus of adult mice (4-5 weeks of age) following acclimation (Chan et al., 2017). A 30-gauge needle, filled with the viral solution was diluted to the correct titer in PBS with 0.001% Pluronic F-68 solution, was inserted into the medial canthus at a 30-45° angle through the conjunctival membrane; virus was then slowly injected into the sinus (Chan et al., 2017). Viral titer $10^9 – 10^{11}$ vector genomes (vg) were injected into each mouse with 80 μL. Afterwards, the virus was allowed to express for 3-5 weeks before imaging experiments.

8.4.2.1 Histology: Examination of expression sparsity in channelrhodopsin mice lines

Mouse were sacked after 21-52 days post AAV infection and the brain was fixed and sliced to examine the expression levels of Enhanced Yellow Florescent Protein (EYFP) labeled channelrhodopsin. We examined brain slices from mice infected with various AAV titers to ensure expression was sparse in the cortex. Complete mouse brain fixation was achieved using transthoracic cardiac perfusion without thoracotomy following methods listed in (Eichenbaum et al., 2005). This method is preferred because it is minimally invasive, uses the beating heart to circulate the fixative, and better maintains the physiology of the brain (Eichenbaum et al., 2005). The fixative solution consisted of a 4% paraformaldehyde and 4% sucrose in 0.1 M phosphate buffer (pH 7.2) (Electron Microscopy Sciences, Hatfield, PA, USA Catalogue #1224SK). Fixative solution was injected into anesthetized mice using a 30-gauge needle into the left ventricle of the heart. Following perfusion, the fixed brain was removed and placed in perfusion wash, which consisted of Phosphate Buffered Saline 0.1M Phosphate Buffer pH 7.2-7.4) (Electron Microscopy Sciences, Hatfield, PA, USA Catalogue #1219SK). Fixed brains were then sliced to a thickness of 100 to 200 μm using a microtome (Leica, VT1200 S).

8.4.2.2 Confocal imaging of fixed brain slices

Histologically fixed brain slices were imaged on an inverted Zeiss LSM 710 confocal microscope. Slices were mounted onto glass slides and coverslips were placed on top of the brain slice. To image the channelrhodopsin labeled with eYFP, we used a 488 nm laser paired with a 530/30 nm bandpass filter on the confocal microscope. Confocal microscope imaging

was performed at the Biological Imaging Facility at Caltech. Images were obtained using a 20X objective (Zeiss Epiplan-NEOFLUAR Objective, 20x/0.50 DIC).

8.4.3 Gad2-IRES-Cre infected with Cre-activated AAV expressing humanized ChR2

To achieve sparse labeling, we titered the amount of channelrhodopsin expressing AAV injected in transgenic mouse lines expressing Cre in GABAergic interneurons (*Gad2-IRES-Cre*) and abbreviate these mice as the Gad2 mice line. In these mice, we need the neurons to be labeled sparsely so that labeled neurons are well separated to enable single cell stimulation, but also dense enough so that there would be enough labeled neurons within the detection limit around the probe. From confocal images of brain slices from infected mice, we determined the dosages leading to sparse expression of channelrhodopsin are between $3x10^9$ vg of virus incubation (with well separated and labeled interneurons in brain slices) and below $5x10^{11}$ vg (with dense processes nearby interneuron cell bodies) (Figure 8.2).

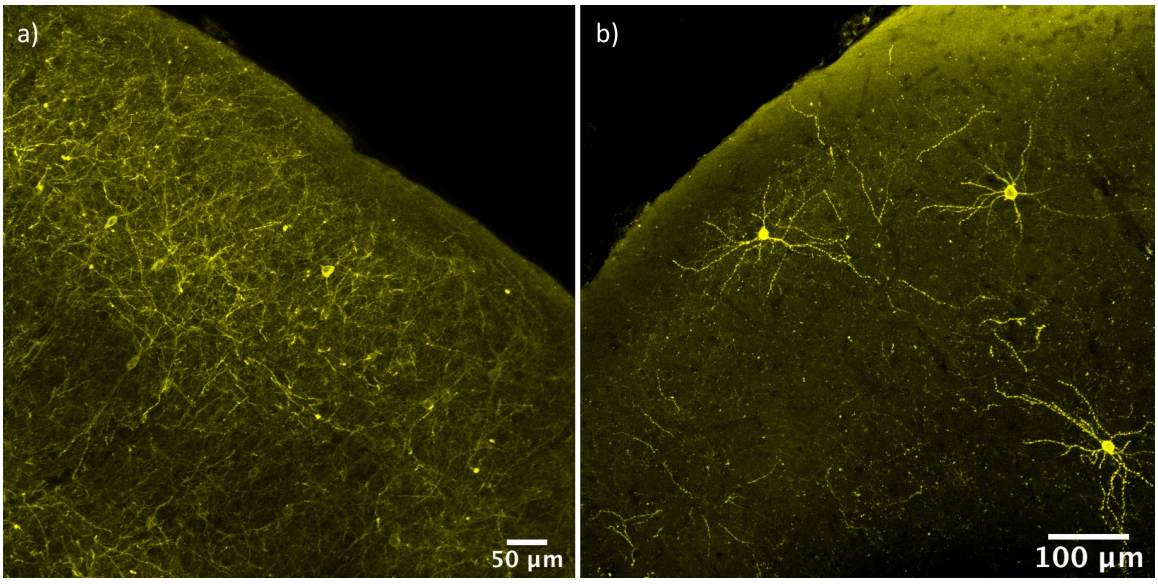

Figure 8.2: Distribution of hChR2-eYFP (yellow) labeled GABAergic interneurons in fixed slices infected with various viral titers. a) Mouse infected with PHP.eB with $5x10^{11}$ vg of AAV through retro-orbital injection (P52) after 21 days from viral injection. b) Mouse infected with 3 x 10^9 vg PHP.eB for 52 days.

Table 6: Summary table of viral dosages, incubation times, and mouse age for Gad2-IRES-Cre infected with Cre-activated AAV PHP.eB expressing humanized ChR2

Viral Titer per Mouse in Vector Genomes	Virus incubation time	Age of mouse (during imaging)	Expression Intensity	Expression Sparseness	Conclusions
$2x10^9$ vg	32 days	P63	Dim	Very sparse	Little expression
$3x10^9$ vg	28 days	P59	Dim	Very sparse	Little expression
$3x10^9$ vg	52 days	P101	Bright	Well separated	Bright expression and good density
$3x10^{10}$ vg	28 days	P86	Dim	Well separated	Little expression
$3x10^{10}$ vg	90 days	P94	Bright	Very dense	Densely labeled neurons
$5x10^{11}$ vg	21 days	P52	Bright	Very dense	Densely labeled neurons

*Viral titers are listed in vector genomes (vg), age of mouse listed by postnatal (P) days, and viral incubation times are listed by days after viral injection.

8.4.4 VGAT-ChR2-EYFP

Another transgenic model tested was the *VGAT-ChR2-EYFP* line 8 also known as B6.Cg-Tg(Slc32a1-COP4*H134R/EYFP)8Gfng/J (JAX #014548), which we will abbreviate as the VGAT mice line. In this mouse model, GABAergic inhibitory interneurons were labeled through the vesicular GABA transporter (VGAT) with hChR2-H134R to allow for rapid control of motor behavior via optogenetic stimulation (Zhao et al., 2011). This established mouse line allows for more reproducibility across different mice than the Gad2 transfected models. Additionally, in this model, optogenetic expression and functionality are well characterized and able to sustain high fidelity, high frequency firing in response to blue

light stimulation at 80 Hz or higher frequencies (Zhao et al., 2011). Confocal imaging of our fixed brain slices reveals a moderate expression of EYFP labeled channelrhodopsin.

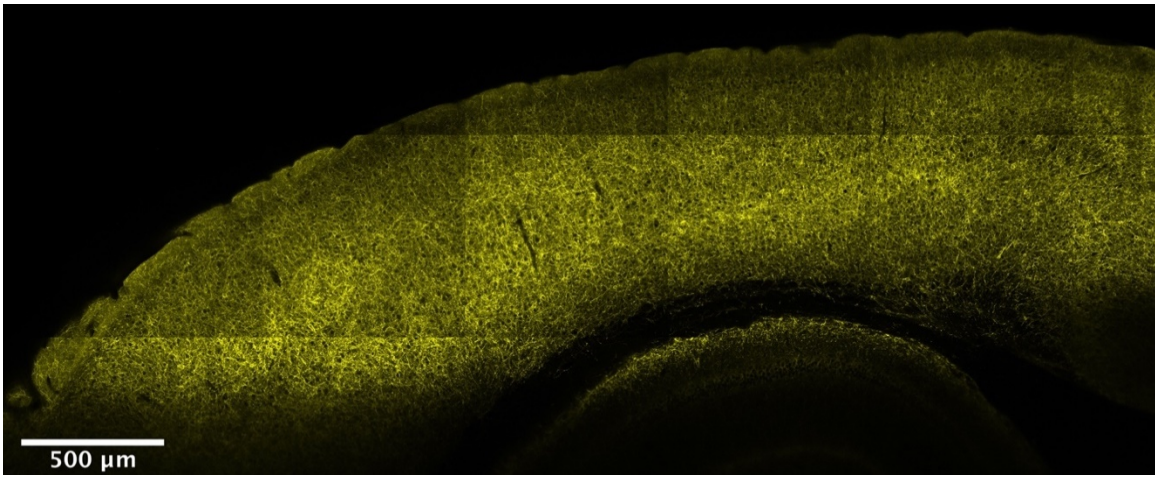

Figure 8.3: Cortical distribution of GABAergic interneurons labeled in VGAT transgenic line. Images taken from fixed cortical brain slice. GABAergic interneurons were labeled with EYFP (*yellow*).

8.5 Two-photon imaging of optogenetic models and neural probe ephys recording

Simultaneous extracellular recording with multisite silicon neural probe with two-photon imaging of the probe and stimulation of surrounding channelrhodopsin expressing neurons is a novel approach and has not been reported previously. This is especially important because the two-photon laser can deterministically activate channelrhodopsin neurons and stimulate action potential of various frequencies and amplitudes that can be used to benchmark the detection of the ephys neural probe. Using the two-photon microscope, we can image the electrodes on the neural probe, deterministically excite neurons at a known distance from the probe, and then correlate recorded ephys signals from the probe back to the known positions of the stimulated channelrhodospin neurons using the two-photon laser. This data helps us achieve our goal of benchmarking the detection limits of the neural probe

by controlling and reconstructing the activity of the surrounding neurons since we know the positions of each electrode, neuron being stimulated, and resulting spike activity.

This method takes inspiration from other works that combine intracellular electrophysiology and multi-photon calcium imaging *in vivo* (Moreaux & Laurent, 2008). Some examples include voltage recording (recorded with patch clamp) with simultaneous calcium activity measured with fluorescent indicators (with Oregon Green BAPTA) imaged with two-photon in the locust brain (Moreaux, 2007) or patch clamp recordings with simultaneous multisite recording with extracellular ephys neural probes in mice (Hulse et al., 2016). To check channelrhodopsin expression levels *in vivo*, mice were examined under the two-photon imaging following the same setup as described in Chapter 5. In this process, mice were placed under a two-photon microscope (Thor Lab) and imaged using a Leica 25X water immersion lens (Leica HCX IRAPO). Unless otherwise indicated, the two-photon wavelength was set to 960nm (250 kHz) for stimulation and imaging. The mouse *in vivo* imaging setup is same as the two-photon setup described in Chapter 5.

8.5.1 Light delivery method

Some common methods to achieve optical activation of channelrhodopsin-2 (ChR2), a light activated cation channel, are wide-field illumination, laser scanning illumination (Wang et al., 2007), one-photon excitation (Mohanty et al., 2008), and micro-light-emitting diode (LEDs) arrays (Ferenczi et al., 2019; Lin, 2012). However, such methods use blue light which has lower penetration in tissue compared to near infrared (NIR) light, limiting blue light's ability to stimulate deeper brain regions (Liu et al., 2021; Mohanty et al., 2008). Additionally, wide-field illumination has low spatial resolution and provides poor spatial selectivity for single neuron simulation (Schoenenberger et al., 2008). One-photon excitation

also lacks optical sectioning and excites opsin molecules above and below the focal plane, leading to increased photobleaching as compared to two-photon excitation (Patterson & Piston, 2000). As such, these methods lack the temporal and spatial resolution needed to selectively stimulate single cells at greater depths.

To address these concerns, we used two-photon laser to excite ChR2. Two-photon provides better temporal and spatial resolution because two-photon excites only molecules in the focal plane. Two-photon microscopy also allows for single cell resolution and targeting light to individual neurons (Packer et al., 2013). Additionally, ChR2 can be stimulated using near-infrared, low power two-photon excitation, reducing the amount of photobleaching and resulting in greater light penetration through the tissue (Rickgauer & Tank, 2009). This single-cell spatial resolution is especially important to help map inputs from individual neurons and selectively stimulate neurons in proximity to the ephys probe.

Since the detection limit of the probe is around 168 μm at most, expression of mice injected with $3x10^9$ vg was too sparse because only a few labeled neurons in a volume would be close enough to be detected by the probe (Figure 8.4). For probe insertion, we decided to increase injected viral titer to $3x10^{10}$ vg for denser labeling (Figure 8.6).

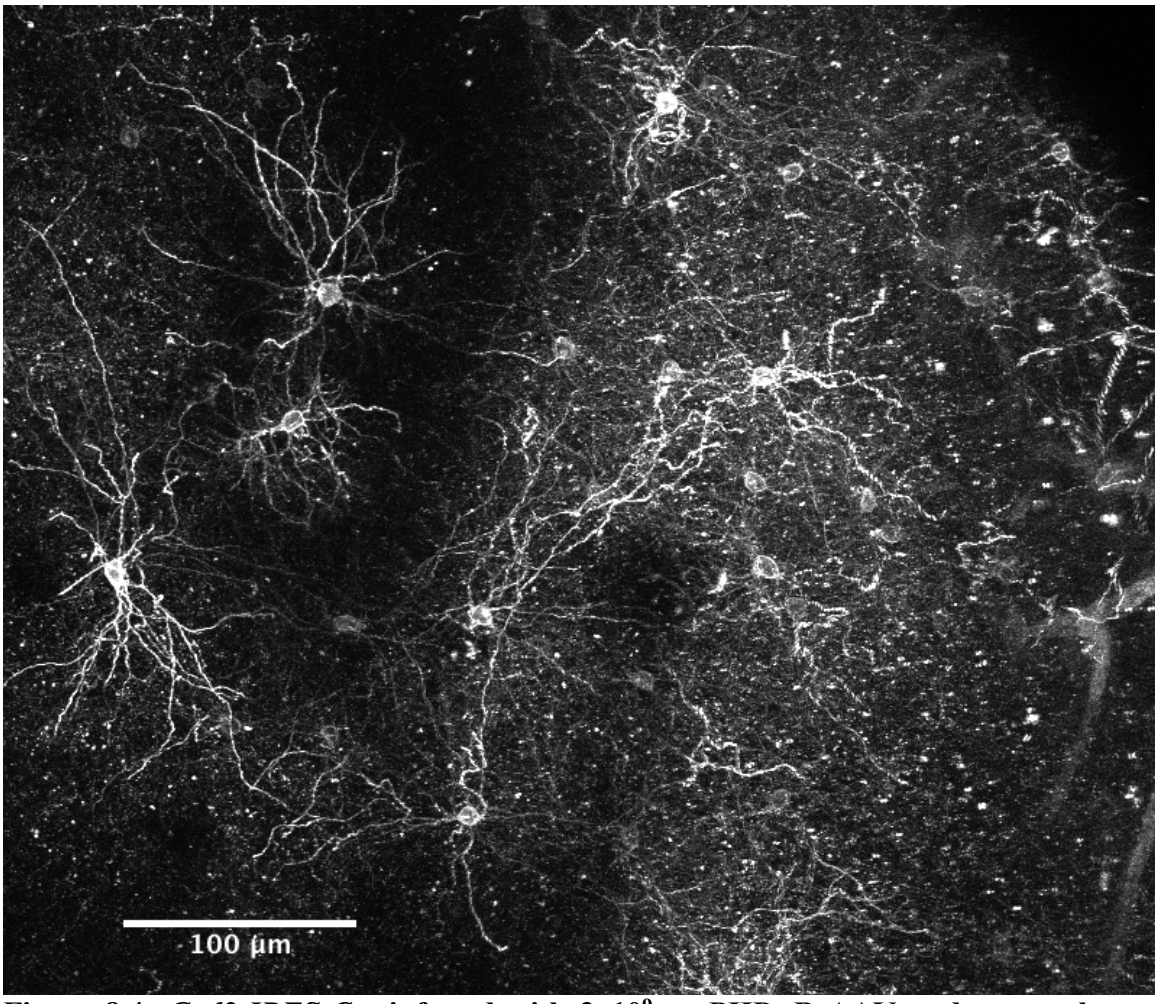

Figure 8.4: *Gad2-IRES-Cre* infected with 3x10^9 vg PHP.eB AAV under two-photon imaging. Maximum intensity projection of layer 1 cortex (obtained from z-stack spanning the surface to 565 µm below the surface).

Additionally, we examined the expression of channelrhodopsin in VGAT mice line, since the mice lines are established and literature has demonstrated extensive functional characterization of blue light controlled action-potential firing (Zhao et al., 2011). VGAT transgenic lines showed moderate expression of ChR2-eYFP in the neuron membrane and processes (Figure 8.5). However, the density of processes from neighboring neurons nearby the cell bodies, makes it difficult to selectively stimulate one neuron without inadvertently

stimulating nearby processes, which makes the Gad2-IRES-Cre line preferable because we can titer the amount of the virus with channelrhodopsin delivered to the mouse.

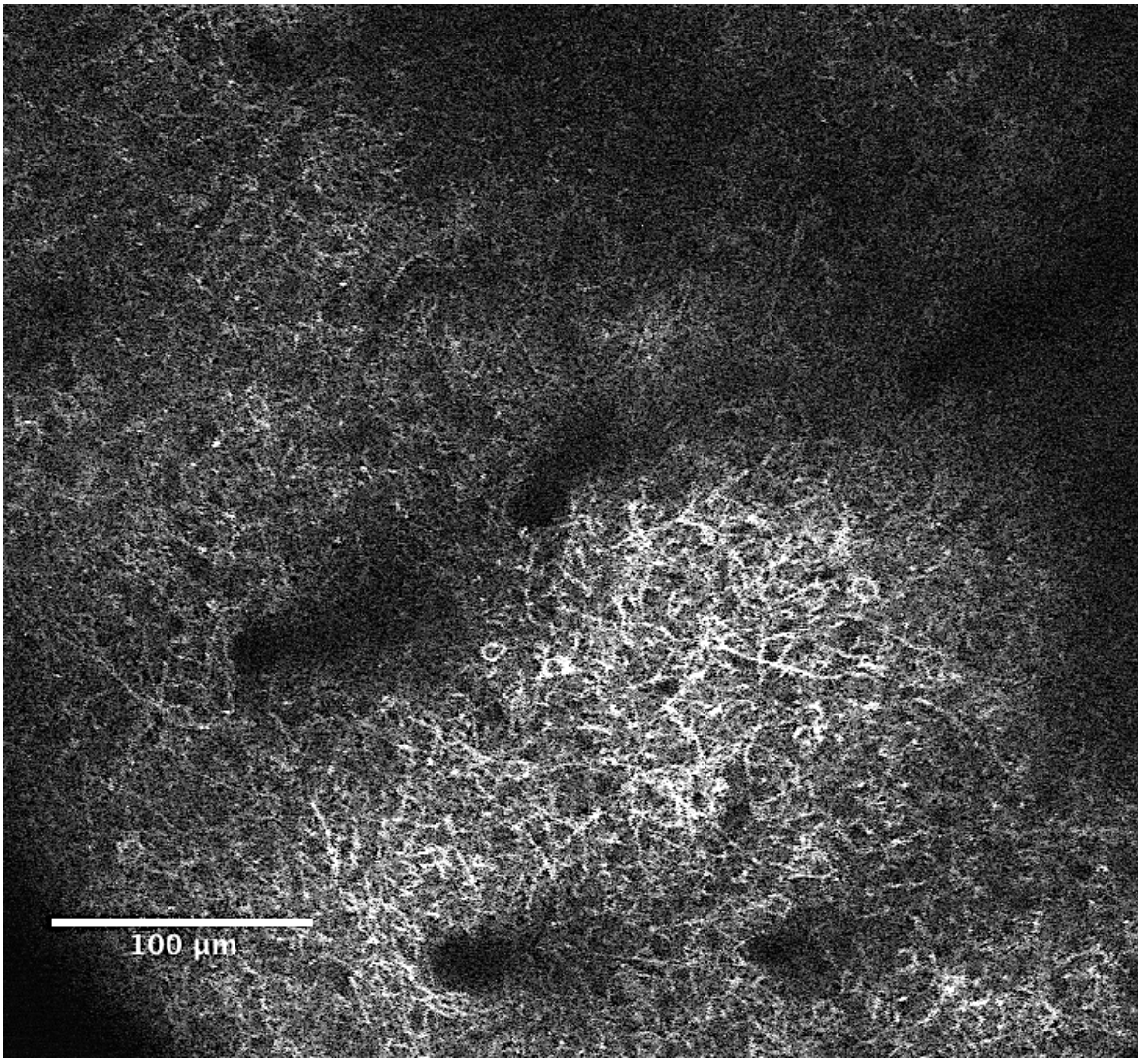

Figure 8.5: ChR2-eYFP cortical expression in VGAT mice line *in vivo*. Expression is shown for the Layer 1 mouse cortex using two-photon imaging *in vivo*. Darker areas are from blood vessels.

8.5.2 Imaging with Ephys Recording

Probes were inserted following methods listed in Chapter 5. Probes were inserted at shallow depths in Layer 1 of the cortex to allow for imaging and lessen the decline of laser power seen at greater depths due to tissue absorption. Channelrhodopsin labeled interneurons

were stimulated with either a two-photon laser or blue LED. Below are images of the Gad2-IRES-Cre and VGAT models during recording with our ephys neural probes (Figure 8.6 and 8.7). Using this two-photon setup, we can image the electrodes on the neural probe, deterministically excite neurons at a known distance from the probe and map the recorded ephys signal from the probe back to the known positions of the stimulated channelrhodospin neurons using the two-photon laser. This data can help us benchmark the detection limits of the neural probe by controlling and reconstructing the activity of the surrounding neurons in future studies.

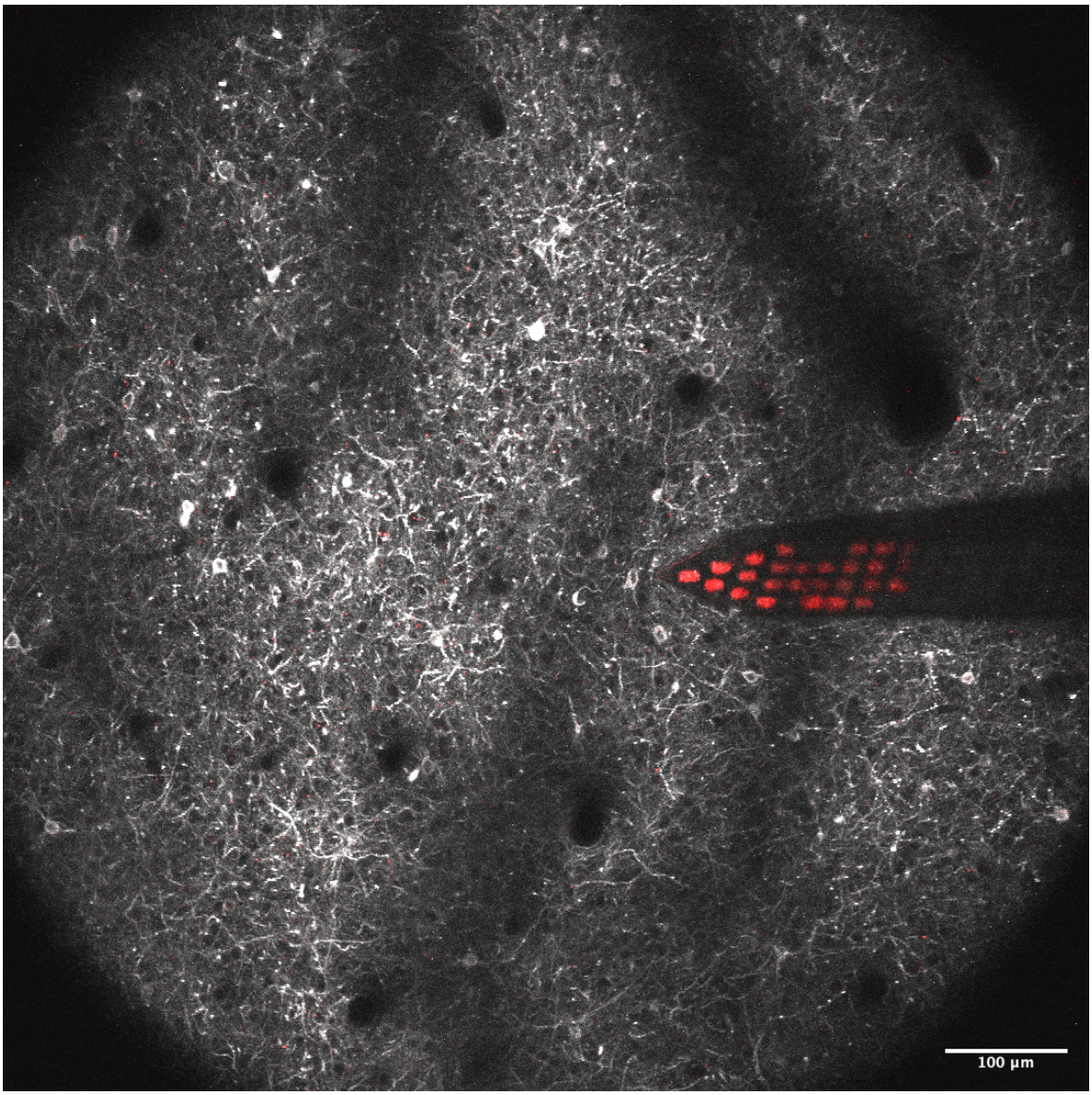

Figure 8.6: Neural probe inserted in *Gad2-IRES-Cre* infected with AAV-PHP.eB injected intravenously. ChR2 labeled with EYFP is in white and electroplated pads are red. A viral titer of $3x10^{10}$ vg per mouse was used.

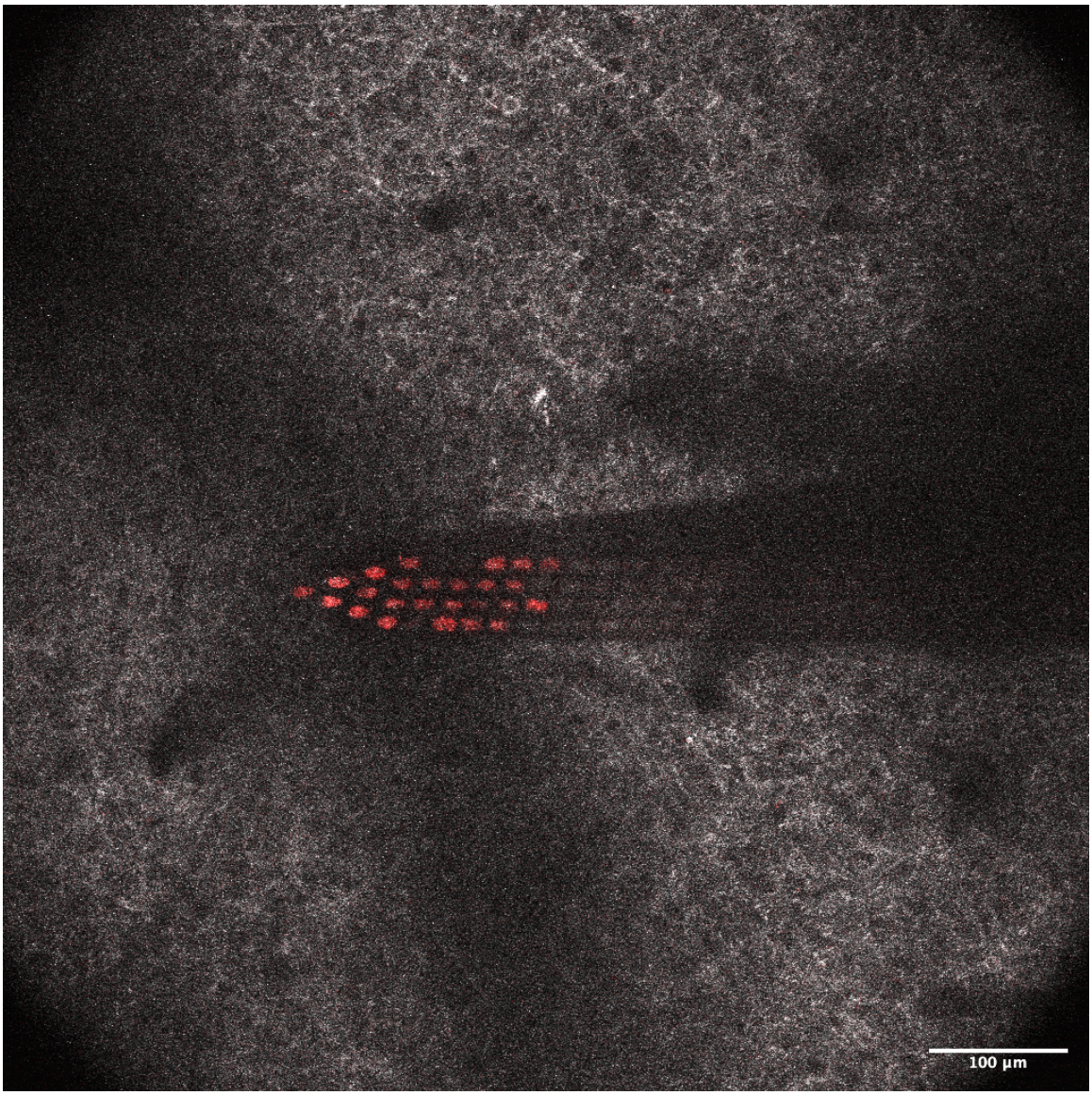

Figure 8.7: Neural probe inserted in VGAT transgenic line. VGAT interneurons expressing ChR2-EYFP are white and electroplated pads are red.

8.5.3 Photo-electric effect of two-photon absorption on probe surface

During imaging and recording, it was important to recognize and remove artifacts from the photovoltaic effect induced by the two-photon laser on the electrode surface of the neural probe during stimulation and imaging. During the photovoltaic effect, the high optical intensity from two-photon laser onto the silicon and gold electrodes leads to the emission of

photoelectrons and generation of electric currents (Fathpour et al., 2007; Güttler & Queisser, 1969). This emission of photoelectrons induced by the two-photon laser (set to 960 nm and 250 kHz) can be detected on as a biphasic wave during recording with the neural probe (Figure 8.8b). During analysis, recording times with characteristic photoelectric artifacts were removed before spike sorting and downstream analysis. Photoelectric effect noise was only observed when the two-photon laser scanned the probe directly and not when laser scanned adjacent areas around the probe.

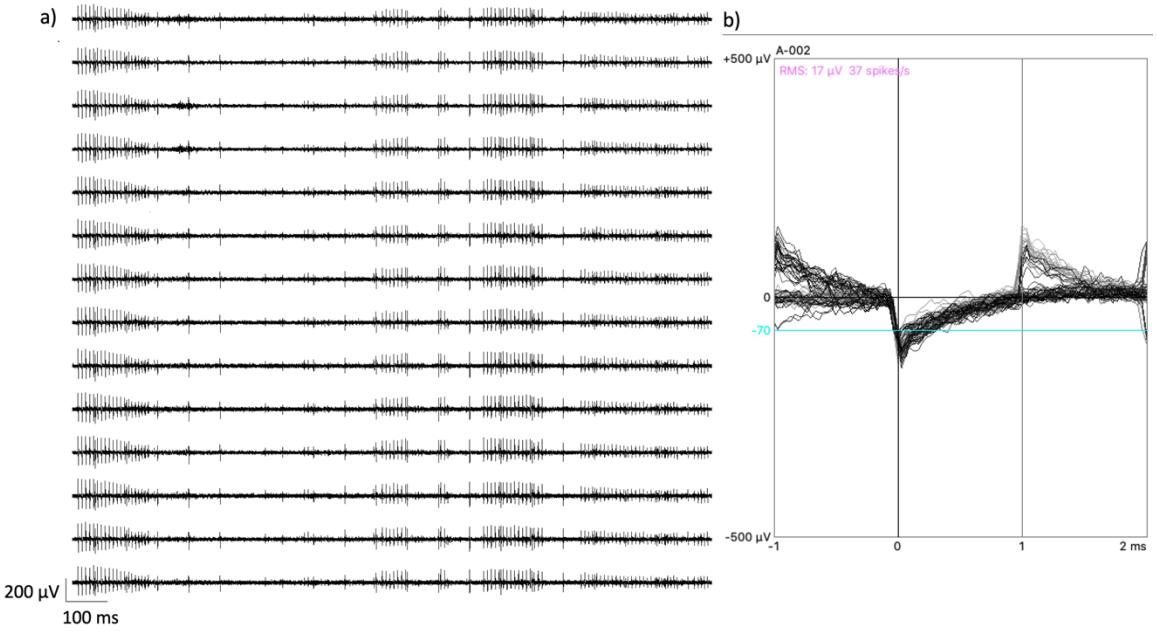

Figure 8.8: Photoelectric effect from two-photon on neural probe. a) Photoelectric artifacts in spike frequency bandwidth (300 Hz - 10 kHz). b) Zoom-in of biphasic wave from two-photon absorption detected on electrodes.

8.5.4 Ephys recording of channelrhodopsin models under two-photon imaging

To test the quality of the recordings, we examined spike activity in between times of light stimulation for Gad2 and VGAT mice lines expressing channelrhodopsin (Figure 8.9 and 8.10). As before, we detected distinct waveforms across multiple pads indicative of

single unit activity (Figure 8.9 and 8.10). These neurons could be resolved by nearby electrodes with wavelengths of highest amplitude closest to the emitting neuron.

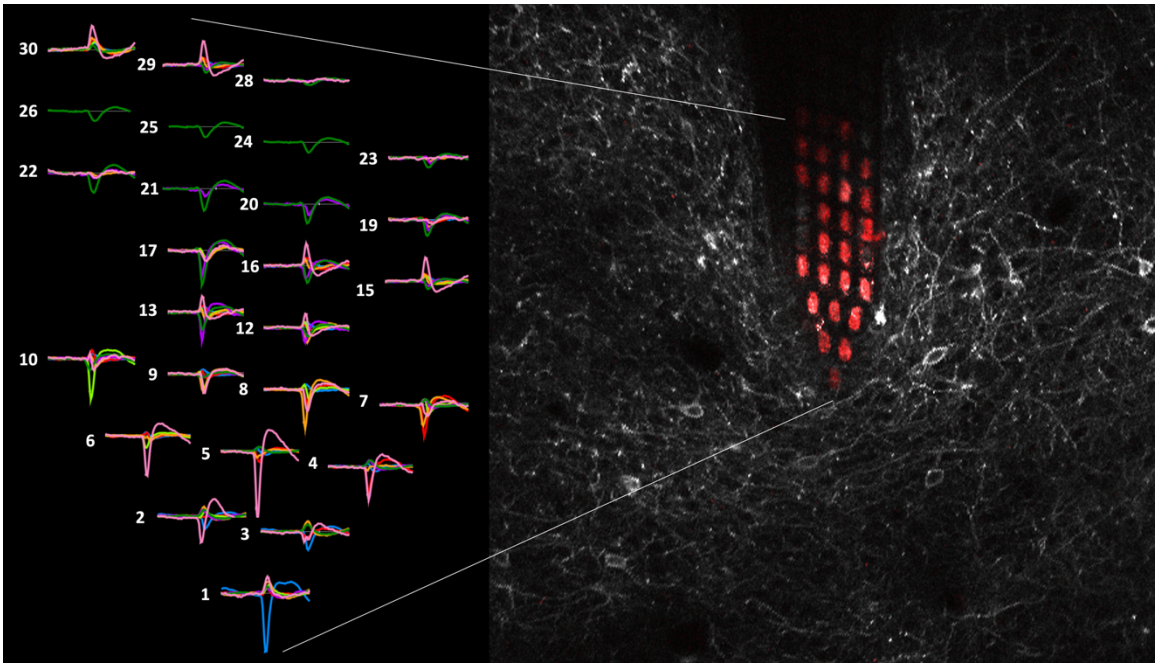

Figure 8.9: Channelrhodopsin PHP.eB transfected Gad2-IRES-Cre mice.

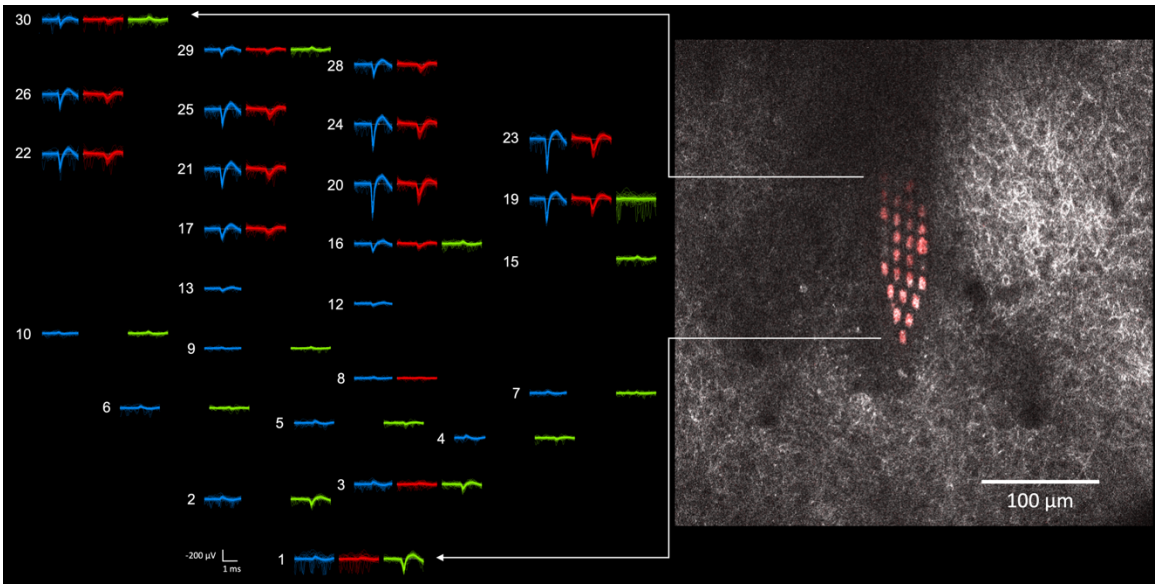

Figure 8.10: VGAT line with corresponding waveforms ordered by position on electrode.

8.6 Limitations

Unfortunately, we did not observe spikes induced by two-photon stimulation in individual neurons. Several factors contribute to difficulties implementing two-photon excitation to stimulate ChR2 (Papagiakoumou et al., 2010). The main issues are: 1) channelrhodopsin's low conductance (below 1pS) (Nagel et al., 2003), 2) the limited density of ChR2 channels that can be expressed on a cell's membrane, and 3) the two-photon laser's small excitation volume; these three factors combined make it difficult to induce sufficient depolarization to trigger an action potential with a two-photon laser (Feldbauer et al., 2009; Papagiakoumou et al., 2010). Neurons have a fairly high membrane resistance and if we assume the cell has a conductance of 50 MΩ, a membrane potential of -60 mV, a reversal potential of 0 mV, and a single channel conductance of 100 fS, it will take approximately 500,000 functional ChR2 to open at a time to sufficiently depolarize the membrane to 15 mV (Lin, 2012). The size of excitation volume induced by the two-photon (thus the optical resolution) is determined by the numerical aperture and excitation wavelength (Rubart, 2004). If we assume we have a two-photon setup with a uniformly illuminated and high numerical aperture objective (numerical aperture 1), then the fluorescence excitation is confined to less than femtoliter volumes around the focal point of the objective, with <1 μm resolution in the *z* direction (Rubart, 2004). These considerations make it difficult to express a high enough number of functional channelrhodopsin proteins in a small volume of the neuron's cell membrane to sufficiently depolarize a cell using a two-photon laser.

One method to address this problem is to sculpt the two-photon excitation light so that the excitation volume is large enough to activate the number of channelrhodopsin

proteins necessary to depolarize the neuron. One method to sculpt the light is to under saturate the back aperture of the objective; however, this method suffers from significant loss in axial resolution (Papagiakoumou et al., 2010; Rickgauer & Tank, 2009). A second method is to use fast scanning of the laser beam across the inferred membrane of the neurons, but a major drawback of this method is its limited temporal resolution (Rickgauer & Tank, 2009). The third method is to use a spatial light modulator (SLM) (Andrasfalvy et al., 2010; Papagiakoumou et al., 2010). Using this method, the SLM is used to shape the 2P excitation beam in order to control the size and shape of the excitation volume (Papagiakoumou et al., 2010). This method allows for low excitation density, large excitation areas, high temporal resolution (millisecond scale), and high spatial (depth resolution <6 μm) resolution optical illumination (Papagiakoumou et al., 2010). The SLM method also allows for targeting of distributed neuron groups at a time, which is especially important in understanding circuit interactions and will aid in close-loop training of neuronal circuits (Russell et al., 2022).

8.7 Silencing spiking activity with blue light LED in VGAT mice

To silence surrounding neurons in channelrhodopsin expressing mice lines, we used blue light LEDs in VGAT mice. The blue light LED was powered with a X-cite fluorescence LED illumination system and a blue bandpass filter (470 nm). Whole-field illumination *in vivo* was delivered through the microscope illumination path and used a dichroic mirror to reflect the 470 nm activation light to the whole brain. No observable photoelectric effect was noticed when the blue light LED was shined on the implanted neural probe. We observe robust optogenetic modulation of large amplitude neuron spike activity in the brain across consecutive electrodes sites on the neural probe with the blue light LED power set to 30-50% (Figure 8.11). This silencing of spike activity is likely due to the activation of the

channelrhodopsin GABAergic interneurons (shown by the small amplitude spikes in the blue dotted box) that inhibit the pyramidal neurons, which emit larger amplitude spikes (red dotted box) (Figure 8.12).

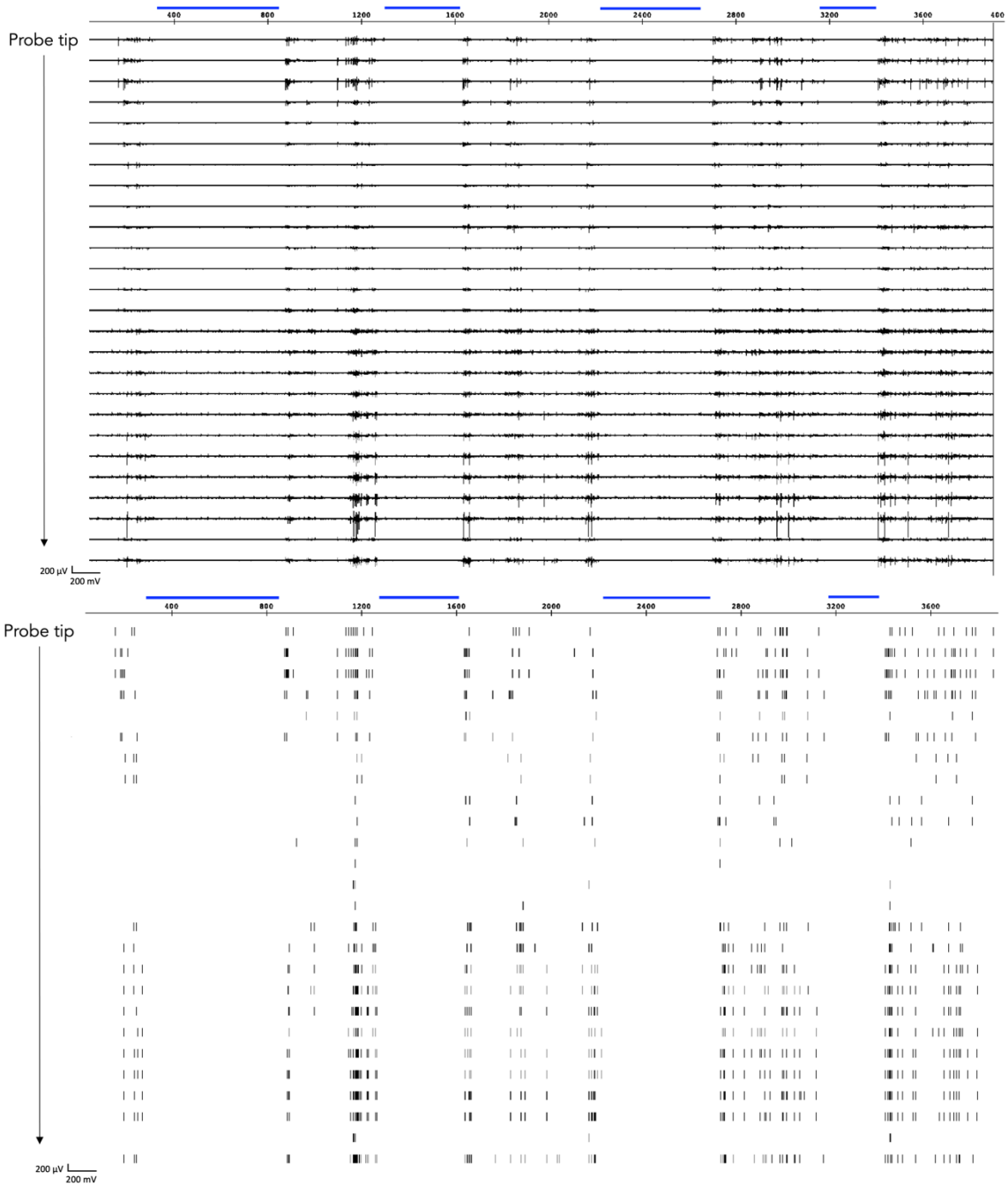

Figure 8.11: Blue light induced silencing in consecutive recording sites of spike bandwidth. Times when blue LED was applied are indicated by blue bars. a) Spike frequency bandwidth (300 Hz - 10 kHz). b) Spike raster.

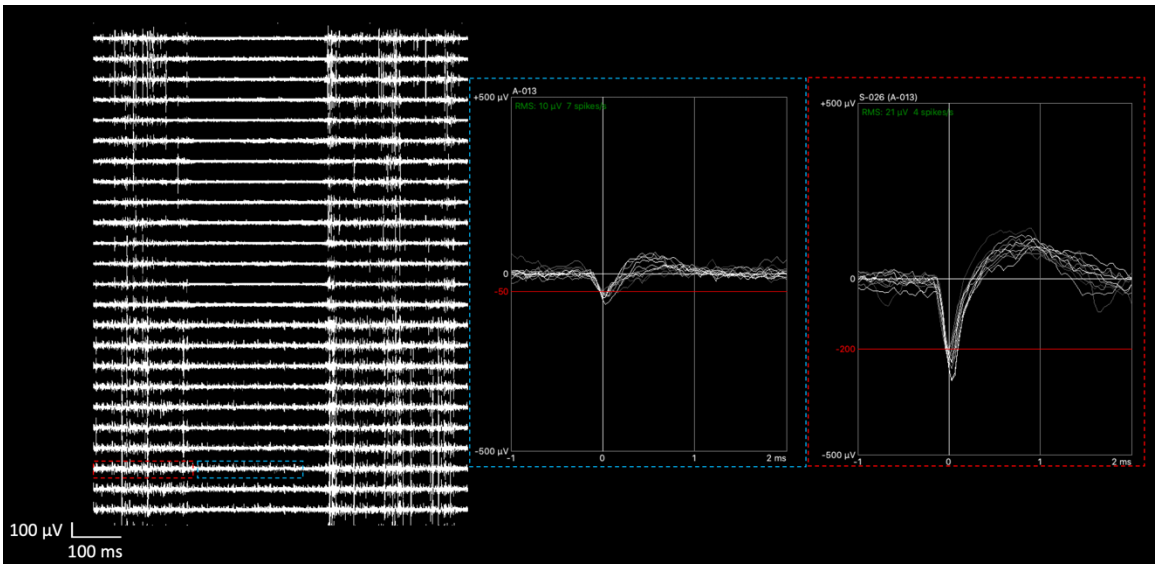

Figure 8.12: Spikes during blue light and without widefield blue light exposure. Blue dotted box shows spikes, possibly from activated interneuron, when widefield blue light was applied. Red dotted box shows spikes, possibly from pyramidal neurons, where blue light was not applied.

8.8 Future Directions: GCaMP6 lines with probe recording and two-photon imaging

Why GCaMP6

Other optogenetic reporter lines of interest are the transgenic lines expressing GCaMP6, which acts as a proxy of activity of surrounding neuronal population by measuring rapid intracellular influxes of Ca2+ (Chen et al., 2013). When combined with our neural probe imaging setup, examination of GCaMP6 mice lines will enable simultaneous recording of ephys activity and correlation to surrounding neural activity. This will provide important benchmarking of the probe's ability to capture ephys activity and a comparison of the ability of optogenetic reporters versus silicon probes to capture brain activity.

8.9 Conclusion

In conclusion, we demonstrate effective sparse, transduction of channelrhodopsin in the mouse brain that in future studies enable point-source, deterministic excitation of single

neurons. Sparse transduction of channelrhodopsin was achieved by testing different titers of viral capsid, mice ages, and viral incubation times. We demonstrate combined two-photon imaging of the channelrhodopsin labeled neuron and the neural probe with extracellular recording. Also, we demonstrate effective silencing of surrounding channelrhodopsin interneurons with blue LED lights.

Future studies would combine SLM or other laser shaping methodologies to enable single-cell excitation with two-photon imaging of the neural probe. This will enable us to better benchmark the ability of the probe to detect spikes of various amplitudes and frequencies at various distances. When combined with chronic implants, the use of two-photon for single neuron stimulation in this setup will enable us to understand how single-cell stimulation alters local cortical circuits activity. After long periods of controlled stimulation, this method might also enable us to drive and modify local cortical circuits in a sustained manner, while recording ephys changes to local brain activity. With two-photon imaging, we can also image fluorescent neurotransmitter reporters to monitor changes in neurotransmitter release that occur when local cortical circuits are modified with single neuron stimulation.

Chapter 9

MICROFLUIDIC PLATFORM FOR MEASURING SYNAPTIC GLUTAMATE RELEASE AND RESPONSE TO NEUROMODULATING DRUGS

9.1 Introduction

This chapter describes development of microfluidic platforms to measure synaptic glutamate release in response to neuromodulating drugs and proposes integration of these microfluidic platforms with CMOS technologies to allow for multiplicity of neurotransmitter flux measurements. To monitor synaptic release, we used a genetically encoded fluorescent protein reporter developed and packaged into viral vectors by the laboratory of Professor Lin Tian at UC Davis (Tian, 2014). To isolate synapses and provide a platform to test different drugs, we used a microfluidic device. This microfluidic device can be interfaced with CMOS contact sensors placed nearby channels containing synapses to record the kinetics of synaptic neurotransmitter release. The large number of pixels on the CMOS chip provides multiplicity and enables collection of larger numbers of synaptic events simultaneously, which provides signal averaging to remove noise in order to obtain more accurate kinetic measurements of synaptic release.

9.2 Split-iGluSnFR sensor for detecting synaptic glutamate release

The split-iGluSnFR sensor consisted of a pre-synaptic (pre-iGlu) and post-synaptic (post-iGlu) components expressed in either the post-synaptic or pre-synaptic neurons, respectively (Figure 9.1) (Tian, 2014). The split-iGluSnFR is expressed using a neurexin promoter for pre-iGlu and neuroligin promoter for post-iGlu to allow for labeling of

presynaptic and postsynaptic parts respectively. The split-iGluSnFr sensor is based on previously developed iGluSnFR (Marvin et al., 2013) and detects glutamate in a similar manner. The pre-iGlu and post-iGlu components each consisted of one half of a glutamate binding protein (*Escherichia coli* GltI) and one half of a circularly permuted green fluorescent protein (cpGFP) (Nagai et al., 2001) (Figure 9.1a). When pre-iGlu and post-Glu expressing neurons form synapses, the two parts of the cpGFP are brought close enough together to partially rejoin and weakly fluoresce (Figure 9.1b). Upon binding of glutamate to the glutamate binding protein in the split-iGluSnFR induces conformation change that restores the beta-barrel of the cpGFP thus increasing the fluorescence intensity (Marvin et al., 2013) (Figure 9.1c). In this way the fluorescent intensity of sensor can be used to detect the concentration of glutamate along the synapse during synaptic release. For the post-iGlu expressed sensor, mRuby3 was expressed using same promoter as the sensor with P2A (2A self-cleaving peptide) (Park et al., 2016) in order to label all post-iGlu expressing cells with mRuby3 (Figure 9.1). To ensure the same cell does not express pre and post sensor, a Cre ON and OFF system was employed where the post-synaptic transgene expression was activated by Cre (DIO “Cre-ON”) and the post-iGluSnFR transgene expression was inactivated by Cre (DO “Cre-Off”) (Saunders et al., 2012).

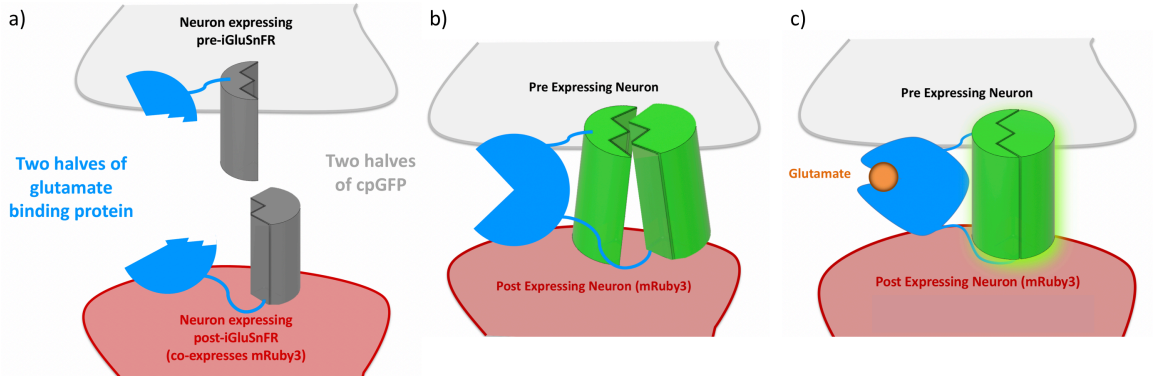

Figure 9.1: Cartoon of split-iGluSnFR parts and synaptic glutamate detection. a) The two parts of the split-iGluSnFR are labeled pre-iGlu and post-iGlu. Each part consisted of the one half of the glutamate binding protein and cpGFP. b) At the synapse, the pre and post parts of the split-iGluSnFR are brought close together, bringing the beta-barrel close enough that it is distorted but able to fluoresce dimly. c) In the presence of glutamate, the glutamate binding protein binds to the glutamate, which induces a conformational change that restores the beta-barrel increasing the fluorescent brightness.

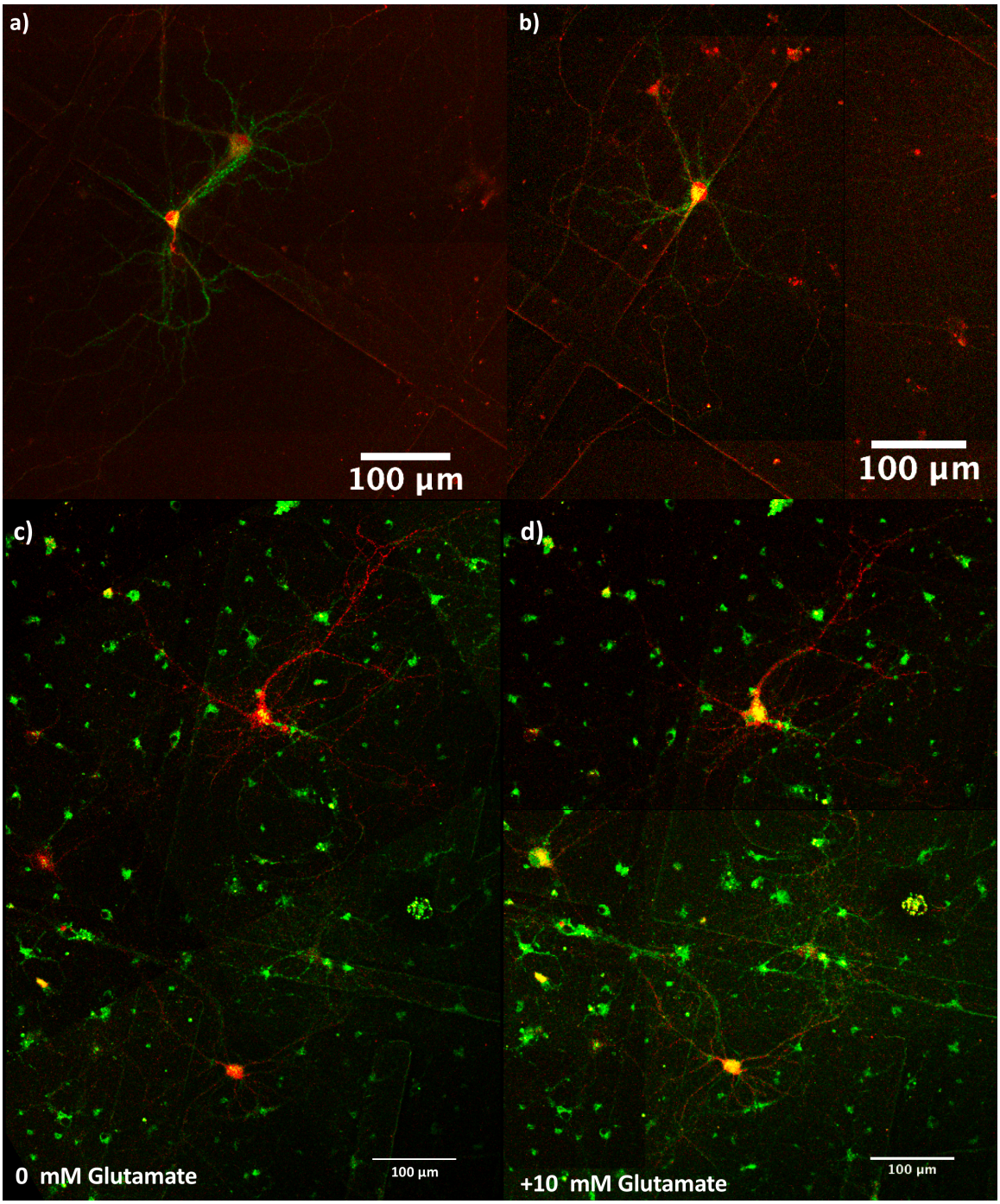

Figure 9.2: Primary hippocampal neurons expressing split-iGluSnFR. Reconstituted synaptic glutamate sensor (consisting of a post-iGlu and pre-iGlu sensor) are shown as green puncta (a-b). Cells expressing the post-synaptic component of the split-iGluSnFR sensor are shown in red. a-b) Primary hippocampal neurons expressing split-iGluSnFR. c) Fluorescence of split-iGluSnFr expressing neurons in media with 0 mM glutamate. d) Reconstituted split-iGluSnFR (green) fluorescent increases with addition of glutamate.

9.3 Microfluidic design to isolate synaptic processes

For initial experiments, commercially available microfluidic devices were used (XONA® Microfluidics) for proof of concept, feasibility, and troubleshooting. Devices were prepared according to manufacturer protocols listed for XonaChip (Taylor, 2019).

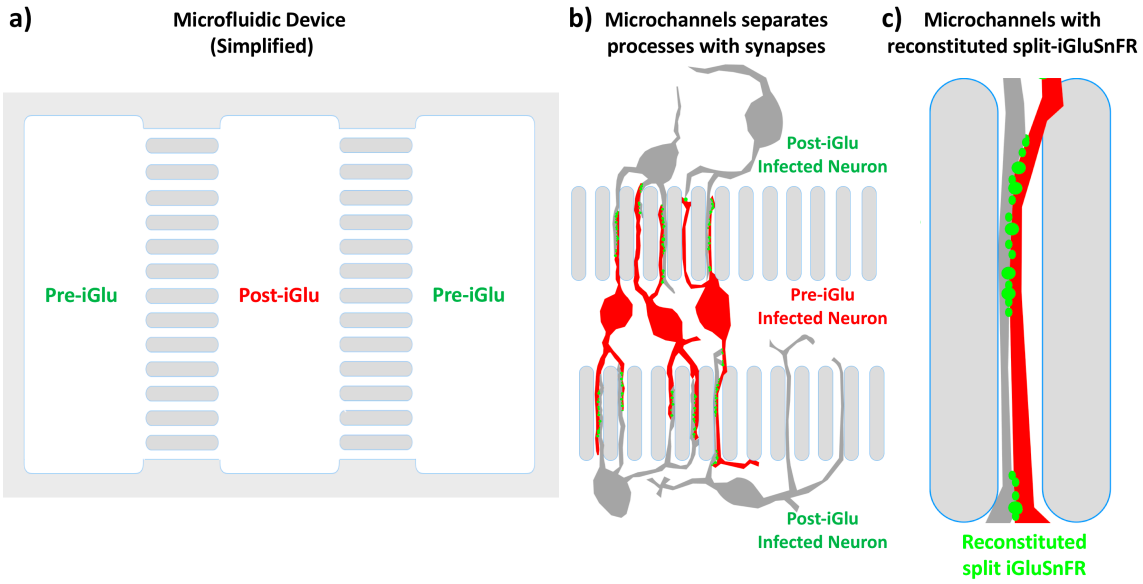

Figure 9.3: Microfluidic design for separating synapses and pre-iGlu and post-iGlu infections. a) Microfluidic device consisting of separate chambers where neurons are infected with either pre-iGlu or post-iGlu sensor. b) Microchannels in device are just wide enough to allow processes to infiltrate and not cell bodies. This allows the synapses to form within microgrooves and be isolated in one part of the device for imaging. c) Along microchannels, reconstituted split-iGluSnFR can be viewed as green puncta.

9.3.1 Fluid isolation in microchannels for compartmental viral infection of pre and post-iGlu components

To transfect chambers with pre-iGlu and post-iGlu components respectively, we needed the microfluidic platform to maintain fluid isolation during viral incubation to separate pre-iGlu and post-iGlu infections. In order to maintain fluid isolation, we employed minute volume differentials between chambers that created a pressure head to isolate fluids into compartments similar to those listed in (Taylor et al., 2005). In this process, high fluid resistance in the microgrooves produce by the compartment with a higher volume creates a

small, sustained flow between compartments that prevents diffusion from the lower volume chamber (Figure 9.4) (Taylor et al., 2003). This volume separation can be maintained for over the course of 24 hours, allowing sufficient time for viral transfection (Figure 9.4).

To demonstrate this fluid isolation across the center part of the device across the microchannels, we loaded the outermost chambers of the device (XONA®, XonaChips® XC-T500) with either calcein AM or Ethidium Homodimer III (EtD-III) stain (Biotium, Viability/Cytotoxicity Assay Kit for Animal Live & Dead Cells, #30002-T) (Figure 9.5). The central chamber was loaded with a higher volume of clear cellular media that prevented the lower volumes of calcein AM (green) and EtD-III (red) dye in the side chambers from leaking into the central chamber (Figure 9.5).

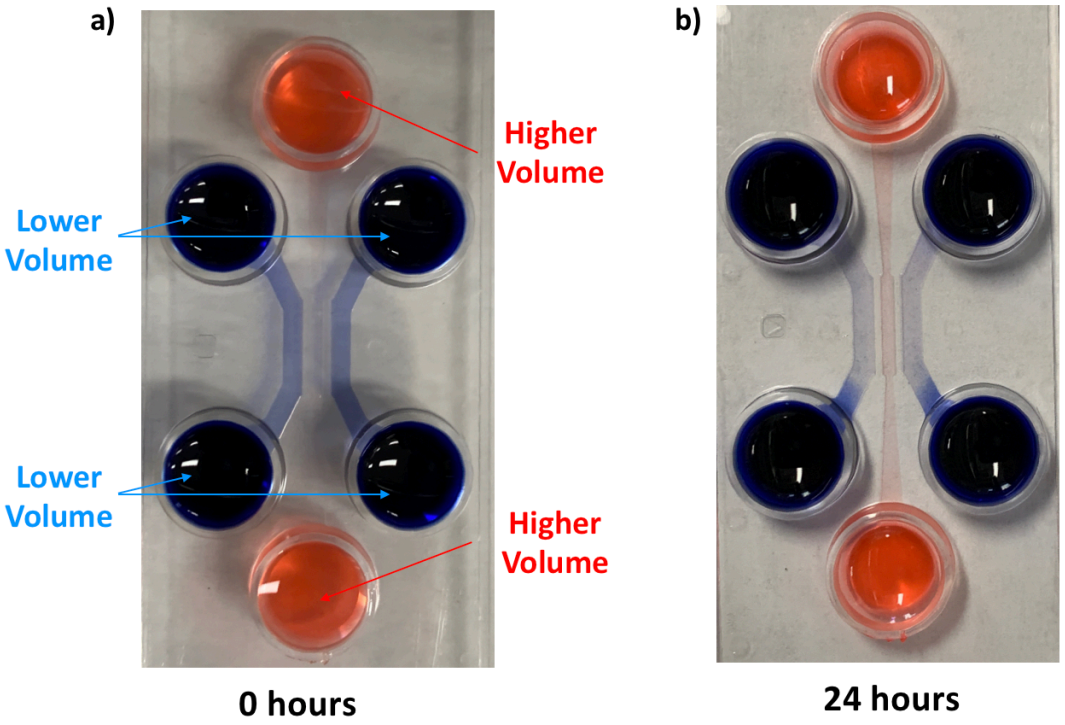

Figure 9.4: Pressure head used to isolate volumes into compartments in microfluidic-based neuron platform. A volume difference between the compartments creates isolation of solutions. A higher volume of solution in the middle chamber (red dye) creates a high fluidic resistance across the microgrooves preventing solution from the side (blue dye) from escaping. Volume difference can be reversed to allow for isolation of solutions to the opposite compartments. Fluid isolation test was demonstrated on XonaChip three-chamber device (XC-T500). a) A higher volume (150 µL) of red dye was added to the middle chamber and lower volume (120 µL) of blue dye to left and right chambers. b) After 24 hours, no dye entered from lower volume chambers (blue) into the middle red chamber indicating successful fluid isolation.

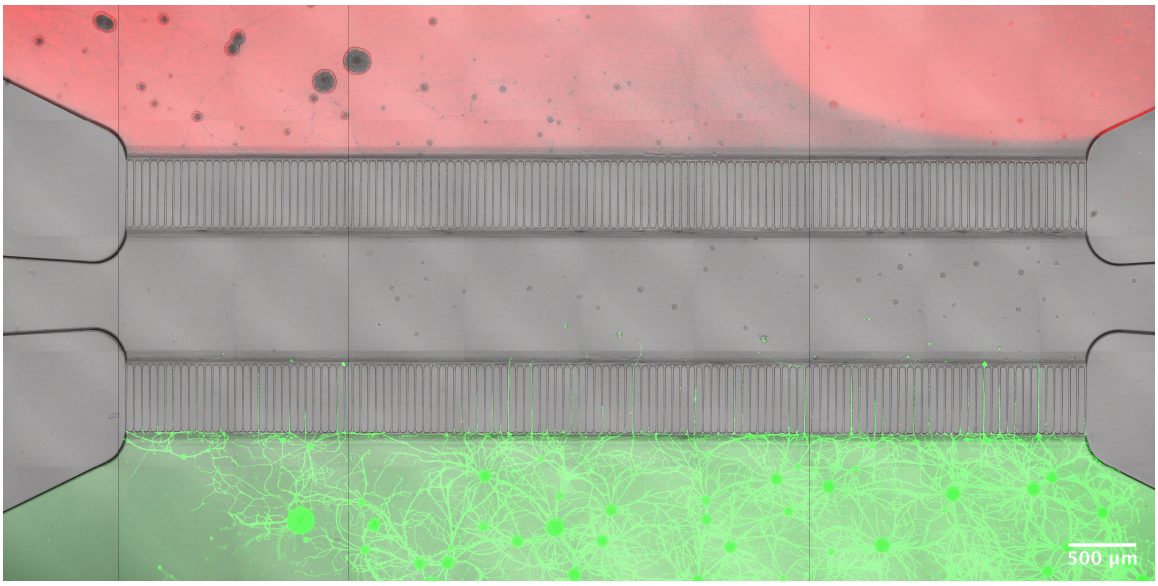

Figure 9.5: Fluid isolation in device. Middle chamber had higher pressure head from a higher volume differential and prevented lower neighboring solutions (red and green) from escaping chambers. The red solution was EtD-III (dead cell stain) and the green solution was calcein AM (a viability stain) that stained viable cells green.

9.3.1.1 Infecting pre-iGlu and post-iGlu expressing neurons into separate compartments

This method of isolating volumes using volume differentials was used to selectively infect neurons in compartments with either pre-iGlu or post-iGlu (Figure 9.6). First, devices were seeded with approximately 90,000 dissociated primary hippocampal neurons (BrainBits, LLC) per chamber (Figure 9.6). After neurons were seeded into chambers and neurons allowed sufficient time to attach to device, the neurons were infected with the split-iGluSnFR packaged in AAV9 capsids. A volume differential between the lower and higher volume compartments was established with a 30 µL volume difference. For longer incubation times, the volume difference was maintained by replenishing media in the higher volume chambers and aspirating out media in the lower volume chambers. For post-iGlu infection, side chambers were loaded with a higher volume of media and the middle chamber was loaded with a lower volume of solution containing post-iGlu AAV. After infection for

24 hours, the virus containing solution was then aspirated and all compartments of the device were then washed with media to remove remaining post-iGlu virus. For pre-iGlu infection, the central chamber was loaded with a higher volume of media and side chambers were loaded with a smaller volume of solution containing pre-iGlu virus and solution was incubated for 24 hours for infection. Finally, the pre-iGlu viral solutions were aspirated out and devices were washed with fresh media. In this way, the central chamber neurons were infected with post-iGlu sensor and side chambers were infected with pre-iGlu sensor. The split-iGlu reporter was allowed 7-14 days to express after viral infection before imaging.

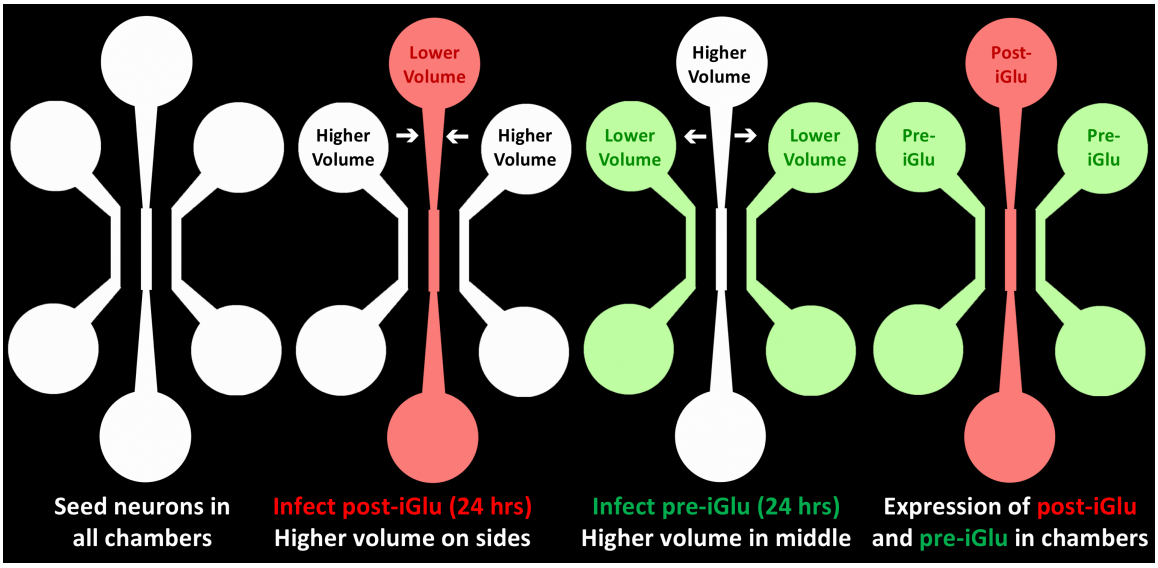

Figure 9.6: Split-iGluSnFR infection strategy in microfluidic devices. Post-iGlu infection chambers are red and pre-iGlu infection chambers are green.

9.3.2 Improving neuron viability in microfluidic devices

9.3.2.1 Reduced evaporation in microfluidic device for improved neuron health

Due to the small volume of media in the devices, it is necessary to reduce evaporation loss to prevent the solution from becoming hyperosmotic, which contributes to the gradual death of neurons in long-term cell cultures (Potter & DeMarse, 2001). To reduce evaporation,

we used a hydrophobic membrane, Teflon® FEP Film (0.5 mil thickness, Durafilm 50A), to seal Petri dishes housing microfluidic devices. This fluorinated ethylene–propylene (FEP) film is selectively permeable, allowing oxygen and carbon dioxide to diffuse but preventing water vapor from escaping (Potter & DeMarse, 2001). To maintain additional humidity and thus reduce humidity fluctuations when the incubator door was opened or when devices were taken out of the incubator, sterile gauze or cotton pads soaked with deionized water were placed into the Petri dish containing the device.

9.3.2.2 Device coating to increase neuron adhesion

Microfluidic devices were prepared according to protocols listed for XonaChips. The device was coated with Poly-D-Lysine (0.5 mg/mL in 0.1 M borate buffer) with a molecular weight of >70,000 kDa (Milipore-Sigma) and was incubated for one to four hours in a humidified, tissue-culture incubator at 37°C (Figure 9.7). Poly-D-Lysine (PDL) is a chemically synthesized extracellular matrix that helps the positively charged cell adhesion molecules to attach and facilitates neuron adhesion to tissue culture-treated plastic and glass surfaces (Harnett et al., 2007). With the shorter PDL treatment time, the neurons clumped together likely due to insufficient PDL adhesion molecules on the microfluidic device surface (Figure 9.7a). Longer PDL treatment times resulted in better attachment of a single neuron layer onto the device surface (Figure 9.7b)

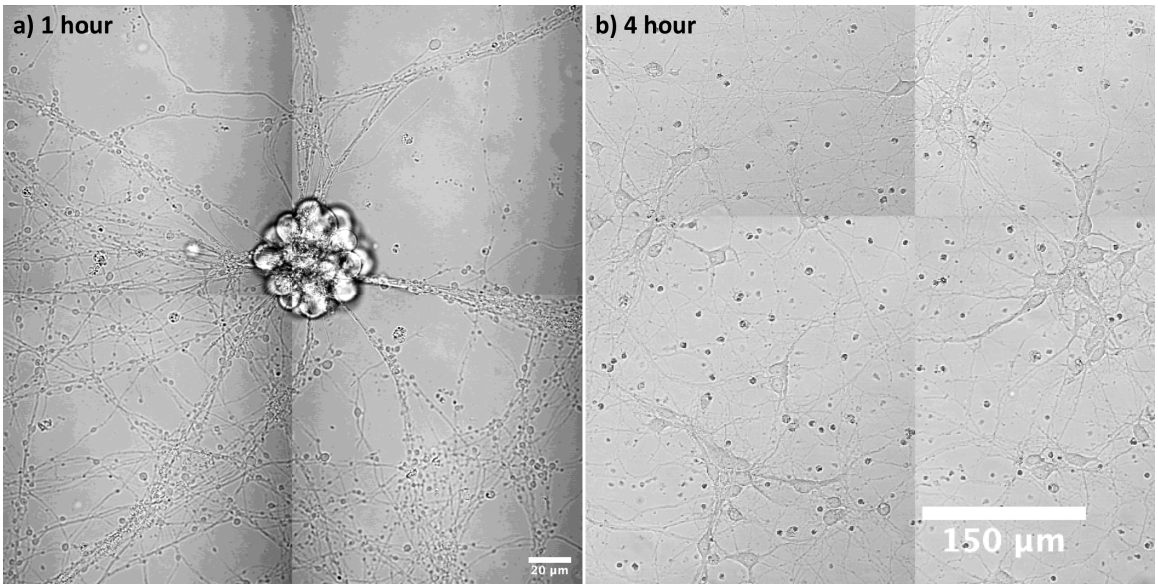

Figure 9.7: Effect of PDL incubation time on neuron adhesion. a) Neuron clumping. b) Single layer neuron growth.

9.3.3 Sparse split-iGluSnFR reconstitution along microchannels

Using microchannels in the microfluidic devices, we successfully observe isolation of the post labeled processes and reconstituted sensors (Figure 9.8). However, reconstitution was sparse likely due to the limited infiltration of neural processes (neurites) in microchannels. This low infiltration of neurites is especially pronounced with the pre-iGlu labeled dendrites as indicated by the low number of reconstituted split-iGluSnFR sensors (green puncta) we observed (Figure 9.8). These factors informed our future microfluidic design where we reduced microchannel length and created a centralized chamber where the microchannels will feed into to allow for more processes to cross (Figure 9.10).

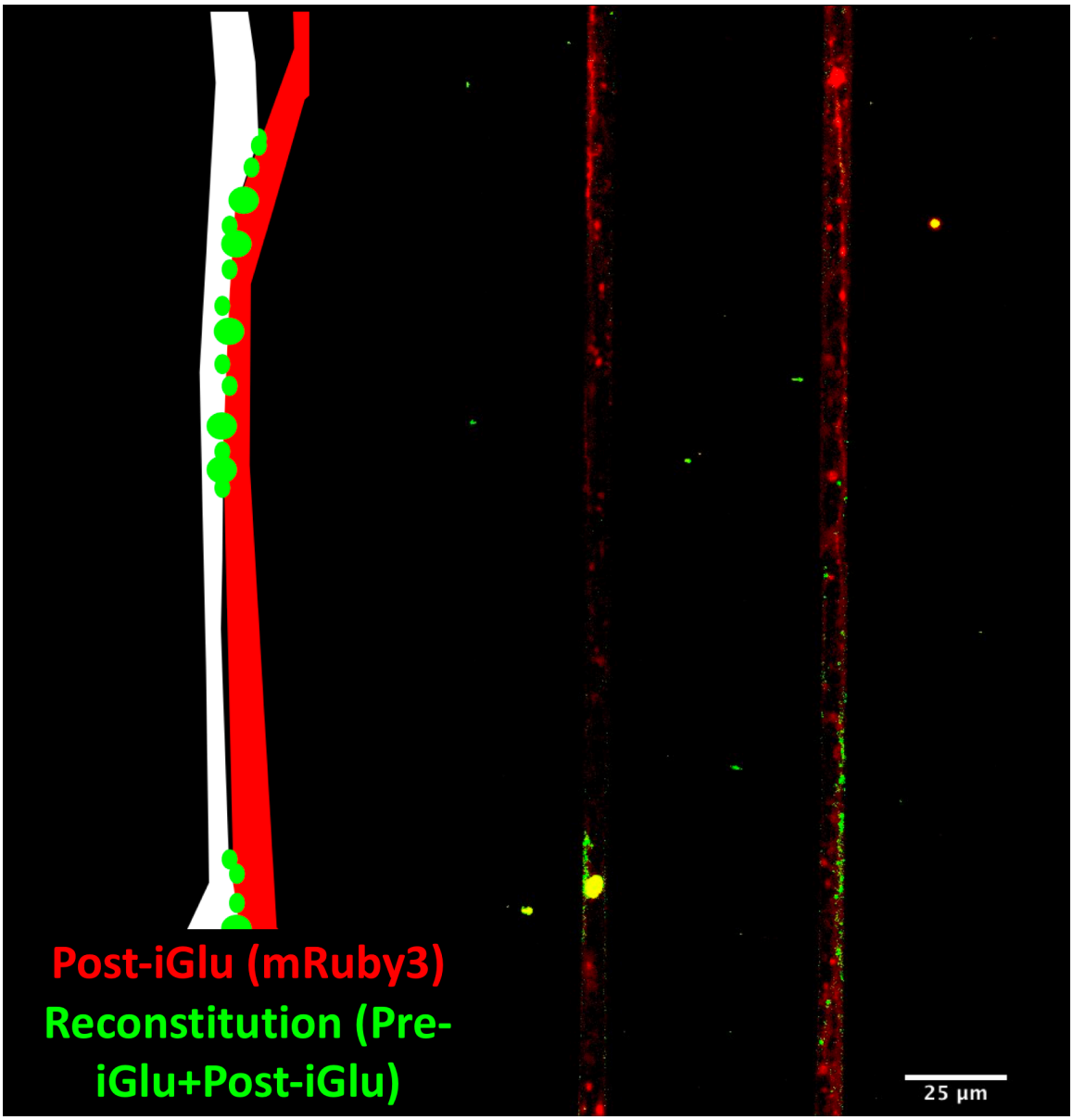

Figure 9.8: Reconstitution along microchannels. Cartoon of neurites captured in microchannels with reconstituted sensor (*left image*). Image of two microchannels with post-iGlu labeled processes (*red*) and reconstituted split-iGlu sensor (*green puncta*) (*right image*). Channels were 500 µm long.

9.3.4 Decreased microchannel length for increased neurite compartmentalization and infiltration

Due to the slow growth and short length of dendrites, it is difficult for the neurites to infiltrate the microchannels. We then tried to increase dendrite infiltration using microfluidic

devices with a shorter microchannel length (shortened to 150 µm from 500 µm) (XONACHIPS®, XC150). With a shorter microchannel length, we observed increased neural process infiltration (Figure 9.9).

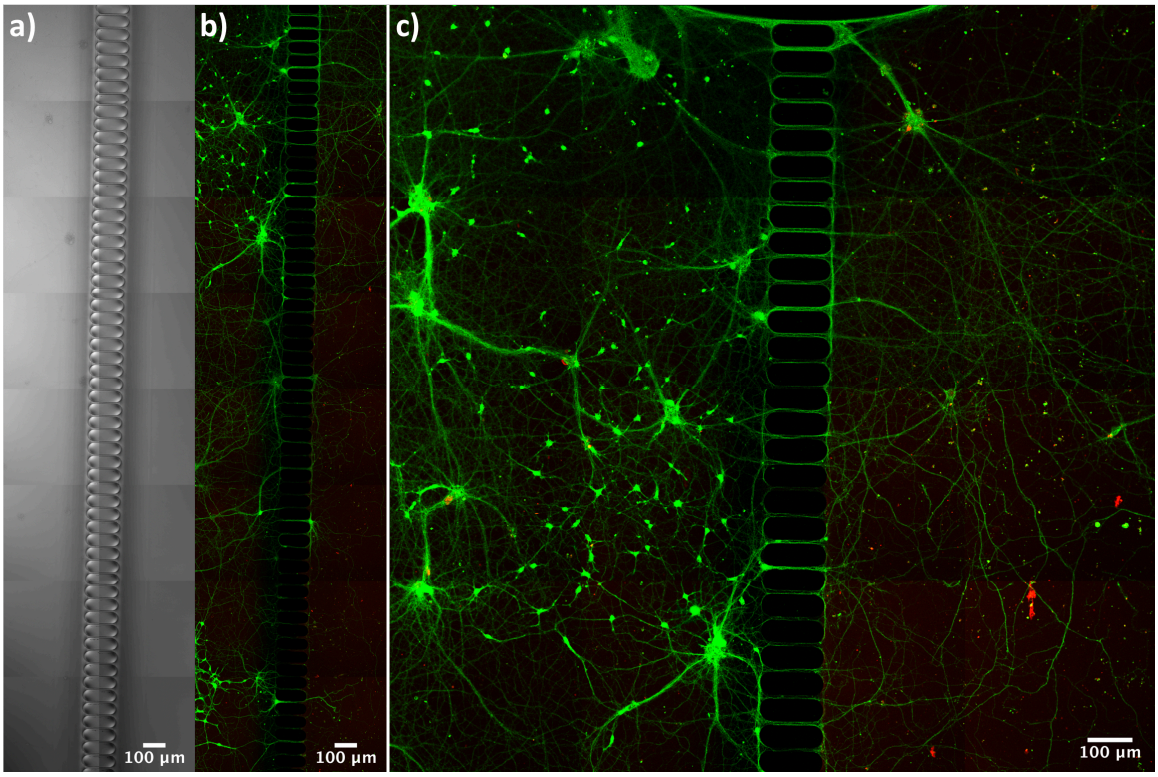

Figure 9.9: Dendrite compartmentalization in microchannels with 150 µm. a) Bright field of device and microchannels. b) Neuron staining with viability (green, calcein AM) and dead (red, EtD-III) cell stain. c) Zoom-in of dendrites infiltrating microchannels.

9.4 New microfluidic design: revised microchannel lengths for axons and dendrites and central chamber for reconstituted synapses and perfusion

To allow for dendrites to fully infiltrate the microchannels, microchannel length was further decreased on one side to 75 µm based on microfluidic devices designed for compartmentalization of dendrites in literature (Cohen et al., 2011). This will allow the pre-iGlu expressing dendrites to fully cross the microchannel and enter the synaptic reconstitution chamber with at least 50% of dendrites in microgrooves longer than 100 µm

(with an average dendrite length of 165 µm long) by 14 days *in vitro* (DIV) (Cohen et al., 2011; Taylor et al., 2010b). On the axonal side, for post-iGlu expressing cells, the channel length was set to 450 µm which is long enough so that most dendrites will not pass the microchannels (Taylor et al., 2010b), and also allow us to isolate the post-iGlu expressing axons in the central reconstitution chamber. The perfusion channel was designed based on microfluidic devices from (Taylor et al., 2010b).

In this new design, neurons will be seeded into rectangular cell chambers 6.5 mm wide and 6.2 mm long (Figure 9.10). For the central synaptic reconstitution chamber, the radius of the inlet is 0.5 mm and the radius of the outlet is 0.32 mm. Microfluidic devices features, materials, and assembly were designed with consideration to the manufacturing capabilities of commercial microfluidic device manufacturing companies (uFluidix).

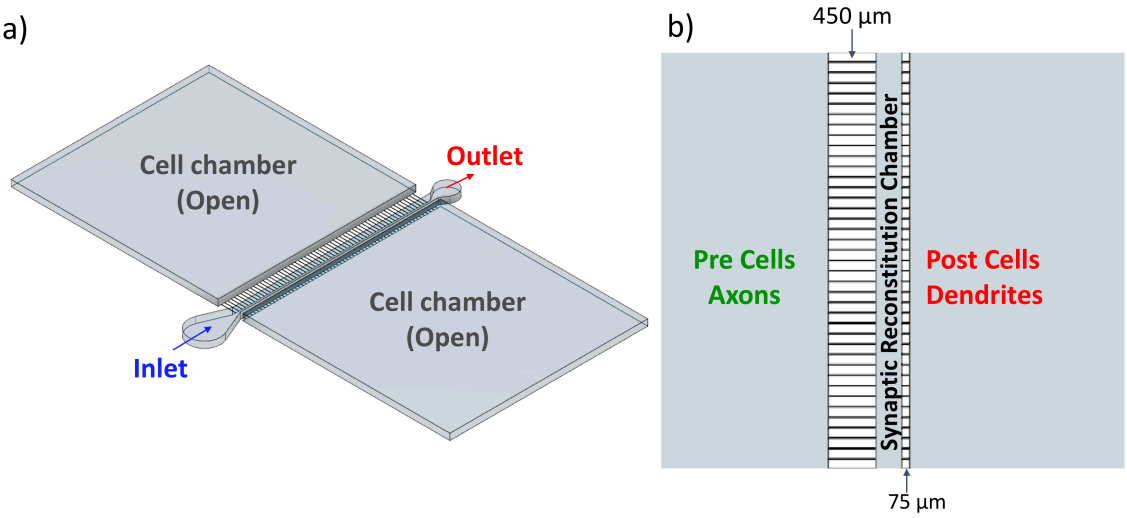

Figure 9.10: Revised microfluidic design. a) Model of microfluidic device. Open cell chambers are created with a biopsy punch. b) Enlarged view of microchannels. Synaptic reconstitution chamber is 250 µm wide.

9.4.1 Simulation of perfusion in microfluidic design

To ensure the device was able to perfuse drugs and analytes through the chambers containing the dendrites with reconstituted synapses, we used the Ansys software with the fluid flow (Fluent) analysis system toolbox to model fluid flow. The model was first imported into Ansys and a mesh was generated of the body approximating the 3D surface of the microfluidic device for simulation (Figure 9.11). ANSYS meshing allows for the geometry of the model to be broken into smaller polygons to be processed and generate simulation results. The input and outlet ports for perfusion were then specified and annotated with the inlet shown in blue with arrows pointing inwards and the outlet shown in red with arrows pointing outwards. To make sure the device did not delaminate during perfusion, we examined the pressure buildup when solution (water) flowed through the inlet and outlet ports in the central chamber (Figure 9.12).

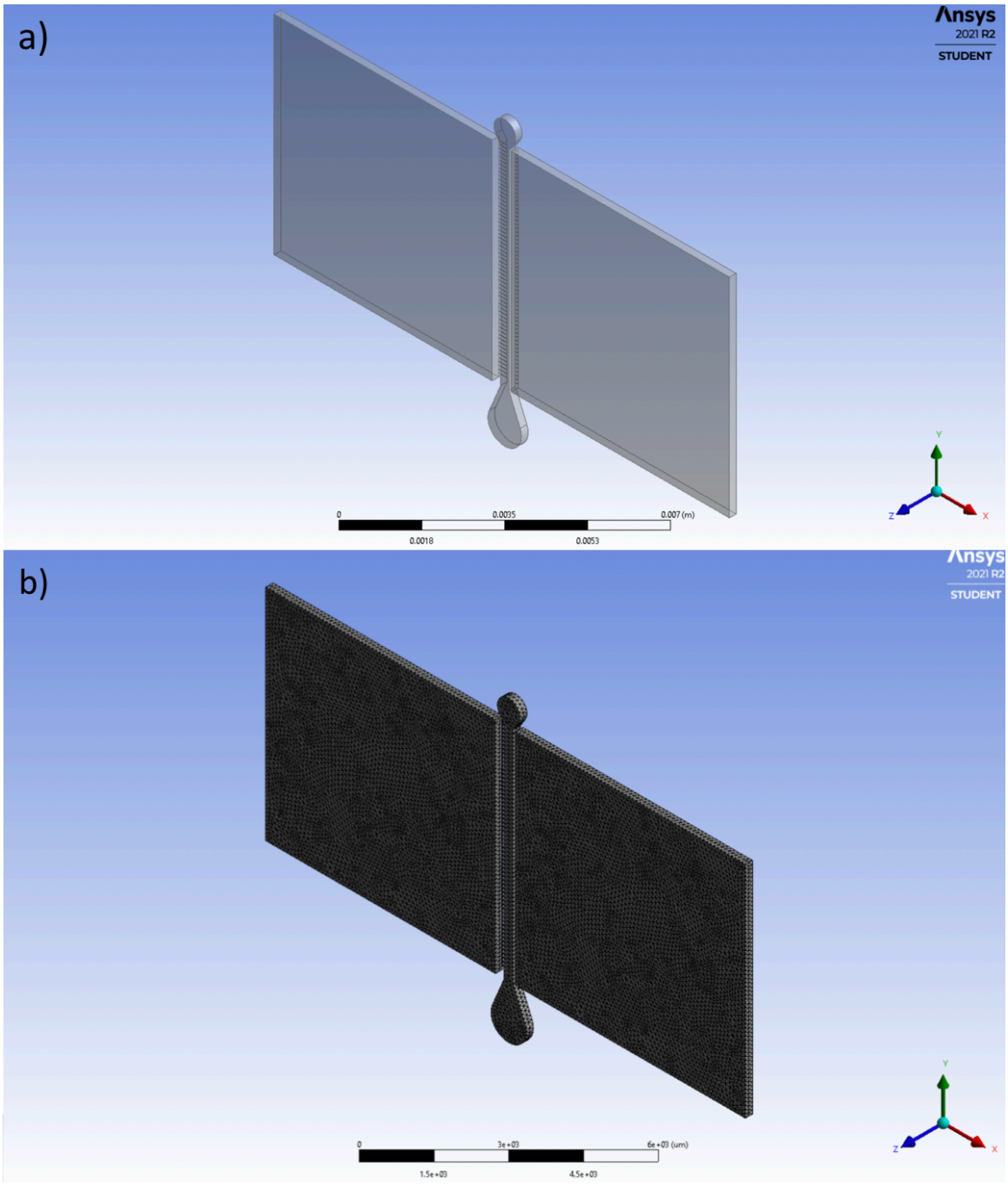

Figure 9.11: Preparing microfluidic device for Ansys simulation. a) Imported geometry of microfluidic design into Ansys program. b) Mesh of microfluidic device generated for simulations.

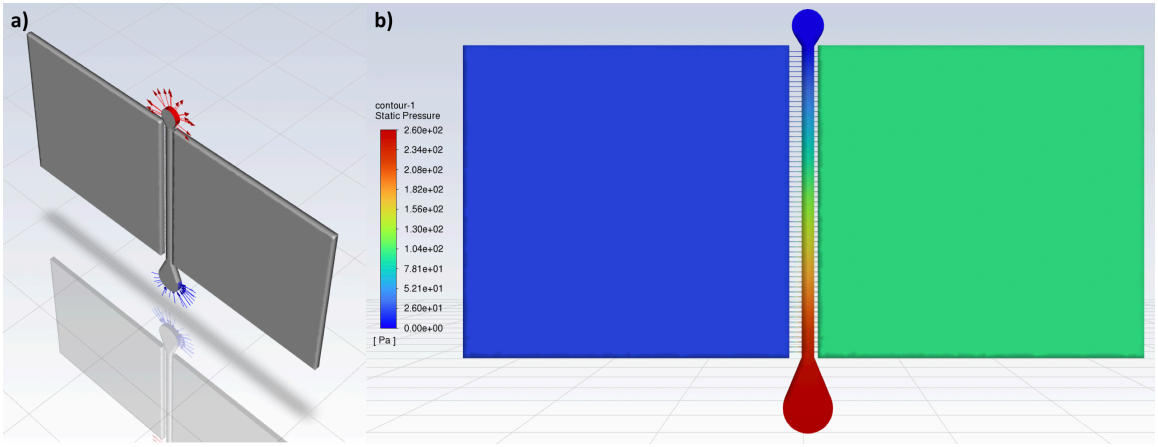

Figure 9.12: Fluid path and pressure simulations. a) Inlet port is annotated with blue arrows pointing inwards. Outlet port is annotated with red arrows radiating outwards. b) Simulation of pressure during perfusion.

9.4.1.1 Particle path predictions using simplified glass, open-surface microfluidic design

Microfluidic design was modified by simplifying inlet and outlet shape, changing the material from PDMS to glass, and creating open-surface compartments. Inlet and outlet shapes were simplified in the model to reduce computational load during particle path simulations. Glass allows for better cell health and cell adhesion compared to PDMS since both the glass and cell membrane are hydrophilic. In contrast, PDMS is hydrophobic and requires treatment to create a hydrophilic layer to allow for attachment of hydrophilic neurons (McDonald et al., 2000). Additionally, uncross linked PDMS oligomers in PDMS-based microfluidic chips can leach into media and are toxic to cell health (Carter et al., 2020).

Open compartments in the device allows for easier solution addition for cell seeding and media change (Lee et al., 2018), a larger liquid-gas interface that allows for more oxygen diffusion to neurons increasing cell viability (Zhao et al., 2011), a simpler fabrication with the elimination of the top bond surface, and better optical transparency because the top side of the device is not covered by material that may autofluorescence during imaging (Young et al., 2013).

Microfluidic devices features, material, and assembly were designed with consideration to the manufacturing capabilities of commercial glass microfluidic device manufacturing companies (Workshop of Photonics). Microchannels for axons were designed with a width of 10 μm, height of 3.5 μm, and length of 250 μm and neuron compartments are approximately 4 mm by 3mm based on (Ristola et al., 2021). The microchannel length for dendrites are 75 μm long based on microfluidic devices designed for compartmentalization of dendrites in literature (Cohen et al., 2011).

The device consisted of two glass parts: a top layer with three chambers with microchannels etched between chambers and a bottom layer consisting of a thin coverslip (Figure 9.13). These two layers were bonded together using laser micro-welding. For the top layer, chambers are formed using a glass micro-cutting laser system (FemtoGLASS, Workshop of Photonics). On one side of the top layer, microchannels (width of 10 μm and height of 3.5 μm) are created by micro-etching the bottom of the device with femtosecond laser ablation (FemtoLAB, Workshop of Photonics). The two layers are then laser welded together (with the microchannels facing the coverslip) which provided a hermetic seal with good mechanical strength between glass pieces.

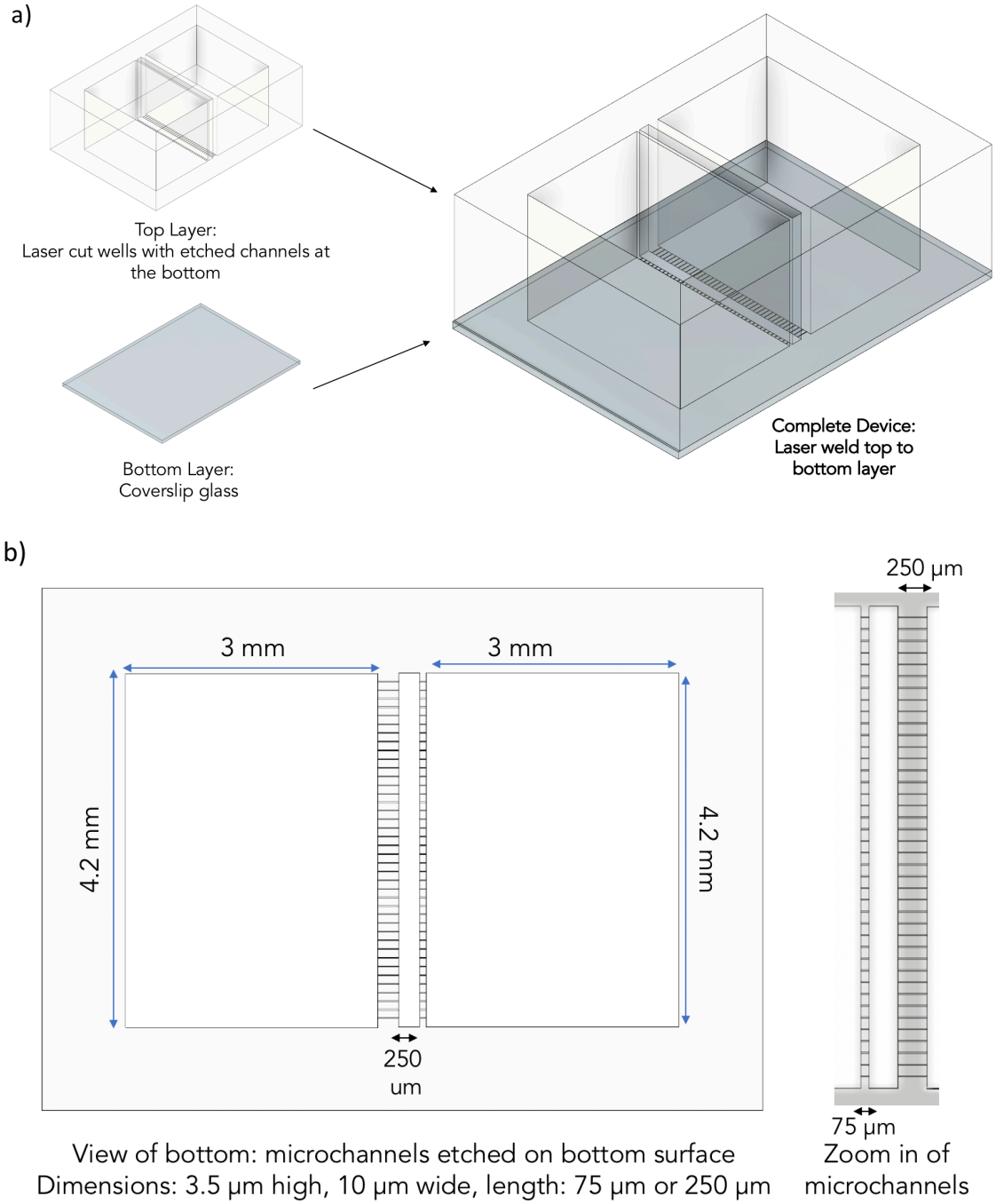

Figure 9.13: Glass microfluidic device with thin coverslip bottom. a) Fabrication and assembly of glass microfluidic device. b) Dimensions of device. Compartment chambers are 1 mm high.

9.4.1.2 Fluid simulations in glass device

Computational fluid dynamics (CFD) simulations were used to predict particle paths and particle velocities during perfusion. The following parameters were used: inlet velocity: 0.1 m/s and initial outlet pressure: 0 Pa. Wall material was set to borosilicate glass and fluid was set to water. Laminar flow through the model was assumed.

9.4.1.3 Particle flow simulation

To simulate the path of the particle through the device, we used the Ansys Fluent to show particle pathlines as solution entered through the inlet and exited via the outlet (Figure 9.14). Particles in the device are used to simulate molecules of analyte (such as glutamate) and their trajectory. The flow of fluid in the device generates different pressure regions that are shown in Figure 9.15.

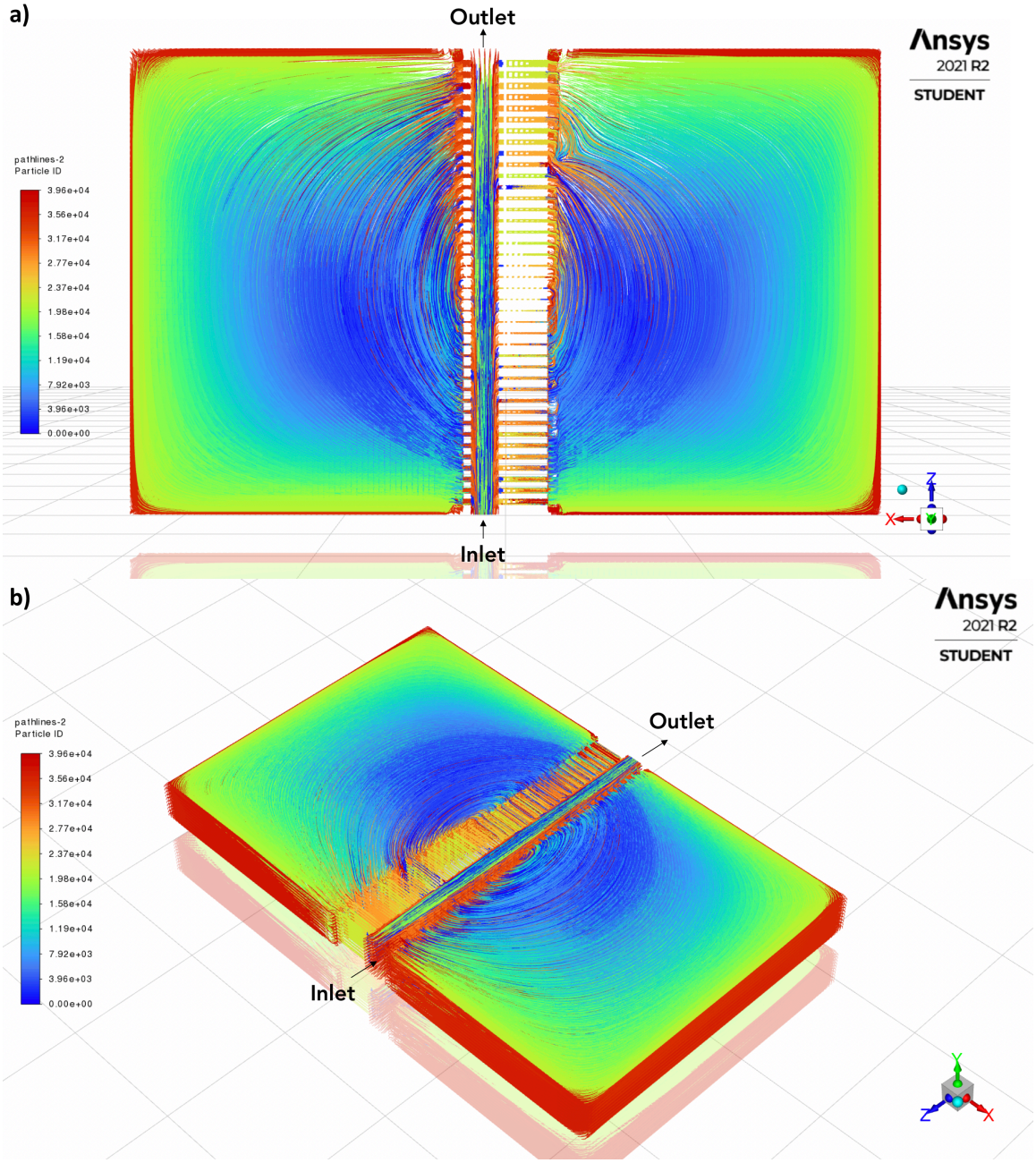

Figure 9.14: Particle flow pathlines in device. a) Top-down view. b) Side view.

From pressure contours models, the highest pressure is at the inlet where the solution enters and lowest pressure at the outlet where the solution exits as expected (Figure 9.15). Since fluid will flow down the path of least resistance, we can confirm the solution will flow primarily from inlet to outlet. Pressure contours are also important in making sure the

pressure does not build up in the device to the point that the layers delaminate. From the models, max absolute pressure in the device is low at 1.01×10^5 Pa (considering atmospheric pressure is 1.01325×10^5 Pa) and thus perfusion would not cause device delamination.

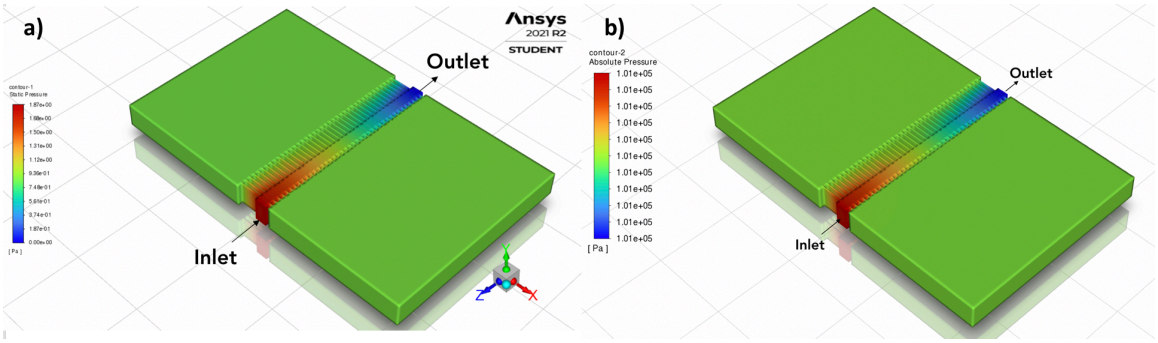

Figure 9.15: Pressure contours in simplified glass model. a) Static pressure. b) Absolute pressure.

9.4.1.4 Velocity of particle pathlines

To determine how long the solution will take to reach areas of the chamber containing synapses, we simulated velocity pathlines when solution was injected through the inlet and removed via the outlet during perfusion (Figure 9.16). Velocity pathlines show that as predicted most particles during perfusion will flow from inlet to outlet. Particles in the center of the central chamber will receive little resistance and thus flow fastest (as shown by red center) so the analyte will reach synapses in the center part of the chamber almost instantaneously. A small number of particles that enter the microchannels flow slowly, mitigating the amount of the perfused solution reaching the side cell chambers.

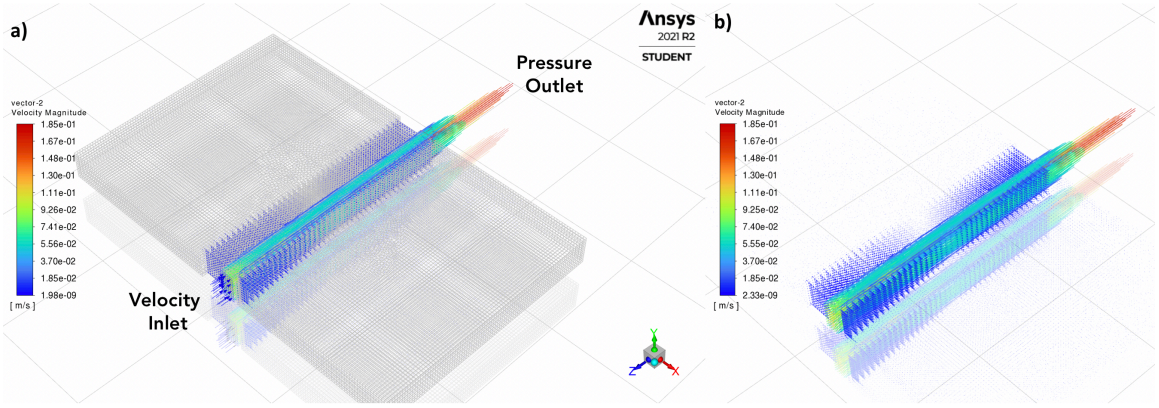

Figure 9.16: Velocity path and magnitude (in m/s) of particles perfused through central reconstitution chamber. a) Outline of device shown with mesh and velocity magnitude of perfused particles color mapped. b) Velocity vectors with device mesh removed.

9.5 Future Directions

Our proposed glass microfluidic device form-factor and materials also allows us to integrate our device with photonic imaging technologies in future studies (Figure 9.17). One area of particular interest is to integrate our microchannel platform with fluorescent contact imagers based on CMOS devices developed in (Takehara et al., 2017). The CMOS chip contains a large number of pixels (Takehara et al., 2017) with pixel size as small as 0.35 μm (Sony, 2021) that can accurately image fluorescent activity across small synaptic boutons that are 0.45-0.55 μm in diameter (Schikorski & Stevens, 1997). Integration with this microfluidic platform with fluorescent CMOS chips provides multiplicity by allowing us to simultaneously record induced glutamate release across the synapse with multiple pixels. The multiplicity of detection with CMOS chips offers advantages over traditional two-photon raster scanning which can only scan a limited area at a time. Use of CMOS chips allows averaging of all the kinetic release events over time to average out noise and increased statically significant measurements of transmitter flux. Using microfluidic devices integrated

with fluorescent CMOS contact imagers, we can better understand and monitor the kinetics of neurotransmitter synaptic release events.

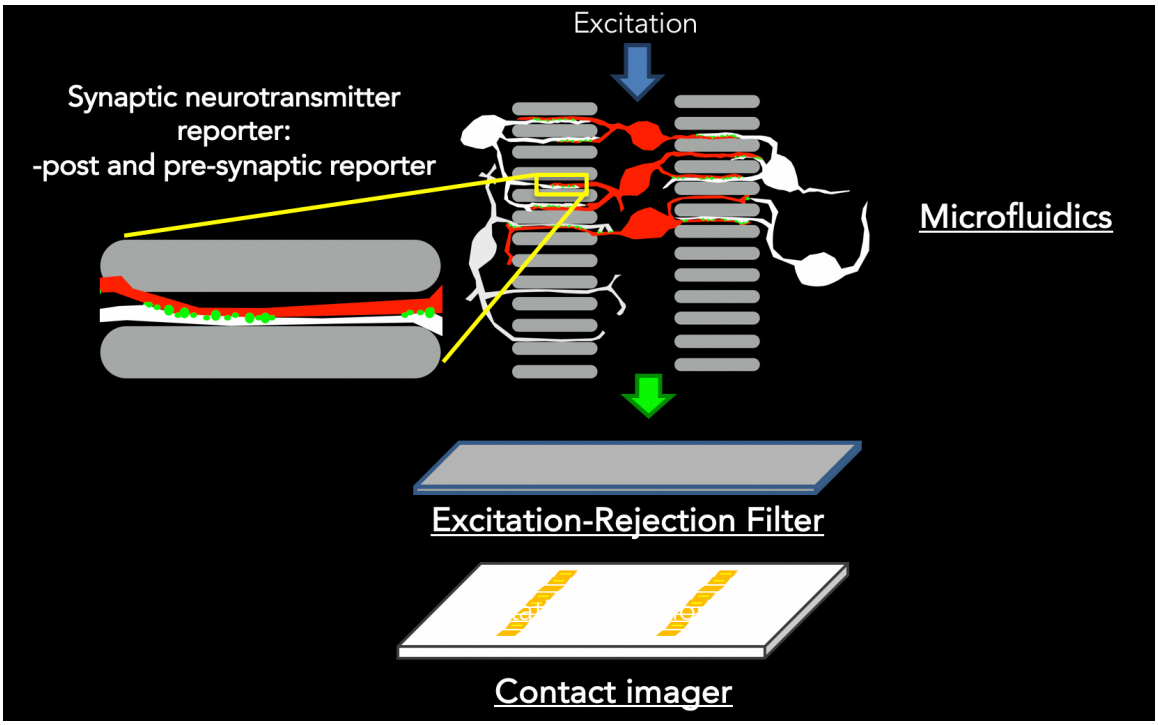

Figure 9.17: Integrated microfluidic platform with CMOS contact imager for monitoring kinetic release of glutamate. Microfluidic platform will consist of microfluidic device described in this chapter. Light from the excitation light will pass through the microfluidic device onto neuron cells expressing the split-iGlu sensor. Emitted fluorescent signal from the reconstituted sensor will then pass through a filter removing the excitation light and the remaining emitted light from the sensor will detected by a fluorescent contact imager. Contact image sensors will be placed along the microchannels or chambers were the processes join to form synapses.

9.6 Conclusion

In conclusion, we establish a microfluidic platform for monitoring synaptic glutamate release with split-iGluSnFR. Using this microfluidic platform, we show successful fluid isolation in microfluidic chambers and infection of pre and post-iGlu parts of split-iGluSnFR reporter. We also confirm successful isolation of neurite processes using microchannels and confirm reconstitution of the split-iGluSnFR along these isolated processes. We also

demonstrate increased infiltration of neural processes with shorter microchannel lengths and propose new microfluidic designs to isolate processes with reconstituted split-iGluSnFR. Using computational fluid dynamic simulations, we model the path and velocity of perfused of analytes through the central chamber. We also simulate the pressure generated during perfusion and demonstrate that the microfluidic device will not delaminate during perfusion. In the future, this microfluidic platform can be integrated with CMOS contact imagers to monitor the kinetics of multiple synaptic release events at one-time point.

Chapter 10

CONCLUSION

The ultimate goals of both projects described in this thesis are to understand the coordinated neural activity and the kinetics of neuronal signaling to develop technologies to enable more comprehensive monitoring of brain activity. The first project focuses on monitoring electrical activity in the brain through extracellular ephys recording and the second project measures chemical activity in the brain via synaptic neurotransmitter release. This thesis describes two separate projects that integrate imaging, one with two-photon imaging with ephys neural probe, and another with microfluidics platforms with contact CMOS imaging. The first project demonstrated the development of a new ultra-dense multisite silicon based neural probes, design, and packaging of 32 and 256-channel assemblies, benchmarking of a minimally invasive, high resolution ephys recordings, and integration of ephys assemblies with two-photon imaging for concurrent imaging of surrounding neurons. Integration with two-photon microscopy allows for simultaneous recording, imaging of probe and the surrounding brain, and control of activity using optogenetic mouse models. We show high-quality ephys recording and concurrent two-photon imaging of the probe and surrounding neurons. We also demonstrate effective silencing of surrounding channelrhodopsin interneuron activity with blue LEDs. To examine synaptic neurotransmitter release, we also establish a microfluidic platform for monitoring synaptic glutamate release with split-iGluSnFR.

10.1 Comparison with previous work

We describe the development of the novel Caltech/LETI probe, with highly dense electrodes and minimally invasive neural probe, packaging for 32-channel acute and 256-channel chronic assemblies, and integration with two-photon setups to allow for simultaneous recording and imaging of probe and the surrounding brain tissue. These assemblies were designed to be compatible with two-photon imaging platforms and allow for concurrent imaging of the probe and brain during ephys recordings. Additionally, the modular design and integration with Intan headstages allows for the active electronics in the headstage board to be thermally decoupled from the probe and flexicables allow for mechanical decoupling of the probe in the brain from the rest of the assembly during chronic behavioral recording.

The neural probes also show better performance compared to other probes by causing less disturbance of surrounding tissue (Chapter 7) and have higher detection of single neuron units (Chapter 6). Also our neural probe has a slightly farther range of detection than other probes (170 μm for our probe compared to 160 μm for the UCLA probe (Du et al., 2011)). We also confirm high quality recordings capable of distinguishing closely spaced neurons of up to of up to 8-25 putative single neuron units per electrode. In particular, our custom neural probes cause less displacement of vasculature blood vessels and capillaries than commercial probes, which cause 49 μm or more displacement for commercial Neuropixel probes (Kozai et al., 2010) compared to our probe's displacement of 30 μm or below. Quantification of displacement was made possible by imaging surrounding vasculature as the probe was inserted with two-photon imaging for the first time.

Several factors contribute to the success of our neural probes compared to other commercial probes, such as the close spacing of the electrodes (pitch of 20 μm comparable to Neuropixel (Steinmetz et al., 2021)), and higher density electrodes of 17.1 electrodes per 100 μm (compared with Neuropixel's 10.1 active electrodes per 100 μm (Steinmetz et al., 2021) or Neuronexus's 11.6 electrodes per 100 μm (Hetke, 2022)). Fabrication of the large number of dense electrode arrays per shank was made possible using integrated circuit technology, which allows for fine resolution and pitch routing necessary to fit large numbers of electrodes on a narrow and thin shank. This dense array of electrodes is especially important because it enhances the ability to triangulate signals from nearby and resolve the activity of closely spaced neurons. The narrow, thin profile of the probe shank is also vital to minimize displacement and damage of the neural tissue during implantation of the neural probe in the brain.

In summary, we describe for the first-time integration of our ephys probes with two-photon setups to allow for simultaneous recording and imaging of probe and the surrounding brain (including stained neurons and blood vessels). We report real-time visualization of neuron apoptosis caused by probe damage and vasculature flow during insertion.

In the second project, we describe development of a microfluidic platform for monitoring synaptic glutamate release with genetically encoded fluorescent reporter, split-iGluSnFR. Using this microfluidic platform, we show successful fluid isolation and infection of pre and post-iGlu parts of the split-iGluSnFR in separate compartments of the device. We also confirm successful isolation of neuron processes and reconstitution of the split-iGluSnFR along these isolated synapses using microchannels. Using shorter microchannels,

we also demonstrate increased infiltration of neural processes. We designed new microfluidic devices to better isolate processes with reconstituted split-iGluSnFR and have a form-factor compatible with existing fluorescent contact imagers. Using computational fluid dynamic simulations, we model the path and velocity of perfused of liquid in the device. In the future, this microfluidic platform can be integrated with CMOS contact imagers to monitor the kinetics of multiple synaptic release events at one-time point in response to different perfused analytes.

10.2 Future Directions

Both platforms described in this project: neural probes paired with two-photon systems and a microfluidic platform paired with fluorescent CMOS arrays, will elucidate important concepts behind neural activity and provide platforms to modulate neural activity. With the two-photon neural probe setup, neural activity in surrounding neurons can be stimulated and measured in a close-looped system. With a microfluidic chip and contact imager, analytes that stimulate synaptic neurotransmitter release are perfused and the resulting neurotransmitter flux can be measured with CMOS arrays. In the future, the two-photon imaging setup reported in this paper can also be paired with state-of-the-art optical neural probes (in place of the ephys probe tested described in this paper), such as plasmonic neural probes with tapered optical fibers (Zheng et al., 2023).

The design philosophy and approach of this thesis combining imaging (either with two-photon microscopy or CMOS arrays) with methods to modulate neuron activity through optogenetic stimulation or perfusion of neuromodulating drugs provide powerful technology platforms for the understanding of coordinated neural activity and the kinetics of neuronal signaling.

BIBLIOGRAPHY

3D Slicer imaging computing platform. (2022). https://www.slicer.org/

Ahrens, J., Brislawn, K., Martin, K., Geveci, B., Law, C. C., & Papka, M. (2001). Large-scale data visualization using parallel data streaming. *IEEE Computer Graphics and Applications*, *21*(4), 34–41. https://doi.org/10.1109/38.933522

Anastassiou, C. A., Perin, R., Buzsáki, G., Markram, H., & Koch, C. (2015). Cell type- and activity-dependent extracellular correlates of intracellular spiking. *Journal of Neurophysiology*, *114*(1), 608–623. https://doi.org/10.1152/jn.00628.2014

Andrasfalvy, B. K., Zemelman, B. V, Tang, J., & Vaziri, A. (2010). Two-photon single-cell optogenetic control of neuronal activity by sculpted light. *Proceedings of the National Academy of Sciences of the United States of America*, *107*(26), 11981–11986. https://doi.org/10.1073/pnas.1006620107

Balaban, R. S., & Hampshire, V. A. (2001). Challenges in small animal noninvasive imaging. *Institute for Laboratory Animal Research Journal*, *42*(3), 248–262. https://doi.org/10.1093/ilar.42.3.248

Belloc, F., Dumain, P., Boisseau, M. R., Jalloustre, C., Reiffers, J., Bernard, P., & Lacombe, F. (1994). A flow cytometric method using Hoechst 33342 and propidium iodide for simultaneous cell cycle analysis and apoptosis determination in unfixed cells. *Cytometry*, *17*(1), 59–65. https://doi.org/10.1002/cyto.990170108

Benes, F. M., & Berretta, S. (2001). GABAergic interneurons: Implications for understanding schizophrenia and bipolar disorder. *Neuropsychopharmacology*, *25*(1), 1–27. https://doi.org/10.1016/S0893-133X(01)00225-1

Blanche, T. J., Spacek, M. A., Hetke, J. F., & Swindale, N. V. (2005). Polytrodes: High-density silicon electrode arrays for large-scale multiunit recording. *Journal of Neurophysiology*, *93*(5), 2987–3000. https://doi.org/10.1152/jn.01023.2004

Buck, K., Voehringer, P., & Ferger, B. (2009). Rapid analysis of GABA and glutamate in microdialysis samples using high performance liquid chromatography and tandem mass spectrometry. *Journal of Neuroscience Methods*, *182*(1), 78–84. https://doi.org/10.1016/j.jneumeth.2009.05.018

Budin, F., Pera, J., & Paniagua, B. (2015). *Documentation/4.6/Extensions/ModelToModelDistance*. https://www.slicer.org/wiki/Documentation/4.6/Extensions/ModelToModelDistance

Bustillo, J. M., Howe, R. T., & Muller, R. S. (1998). Surface micromachining for microelectromechanical systems. *Proceedings of the IEEE*, *86*(8), 1552–1574. https://doi.org/10.1109/5.704260

Buzsáki, G. (2004). Large-scale recording of neuronal ensembles. *Nature Neuroscience*, *7*(5), 446–451. https://doi.org/10.1038/nn1233

Buzsáki, G. (2022). *Head-Fixation RODIN- Rodent Immobilisation- System for Neuroscience*. Cambridge NeuroTech. https://www.cambridgeneurotech.com/head-fixation

Buzsáki, G., Anastassiou, C. A., & Koch, C. (2012). The origin of extracellular fields and currents — EEG, ECoG, LFP and spikes. *Nature Reviews Neuroscience*, *13*(6), 407–420. https://doi.org/10.1038/nrn3241

Buzsáki, G., & Kandel, A. (1998). Somadendritic backpropagation of action potentials in cortical pyramidal cells of the awake rat. *Journal of Neurophysiology*, *79*(3), 1587–1591. https://doi.org/10.1152/jn.1998.79.3.1587

Buzsáki, G., Stark, E., Berényi, A., Khodagholy, D., Kipke, D. R., Yoon, E., & Wise, K. D. (2015). Tools for probing local circuits: High-density silicon probes combined with optogenetics. *Neuron*, *86*(1), 92–105. https://doi.org/10.1016/j.neuron.2015.01.028

Carter, S.-S. D., Atif, A.-R., Kadekar, S., Lanekoff, I., Engqvist, H., Varghese, O. P., Tenje, M., & Mestres, G. (2020). PDMS leaching and its implications for on-chip studies focusing on bone regeneration applications. *Organs-on-a-Chip*, *2*, 100004. https://doi.org/10.1016/j.ooc.2020.100004

Chan, K. Y., Jang, M. J., Yoo, B. B., Greenbaum, A., Ravi, N., Wu, W.-L., Sánchez-Guardado, L., Lois, C., Mazmanian, S. K., Deverman, B. E., & Gradinaru, V. (2017). Engineered AAVs for efficient noninvasive gene delivery to the central and peripheral nervous systems. *Nature Neuroscience*, *20*(8), 1172–1179. https://doi.org/10.1038/nn.4593

Chen, T.-W., Wardill, T. J., Sun, Y., Pulver, S. R., Renninger, S. L., Baohan, A., Schreiter, E. R., Kerr, R. A., Orger, M. B., Jayaraman, V., Looger, L. L., Svoboda, K., & Kim, D. S. (2013). Ultrasensitive fluorescent proteins for imaging neuronal activity. *Nature*, *499*(7458), 295–300. https://doi.org/10.1038/nature12354

Chu, J., & Anderson, S. A. (2015). Development of cortical interneurons. *Neuropsychopharmacology*, *40*(1), 16–23. https://doi.org/10.1038/npp.2014.171

Chung, J. E., Magland, J. F., Barnett, A. H., Tolosa, V. M., Tooker, A. C., Lee, K. Y., Shah, K. G., Felix, S. H., Frank, L. M., & Greengard, L. F. (2017). A fully automated approach to spike sorting. *Neuron*, *95*(6), 1381-1394.e6. https://doi.org/10.1016/j.neuron.2017.08.030

Cohen, M. S., Bas Orth, C., Kim, H. J., Jeon, N. L., & Jaffrey, S. R. (2011). Neurotrophin-mediated dendrite-to-nucleus signaling revealed by microfluidic compartmentalization of dendrites. *Proceedings of the National Academy of Sciences of the United States of America*, *108*(27), 11246–11251. https://doi.org/10.1073/pnas.1012401108

Cortizo, M. C., & De Mele, M. F. L. (2004). Cytotoxicity of copper ions released from metal: Variation with the exposure period and concentration gradients. *Biological Trace Element Research*, *102*(1–3), 129–141. https://doi.org/10.1385/BTER:102:1-3:129

Crone, W. C. (2008). *A Brief Introduction to MEMS and NEMS* (pp. 203–228). https://doi.org/10.1007/978-0-387-30877-7_9

de Cheveigné, A., & Nelken, I. (2019). Filters: When, why, and how (not) to use them. *Neuron*, *102*(2), 280–293. https://doi.org/10.1016/j.neuron.2019.02.039

DeFelipe, J., Alonso-Nanclares, L., & Arellano, J. I. (2002). Microstructure of the neocortex: Comparative aspects. *Journal of Neurocytology*, *31*(3–5), 299–316. https://doi.org/10.1023/a:1024130211265

Denker, M., Roux, S., Timme, M., Riehle, A., & Grün, S. (2007). Phase synchronization between LFP and spiking activity in motor cortex during movement preparation. *Neurocomputing*, *70*(10–12), 2096–2101. https://doi.org/10.1016/j.neucom.2006.10.088

Dreosti, E., Odermatt, B., Dorostkar, M. M., & Lagnado, L. (2009). A genetically encoded reporter of synaptic activity in vivo. *Nature Methods*, *6*(12), 883–889. https://doi.org/10.1038/nmeth.1399

Du, J., Blanche, T. J., Harrison, R. R., Lester, H. A., & Masmanidis, S. C. (2011). Multiplexed, high density electrophysiology with nanofabricated neural probes. *PloS One*, *6*(10), e26204. https://doi.org/10.1371/journal.pone.0026204

Eichenbaum, K. D., Eichenbaum, J. W., Fadiel, A., Miller, D. C., Demir, N., Naftolin, F., Stern, A., & Pevsner, P. H. (2005). Minimally invasive method for murine brain fixation. *BioTechniques*, *39*(4), 487–490. https://doi.org/10.2144/000112003

Fan, J. L., Rivera, J. A., Sun, W., Peterson, J., Haeberle, H., Rubin, S., & Ji, N. (2020). High-speed volumetric two-photon fluorescence imaging of neurovascular dynamics. *Nature Communications*, *11*(1), 6020. https://doi.org/10.1038/s41467-020-19851-1

Fathpour, S., Tsia, K. K., & Jalali, B. (2007). Two-photon photovoltaic effect in silicon. *IEEE Journal of Quantum Electronics*, *43*(12), 1211–1217. https://doi.org/10.1109/JQE.2007.907545

Fazzari, P., Mortimer, N., Yabut, O., Vogt, D., & Pla, R. (2020). Cortical distribution of GABAergic interneurons is determined by migration time and brain size. *Development*. https://doi.org/10.1242/dev.185033

Fedorov, A., Beichel, R., Kalpathy-Cramer, J., Finet, J., Fillion-Robin, J.-C., Pujol, S., Bauer, C., Jennings, D., Fennessy, F., Sonka, M., Buatti, J., Aylward, S., Miller, J. V, Pieper, S., & Kikinis, R. (2012). 3D Slicer as an image computing platform for the Quantitative Imaging Network. *Magnetic Resonance Imaging*, *30*(9), 1323–1341. https://doi.org/10.1016/j.mri.2012.05.001

Feldbauer, K., Zimmermann, D., Pintschovius, V., Spitz, J., Bamann, C., & Bamberg, E. (2009). Channelrhodopsin-2 is a leaky proton pump. *Proceedings of the National Academy of Sciences of the United States of America*, *106*(30), 12317–12322. https://doi.org/10.1073/pnas.0905852106

Ferenczi, E. A., Tan, X., & Huang, C. L. H. (2019). Principles of optogenetic methods and their application to cardiac experimental systems. *Frontiers in Physiology*, *10*. https://doi.org/10.3389/fphys.2019.01096

Fiáth, R., Meszéna, D., Somogyvári, Z., Boda, M., Barthó, P., Ruther, P., & Ulbert, I. (2021). Recording site placement on planar silicon-based probes affects signal quality in acute neuronal recordings. *Scientific Reports*, *11*(1), 2028. https://doi.org/10.1038/s41598-021-81127-5

Filiano, A. J., Gadani, S. P., & Kipnis, J. (2015). Interactions of innate and adaptive immunity in brain development and function. *Brain Research*, *1617*, 18–27. https://doi.org/10.1016/j.brainres.2014.07.050

Foust, K. D., Nurre, E., Montgomery, C. L., Hernandez, A., Chan, C. M., & Kaspar, B. K. (2009). Intravascular AAV9 preferentially targets neonatal neurons and adult astrocytes. *Nature Biotechnology*, *27*(1), 59–65. https://doi.org/10.1038/nbt.1515

Franklin, K., & Paxinos, G. (2008). *The Mouse Brain in Stereotaxic Coordinates* (3rd ed.). Elsevier.

Freeman, J. A., & Nicholson, C. (1975). Experimental optimization of current source-density technique for anuran cerebellum. *Journal of Neurophysiology*, *38*(2), 369–382. https://doi.org/10.1152/jn.1975.38.2.369

Glutamate-Related Biomarkers in Drug Development for Disorders of the Nervous System. (2011). National Academies Press. https://doi.org/10.17226/13146

Gold, C., Henze, D. A., Koch, C., & Buzsáki, G. (2006). On the origin of the extracellular action potential waveform: A modeling study. *Journal of Neurophysiology*, *95*(5), 3113–3128. https://doi.org/10.1152/jn.00979.2005

Golda-Cepa, M., Engvall, K., Hakkarainen, M., & Kotarba, A. (2020). Recent progress on parylene C polymer for biomedical applications: A review. *Progress in Organic Coatings*, *140*, 105493. https://doi.org/10.1016/j.porgcoat.2019.105493

Gray, C. M., Maldonado, P. E., Wilson, M., & McNaughton, B. (1995). Tetrodes markedly improve the reliability and yield of multiple single-unit isolation from multi-unit recordings in cat striate cortex. *Journal of Neuroscience Methods*, *63*(1–2), 43–54. https://doi.org/10.1016/0165-0270(95)00085-2

Groblewski, P. A., Sullivan, D., Lecoq, J., de Vries, S. E. J., Caldejon, S., L'Heureux, Q., Keenan, T., Roll, K., Slaughterback, C., Williford, A., & Farrell, C. (2020). A standardized head-fixation system for performing large-scale, in vivo physiological recordings in mice. *Journal of Neuroscience Methods*, *346*, 108922. https://doi.org/10.1016/j.jneumeth.2020.108922

Groothuis, D. R., Ward, S., Schlageter, K. E., C. Itskovich, A., Schwerin, S. C., Allen, C. V, Dills, C., & M. Levy, R. (1998). Changes in blood-brain barrier permeability associated with insertion of brain cannulas and microdialysis probes. *Brain Research*, *803*(1–2), 218–230. https://doi.org/10.1016/S0006-8993(98)00572-1

Güttler, G., & Queisser, H. J. (1969). Photovoltaic effect of gold in silicon. *Journal of Applied Physics*, *40*(12), 4994–4995. https://doi.org/10.1063/1.1657337

Harnett, E. M., Alderman, J., & Wood, T. (2007). The surface energy of various biomaterials coated with adhesion molecules used in cell culture. *Colloids and Surfaces B: Biointerfaces*, *55*(1), 90–97. https://doi.org/10.1016/j.colsurfb.2006.11.021

Harrison, R. R., & Charles, C. (2003). A low-power low-noise cmos for amplifier neural recording applications. *IEEE Journal of Solid-State Circuits*, *38*(6), 958–965. https://doi.org/10.1109/JSSC.2003.811979

Helmchen, F., & Denk, W. (2005). Deep tissue two-photon microscopy. *Nature Methods*, *2*(12), 932–940. https://doi.org/10.1038/nmeth818

Henze, D. A., Borhegyi, Z., Csicsvari, J., Mamiya, A., Harris, K. D., & Buzsáki, G. (2000). Intracellular features predicted by extracellular recordings in the hippocampus in vivo. *Journal of Neurophysiology*, *84*(1), 390–400. https://doi.org/10.1152/jn.2000.84.1.390

Herculano-Houzel, S., Watson, C., & Paxinos, G. (2013). Distribution of neurons in functional areas of the mouse cerebral cortex reveals quantitatively different cortical zones. *Frontiers in Neuroanatomy*, *7*. https://doi.org/10.3389/fnana.2013.00035

Hetke, J. F. (2022). *NeuroNexus 2022 Microelectrode Design*. NeuroNexus. https://www.neuronexus.com/wp-content/uploads/2022/03/NeuroNexus-2022-Microelectrode-Arrays-Design-Catalog.pdf

Holmgren, C., Harkany, T., Svennenfors, B., & Zilberter, Y. (2003). Pyramidal cell communication within local networks in layer 2/3 of rat neocortex. *The Journal of Physiology*, *551*(1), 139–153. https://doi.org/10.1113/jphysiol.2003.044784

Hong, G., & Lieber, C. M. (2019). Novel electrode technologies for neural recordings. *Nature Reviews Neuroscience*, *20*(6), 330–345. https://doi.org/10.1038/s41583-019-0140-6

Hopcroft, M. A., Nix, W. D., & Kenny, T. W. (2010). What is the Young's modulus of silicon? *Journal of Microelectromechanical Systems*, *19*(2), 229–238. https://doi.org/10.1109/JMEMS.2009.2039697

Hoshino, C., Konno, A., Hosoi, N., Kaneko, R., Mukai, R., Nakai, J., & Hirai, H. (2021). GABAergic neuron-specific whole-brain transduction by AAV-PHP.B incorporated with a new GAD65 promoter. *Molecular Brain*, *14*(1), 33. https://doi.org/10.1186/s13041-021-00746-1

Hulse, B. K., Moreaux, L. C., Lubenov, E. V., & Siapas, A. G. (2016). Membrane potential dynamics of CA1 pyramidal neurons during hippocampal ripples in awake mice. *Neuron*, *89*(4), 800–813. https://doi.org/10.1016/j.neuron.2016.01.014

Jaquins-Gerstl, A., & Michael, A. C. (2020). Dexamethasone-enhanced microdialysis and penetration injury. *Frontiers in Bioengineering and Biotechnology*, *8*. https://doi.org/10.3389/fbioe.2020.602266

Jensen, K. H. R., & Berg, R. W. (2016). CLARITY-compatible lipophilic dyes for electrode marking and neuronal tracing. *Scientific Reports*, *6*(1), 32674. https://doi.org/10.1038/srep32674

Jensen, W., Yoshida, K., & Hofmann, U. G. (2006). In-vivo implant mechanics of flexible, silicon-based ACREO microelectrode arrays in rat cerebral cortex. *IEEE Transactions on Biomedical Engineering*, *53*(5), 934–940. https://doi.org/10.1109/TBME.2006.872824

Johnson, M. D., Kao, O. E., & Kipke, D. R. (2007). Spatiotemporal pH dynamics following insertion of neural microelectrode arrays. *Journal of Neuroscience Methods*, *160*(2), 276–287. https://doi.org/10.1016/j.jneumeth.2006.09.023

Juavinett, A. L., Bekheet, G., & Churchland, A. K. (2019). Chronically implanted neuropixels probes enable high-yield recordings in freely moving mice. *ELife*, *8*. https://doi.org/10.7554/eLife.47188

Jun, J. J., Steinmetz, N. A., Siegle, J. H., Denman, D. J., Bauza, M., Barbarits, B., Lee, A. K., Anastassiou, C. A., Andrei, A., Aydın, Ç., Barbic, M., Blanche, T. J., Bonin, V., Couto, J., Dutta, B., Gratiy, S. L., Gutnisky, D. A., Häusser, M., Karsh, B., … Harris, T. D. (2017). Fully integrated silicon probes for high-density recording of neural activity. *Nature*, *551*(7679), 232–236. https://doi.org/10.1038/nature24636

Keller, D., Erö, C., & Markram, H. (2018). Cell densities in the mouse brain: A systematic review. *Frontiers in Neuroanatomy*, *12*. https://doi.org/10.3389/fnana.2018.00083

Kepecs, A., & Fishell, G. (2014). Interneuron cell types are fit to function. *Nature*, *505*(7483), 318–326. https://doi.org/10.1038/nature12983

Kipke, D. R., Shain, W., Buzsáki, G., Fetz, E., Henderson, J. M., Hetke, J. F., & Schalk, G. (2008). Advanced neurotechnologies for chronic neural interfaces: New horizons and clinical opportunities. *Journal of Neuroscience*, *28*(46), 11830–11838. https://doi.org/10.1523/JNEUROSCI.3879-08.2008

Knodel, M. M., Geiger, R., Ge, L., Bucher, D., Grillo, A., Wittum, G., Schuster, C. M., & Queisser, G. (2014). Synaptic bouton properties are tuned to best fit the prevailing firing pattern. *Frontiers in Computational Neuroscience*, *8*(September). https://doi.org/10.3389/fncom.2014.00101

Kozai, T D Y, Marzullo, T. C., Hooi, F., Langhals, N. B., Majewska, A. K., Brown, E. B., & Kipke, D. R. (2010). Reduction of neurovascular damage resulting from microelectrode insertion into the cerebral cortex using in vivo two-photon mapping. *Journal of Neural Engineering*, *7*(4), 046011. https://doi.org/10.1088/1741-2560/7/4/046011

Kozai, Takashi D Yoshida, Vazquez, A. L., Weaver, C. L., Kim, S.-G., & Cui, X. T. (2012). In vivo two-photon microscopy reveals immediate microglial reaction to implantation of microelectrode through extension of processes. *Journal of Neural Engineering*, *9*(6), 066001. https://doi.org/10.1088/1741-2560/9/6/066001

Lee, H., Bellamkonda, R. V, Sun, W., & Levenston, M. E. (2005). Biomechanical analysis of silicon microelectrode-induced strain in the brain. *Journal of Neural Engineering*, *2*(4), 81–89. https://doi.org/10.1088/1741-2560/2/4/003

Lee, J. J., Berthier, J., Brakke, K. A., Dostie, A. M., Theberge, A. B., & Berthier, E. (2018). Droplet behavior in open biphasic microfluidics. *Langmuir*, *34*(18), 5358–5366. https://doi.org/10.1021/acs.langmuir.8b00380

Lin, C.-H. (2008). Bulk micromachining. In *Encyclopedia of Microfluidics and Nanofluidics* (pp. 164–173). Springer US. https://doi.org/10.1007/978-0-387-48998-8_138

Lin, J. Y. (2012). Optogenetic excitation of neurons with channelrhodopsins. Light instrumentation, expression systems, and channelrhodopsin variants. In *Progress in Brain Research* (Vol. 196, pp. 29–47). https://doi.org/10.1016/B978-0-444-59426-6.00002-1

Liu, X., Chen, H., Wang, Y., Si, Y., Zhang, H., Li, X., Zhang, Z., Yan, B., Jiang, S., Wang, F., Weng, S., Xu, W., Zhao, D., Zhang, J., & Zhang, F. (2021). Near-infrared manipulation of multiple neuronal populations via trichromatic upconversion. *Nature Communications*, *12*(1), 5662. https://doi.org/10.1038/s41467-021-25993-7

Loeb, G. E., Bak, M. J., Schmidt, E. M., & Salcman, M. (1977). Parylene as a chronically stable, reproducible microelectrode insulator. *IEEE Transactions on Biomedical Engineering*, *BME-24*(2), 121–128. https://doi.org/10.1109/TBME.1977.326115

Lojek, B. (2007). *History of Semiconductor Engineering*. Springer Berlin Heidelberg. https://doi.org/10.1007/978-3-540-34258-8

Luan, L., Wei, X., Zhao, Z., Siegel, J. J., Potnis, O., Tuppen, C. A., Lin, S., Kazmi, S., Fowler, R. A., Holloway, S., Dunn, A. K., Chitwood, R. A., & Xie, C. (2017). Ultraflexible nanoelectronic probes form reliable, glial scar–free neural integration. *Science Advances*, *3*(2). https://doi.org/10.1126/sciadv.1601966

Marvin, J. S., Borghuis, B. G., Tian, L., Cichon, J., Harnett, M. T., Akerboom, J., Gordus, A., Renninger, S. L., Chen, T.-W., Bargmann, C. I., Orger, M. B., Schreiter, E. R., Demb, J. B., Gan, W.-B., Hires, S. A., & Looger, L. L. (2013). An optimized fluorescent probe for visualizing glutamate neurotransmission. *Nature Methods*, *10*(2), 162–170. https://doi.org/10.1038/nmeth.2333

Masmanidis, S. (n.d.). *Microprobe Info*. Retrieved December 2, 2022, from https://masmanidislab.neurobio.ucla.edu/images/microprobe_info.pdf

Mathiesen, S. N., Lock, J. L., Schoderboeck, L., Abraham, W. C., & Hughes, S. M. (2020). CNS transduction benefits of AAV-PHP.eB over AAV9 are dependent on administration route and mouse strain. *Molecular Therapy - Methods and Clinical Development*, *19*, 447–458. https://doi.org/10.1016/j.omtm.2020.10.011

McDonald, J. C., Duffy, D. C., Anderson, J. R., Chiu, D. T., Wu, H., Schueller, O. J., & Whitesides, G. M. (2000). Fabrication of microfluidic systems in poly(dimethylsiloxane). *Electrophoresis*, *21*(1), 27–40. https://doi.org/10.1002/(SICI)1522-2683(20000101)21:1<27::AID-ELPS27>3.0.CO;2-C

McEntee, W. J., & Crook, T. H. (1993). Glutamate: Its role in learning, memory, and the aging brain. *Psychopharmacology*, *111*(4), 391–401. https://doi.org/10.1007/BF02253527

McGlynn, E., Nabaei, V., Ren, E., Galeote-Checa, G., Das, R., Curia, G., & Heidari, H. (2021). The future of neuroscience: Flexible and wireless implantable neural electronics. *Advanced Science*, *8*(10), 2002693. https://doi.org/10.1002/advs.202002693

Meldrum, B. S. (2000). Glutamate as a neurotransmitter in the brain: Review of physiology and pathology. *The Journal of Nutrition*, *130*(4), 1007S-1015S. https://doi.org/10.1093/jn/130.4.1007S

Michalikova, M., Remme, M. W. H., & Kempter, R. (2018). Extracellular waveforms reveal an axonal origin of spikelets in pyramidal neurons. *Journal of Neurophysiology*, *120*(4), 1484–1495. https://doi.org/10.1152/jn.00463.2017

Mittmann, W., Wallace, D. J., Czubayko, U., Herb, J. T., Schaefer, A. T., Looger, L. L., Denk, W., & Kerr, J. N. D. (2011). Two-photon calcium imaging of evoked activity from L5 somatosensory neurons in vivo. *Nature Neuroscience*, *14*(8), 1089–1093. https://doi.org/10.1038/nn.2879

Mohanty, S. K., Reinscheid, R. K., Liu, X., Okamura, N., Krasieva, T. B., & Berns, M. W. (2008). In-depth activation of channelrhodopsin 2-sensitized excitable cells with high spatial resolution using two-photon excitation with a near-infrared laser microbeam. *Biophysical Journal*, *95*(8), 3916–3926. https://doi.org/10.1529/biophysj.108.130187

Moldovan, N., Blaga, I.-I., Billa, S., Hossain, I., Gong, C., Jones, C. E., Murray, T. A., Divan, R., Siddiqui, S., & Arumugam, P. U. (2021). Brain-implantable multifunctional probe for simultaneous detection of glutamate and GABA neurotransmitters. *Sensors and Actuators B: Chemical*, *337*, 129795. https://doi.org/10.1016/j.snb.2021.129795

Moreaux, L. (2007). Estimating firing rates from calcium signals in locust projection neurons in vivo. *Frontiers in Neural Circuits*, *1*. https://doi.org/10.3389/neuro.04.002.2007

Moreaux, L., & Laurent, G. (2008). A simple method to reconstruct firing rates from dendritic calcium signals. *Frontiers in Neuroscience*, *2*(2), 176–185. https://doi.org/10.3389/neuro.01.032.2008

Moreaux, L., Yatsenko, D., Sacher, W. D., Choi, J., Lee, C., Kubat, N. J., Cotton, R. J., Boyden, E. S., Lin, M. Z., Tian, L., Tolias, A. S., Poon, J. K. S., Shepard, K. L., & Roukes, M. L. (2020). Integrated neurophotonics: Toward dense volumetric interrogation of brain circuit activity—at Depth and in Real Time. *Neuron*, *108*(1), 66–92. https://doi.org/10.1016/j.neuron.2020.09.043

Musk, E. (2019). An integrated brain-machine interface platform with thousands of channels. *Journal of Medical Internet Research*, *21*(10), e16194. https://doi.org/10.2196/16194

Nagai, T., Sawano, A., Park, E. S., & Miyawaki, A. (2001). Circularly permuted green fluorescent proteins engineered to sense Ca 2+. *Proceedings of the National Academy of Sciences*, *98*(6), 3197–3202. https://doi.org/10.1073/pnas.051636098

Nagel, G., Szellas, T., Huhn, W., Kateriya, S., Adeishvili, N., Berthold, P., Ollig, D., Hegemann, P., & Bamberg, E. (2003). Channelrhodopsin-2, a directly light-gated cation-selective membrane channel. *Proceedings of the National Academy of Sciences*, *100*(24), 13940–13945. https://doi.org/10.1073/pnas.1936192100

Najafi, K., Ji, J., & Wise, K. D. (1990). Scaling limitations of silicon multichannel recording probes. *IEEE Transactions on Biomedical Engineering*, *37*(1), 1–11. https://doi.org/10.1109/10.43605

Neto, J. P., Lopes, G., Frazão, J., Nogueira, J., Lacerda, P., Baião, P., Aarts, A., Andrei, A., Musa, S., Fortunato, E., Barquinha, P., & Kampff, A. R. (2016). Validating silicon polytrodes with paired juxtacellular recordings: method and dataset. *Journal of Neurophysiology*, *116*(2), 892–903. https://doi.org/10.1152/jn.00103.2016

Oliva, A. A., Jiang, M., Lam, T., Smith, K. L., & Swann, J. W. (2000). Novel hippocampal interneuronal subtypes identified using transgenic mice that express green fluorescent protein in GABAergic interneurons. *Journal of Neuroscience*, *20*(9), 3354–3368. https://doi.org/10.1523/jneurosci.20-09-03354.2000

Pachitariu, M. (2020). *More on drift correction*. https://github.com/MouseLand/Kilosort/wiki/3.-More-on-drift-correction

Pachitariu, M., Steinmetz, N., Kadir, S., Carandini, M., & Kenneth D., H. (2016). Kilosort: Realtime spike-sorting for extracellular electrophysiology with hundreds of channels. *BioRxiv*, 61481. https://doi.org/10.1101/061481

Packer, A. M., Roska, B., & Häusser, M. (2013). Targeting neurons and photons for optogenetics. *Nature Neuroscience*, *16*(7), 805–815. https://doi.org/10.1038/nn.3427

Pak, N., Siegle, J. H., Kinney, J. P., Denman, D. J., Blanche, T. J., & Boyden, E. S. (2015). Closed-loop, ultraprecise, automated craniotomies. *Journal of Neurophysiology*, *113*(10), 3943–3953. https://doi.org/10.1152/jn.01055.2014

Papagiakoumou, E., Anselmi, F., Bègue, A., de Sars, V., Glückstad, J., Isacoff, E. Y., & Emiliani, V. (2010). Scanless two-photon excitation of channelrhodopsin-2. *Nature Methods*, *7*(10), 848–854. https://doi.org/10.1038/nmeth.1505

Park, A., Yun, T., Hill, T. E., Ikegami, T., Juelich, T. L., Smith, J. K., Zhang, L., Freiberg, A. N., & Lee, B. (2016). Optimized P2A for reporter gene insertion into Nipah virus results in efficient ribosomal skipping and wild-type lethality. *Journal of General Virology*, *97*(4), 839–843. https://doi.org/10.1099/jgv.0.000405

Patterson, G. H., & Piston, D. W. (2000). Photobleaching in two-photon excitation microscopy. *Biophysical Journal*, *78*(4), 2159–2162. https://doi.org/10.1016/S0006-3495(00)76762-2

Polikov, V. S., Tresco, P. A., & Reichert, W. M. (2005). Response of brain tissue to chronically implanted neural electrodes. *Journal of Neuroscience Methods*, *148*(1), 1–18. https://doi.org/10.1016/j.jneumeth.2005.08.015

Potter, S. M., & DeMarse, T. B. (2001). A new approach to neural cell culture for long-term studies. *Journal of Neuroscience Methods*, *110*(1–2), 17–24. https://doi.org/10.1016/S0165-0270(01)00412-5

Quammen, C., Weigle, C., & Taylor II, R. M. (2022). *Boolean operations on surfaces in VTK without external libraries*. The Visualization Toolkit Journal. https://doi.org/10.54294/216g01

Rickgauer, J. P., & Tank, D. W. (2009). Two-photon excitation of channelrhodopsin-2 at saturation. *Proceedings of the National Academy of Sciences*, *106*(35), 15025–15030. https://doi.org/10.1073/pnas.0907084106

Rios, G., Lubenov, E. V., Chi, D., Roukes, M. L., & Siapas, A. G. (2016). Nanofabricated neural probes for dense 3-D recordings of brain activity. *Nano Letters*, *16*(11), 6857–6862. https://doi.org/10.1021/acs.nanolett.6b02673

Ristola, M., Fedele, C., Hagman, S., Sukki, L., Kapucu, F. E., Mzezewa, R., Hyvärinen, T., Kallio, P., Priimagi, A., & Narkilahti, S. (2021). Directional growth of human neuronal axons in a microfluidic device with nanotopography on azobenzene-based material. *Advanced Materials Interfaces*, *8*(11), 2100048. https://doi.org/10.1002/admi.202100048

Rossant, C., Kadir, S. N., Goodman, D. F. M., Schulman, J., Hunter, M. L. D., Saleem, A. B., Grosmark, A., Belluscio, M., Denfield, G. H., Ecker, A. S., Tolias, A. S., Solomon, S., Buzsáki, G., Carandini, M., & Harris, K. D. (2016). Spike sorting for large, dense electrode arrays. *Nature Neuroscience*, *19*(4), 634–641. https://doi.org/10.1038/nn.4268

Rubart, M. (2004). Two-photon microscopy of cells and tissue. *Circulation Research*, *95*(12), 1154–1166. https://doi.org/10.1161/01.RES.0000150593.30324.42

Ruiz-Mejias, M., Ciria-Suarez, L., Mattia, M., & Sanchez-Vives, M. V. (2011). Slow and fast rhythms generated in the cerebral cortex of the anesthetized mouse. *Journal of Neurophysiology*, *106*(6), 2910–2921. https://doi.org/10.1152/jn.00440.2011

Russell, L. E., Dalgleish, H. W. P., Nutbrown, R., Gauld, O. M., Herrmann, D., Fişek, M., Packer, A. M., & Häusser, M. (2022). All-optical interrogation of neural circuits in behaving mice. *Nature Protocols*, *17*(7), 1579–1620. https://doi.org/10.1038/s41596-022-00691-w

Sariev, A., Chung, J., Jung, D., Sharif, F., Lee, J. Y., Kim, S., & Royer, S. (2017). Implantation of chronic silicon probes and recording of hippocampal place cells in an enriched treadmill apparatus. *Journal of Visualized Experiments*, *2017*(128). https://doi.org/10.3791/56438

Saunders, A., Johnson, C. A., & Sabatini, B. L. (2012). Novel recombinant adeno-associated viruses for Cre activated and inactivated transgene expression in neurons. *Frontiers in Neural Circuits*, *6*. https://doi.org/10.3389/fncir.2012.00047

Scheiber, I. F., Mercer, J. F. B., & Dringen, R. (2014). Metabolism and functions of copper in brain. *Progress in Neurobiology*, *116*, 33–57. https://doi.org/10.1016/j.pneurobio.2014.01.002

Schikorski, T., & Stevens, C. F. (1997). Quantitative ultrastructural analysis of hippocampal excitatory synapses. *The Journal of Neuroscience : The Official Journal of the Society for Neuroscience*, *17*(15), 5858–5867. https://doi.org/10.1523/JNEUROSCI.17-15-05858.1997

Schoenenberger, P., Grunditz, Å., Rose, T., & Oertner, T. G. (2008). Optimizing the spatial resolution of Channelrhodopsin-2 activation. *Brain Cell Biology*, *36*(1–4), 119–127. https://doi.org/10.1007/s11068-008-9025-8

Schüz, A., & Palm, G. (1989). Density of neurons and synapses in the cerebral cortex of the mouse. *Journal of Comparative Neurology*, *286*(4), 442–455. https://doi.org/10.1002/cne.902860404

Shaimardanova, A. A., Chulpanova, D. S., Kitaeva, K. V., Abdrakhmanova, I. I., Chernov, V. M., Rutland, C. S., Rizvanov, A. A., & Solovyeva, V. V. (2019). Production and application of multicistronic constructs for various human disease therapies. *Pharmaceutics*, *11*(11), 580. https://doi.org/10.3390/pharmaceutics11110580

Sharp, A. A., Ortega, A. M., Restrepo, D., Curran-Everett, D., & Gall, K. (2009). In vivo penetration mechanics and mechanical properties of mouse brain tissue at micrometer scales. *IEEE Transactions on Biomedical Engineering*, *56*(1), 45–53. https://doi.org/10.1109/TBME.2008.2003261

Sher, A., Chichilnisky, E. J., Dabrowski, W., Grillo, A. A., Grivich, M., Gunning, D., Hottowy, P., Kachiguine, S., Litke, A. M., Mathieson, K., & Petrusca, D. (2007). Large-scale multielectrode recording and stimulation of neural activity. *Nuclear Instruments and Methods in Physics Research Section A: Accelerators, Spectrometers, Detectors and Associated Equipment*, *579*(2), 895–900. https://doi.org/10.1016/j.nima.2007.05.309

Shih, A. Y., Driscoll, J. D., Drew, P. J., Nishimura, N., Schaffer, C. B., & Kleinfeld, D. (2012). Two-photon microscopy as a tool to study blood flow and neurovascular coupling in the rodent brain. *Journal of Cerebral Blood Flow and Metabolism*, *32*(7), 1277–1309. https://doi.org/10.1038/jcbfm.2011.196

Shinozaki, Y., Shibata, K., Yoshida, K., Shigetomi, E., Gachet, C., Ikenaka, K., Tanaka, K. F., & Koizumi, S. (2017). Transformation of astrocytes to a neuroprotective phenotype by microglia via P2Y1 receptor downregulation. *Cell Reports*, *19*(6), 1151–1164. https://doi.org/10.1016/j.celrep.2017.04.047

Shumkova, V., Sitdikova, V., Rechapov, I., Leukhin, A., & Minlebaev, M. (2021). Effects of urethane and isoflurane on the sensory evoked response and local blood flow in the early postnatal rat somatosensory cortex. *Scientific Reports*, *11*(1), 9567. https://doi.org/10.1038/s41598-021-88461-8

Somogyvári, Z., Cserpán, D., Ulbert, I., & Érdi, P. (2012). Localization of single-cell current sources based on extracellular potential patterns: The spike CSD method. *European Journal of Neuroscience*, *36*(10), 3299–3313. https://doi.org/10.1111/j.1460-9568.2012.08249.x

Sony. (2021). *Sony to release large format CMOS image sensor with global shutter function and industry's highest effective pixel count of 127.68 megapixels*. Https://Www.Sony.Com/En/SonyInfo/News/Press/202103/21-021E/. https://www.sony.com/en/SonyInfo/News/Press/202103/21-021E/

Steinmetz, N. (2022). *Data Analysis: Getting Started Tutorial*. https://github.com/cortex-lab/neuropixels/wiki/Other_analysis_methods

Steinmetz, N. A., Aydin, C., Lebedeva, A., Okun, M., Pachitariu, M., Bauza, M., Beau, M., Bhagat, J., Böhm, C., Broux, M., Chen, S., Colonell, J., Gardner, R. J., Karsh, B., Kloosterman, F., Kostadinov, D., Mora-Lopez, C., O'Callaghan, J., Park, J., … Harris, T. D. (2021). Neuropixels 2.0: A miniaturized high-density probe for stable, long-term brain recordings. *Science*, *372*(6539). https://doi.org/10.1126/science.abf4588

Stieglitz, T., Beutel, H., Schuettler, M., & Meyer, J. U. (2000). Micromachined, polyimide-based devices for flexible neural interfaces. *Biomedical Microdevices*, *2*(4), 283–294. https://doi.org/10.1023/A:1009955222114

Sun, Q., Li, X., Ren, M., Zhao, M., Zhong, Q., Ren, Y., Luo, P., Ni, H., Zhang, X., Zhang, C., Yuan, J., Li, A., Luo, M., Gong, H., & Luo, Q. (2019). A whole-brain map of long-range inputs to GABAergic interneurons in the mouse medial prefrontal cortex. *Nature Neuroscience*, *22*(8), 1357–1370. https://doi.org/10.1038/s41593-019-0429-9

Szarowski, D. H., Andersen, M. D., Retterer, S., Spence, A. J., Isaacson, M., Craighead, H. G., Turner, J. N., & Shain, W. (2003). Brain responses to micro-machined silicon devices. *Brain Research*, *983*(1–2), 23–35. https://doi.org/10.1016/S0006-8993(03)03023-3

Takehara, H., Kazutaka, O., Haruta, M., Noda, T., Sasagawa, K., Tokuda, T., & Ohta, J. (2017). On-chip cell analysis platform: Implementation of contact fluorescence microscopy in microfluidic chips. *AIP Advances*, *7*(9), 095213. https://doi.org/10.1063/1.4986872

Taniguchi, H., He, M., Wu, P., Kim, S., Paik, R., Sugino, K., Kvitsani, D., Fu, Y., Lu, J., Lin, Y., Miyoshi, G., Shima, Y., Fishell, G., Nelson, S. B., & Huang, Z. J. (2011). A resource of Cre driver lines for genetic targeting of GABAergic neurons in cerebral cortex. *Neuron*, *71*(6), 995–1013. https://doi.org/10.1016/j.neuron.2011.07.026

Taylor, A. M. (2019). *XonaChip protocol for primary murine neurons*. https://xonamicrofluidics.com/protocols/

Taylor, A. M., Blurton-Jones, M., Rhee, S. W., Cribbs, D. H., Cotman, C. W., & Jeon, N. L. (2005). A microfluidic culture platform for CNS axonal injury, regeneration and transport. *Nature Methods*, *2*(8), 599–605. https://doi.org/10.1038/nmeth777

Taylor, A. M., Dieterich, D. C., Ito, H. T., Kim, S. A., & Schuman, E. M. (2010a). Microfluidic local perfusion chambers for the visualization and manipulation of synapses. *Neuron*, *66*(1), 57–68. https://doi.org/10.1016/j.neuron.2010.03.022

Taylor, A. M., Dieterich, D. C., Ito, H. T., Kim, S. A., & Schuman, E. M. (2010b). Microfluidic Local Perfusion Chambers for the Visualization and Manipulation of Synapses. *Neuron*, *66*(1), 57–68. https://doi.org/10.1016/j.neuron.2010.03.022

Taylor, A. M., Rhee, S. W., Tu, C. H., Cribbs, D. H., Cotman, C. W., & Jeon, N. L. (2003). Microfluidic multicompartment device for neuroscience research. *Langmuir*, *19*(5), 1551–1556. https://doi.org/10.1021/la026417v

Tian, L. (2014). *Fluorescent biosensors for imaging neurotransmitters: observing synapses in action*. National Institute of Health Grantome. https://grantome.com/grant/NIH/DP2-MH107056-01

Tran, T., Sundaram, C. P., Bahler, C. D., Eble, J. N., Grignon, D. J., Francesca Monn, M., Simper, N. B., & Cheng, L. (2015). Correcting the shrinkage effects of formalin fixation and tissue processing for renal tumors: Toward standardization of pathological reporting of tumor size. *Journal of Cancer*, *6*(8), 759–766. https://doi.org/10.7150/jca.12094

Tremblay, R., Lee, S., & Rudy, B. (2016). GABAergic Interneurons in the Neocortex: From Cellular Properties to Circuits. *Neuron*, *91*(2), 260–292. https://doi.org/10.1016/j.neuron.2016.06.033

Wang, H., Huff, T., Zweifel, D., He, W., Low, P. S., Wei, A., & Cheng, J.-X. (2005). In vitro and in vivo two-photon luminescence imaging of single gold nanorods. *Proceedings of the National Academy of Sciences*, *102*(44), 15752–15756. https://doi.org/10.1073/pnas.0504892102

Wang, H., Peca, J., Matsuzaki, M., Matsuzaki, K., Noguchi, J., Qiu, L., Wang, D., Zhang, F., Boyden, E., Deisseroth, K., Kasai, H., Hall, W. C., Feng, G., & Augustine, G. J. (2007). High-speed mapping of synaptic connectivity using photostimulation in Channelrhodopsin-2 transgenic mice. *Proceedings of the National Academy of Sciences*, *104*(19), 8143–8148. https://doi.org/10.1073/pnas.0700384104

Wanger, T., Takagaki, K., Lippert, M. T., Goldschmidt, J., & Ohl, F. W. (2013). Wave propagation of cortical population activity under urethane anesthesia is state dependent. *BMC Neuroscience*, *14*(1), 78. https://doi.org/10.1186/1471-2202-14-78

Welle, E. J., Patel, P. R., Woods, J. E., Petrossians, A., della Valle, E., Vega-Medina, A., Richie, J. M., Cai, D., Weiland, J. D., & Chestek, C. A. (2020). Ultra-small carbon fiber electrode recording site optimization and improved in vivo chronic recording yield. *Journal of Neural Engineering*, *17*(2), 026037. https://doi.org/10.1088/1741-2552/ab8343

Widmann, A., Schröger, E., & Maess, B. (2015). Digital filter design for electrophysiological data – A practical approach. *Journal of Neuroscience Methods*, *250*, 34–46. https://doi.org/10.1016/j.jneumeth.2014.08.002

Yagishita, H., Nishimura, Y., Noguchi, A., Shikano, Y., Ikegaya, Y., & Sasaki, T. (2020). Urethane anesthesia suppresses hippocampal subthreshold activity and neuronal synchronization. *Brain Research*, *1749*, 147137. https://doi.org/10.1016/j.brainres.2020.147137

Yardeni, T., Eckhaus, M., Morris, H. D., Huizing, M., & Hoogstraten-Miller, S. (2011). Retro-orbital injections in mice. *Lab Animal*, *40*(5), 155–160. https://doi.org/10.1038/laban0511-155

Ye, T., He, Y., & Borguet, E. (2006). Adsorption and electrochemical activity: An in situ electrochemical scanning tunneling microscopy study of electrode reactions and potential-induced adsorption of porphyrins. *Journal of Physical Chemistry B*, *110*(12), 6141–6147. https://doi.org/10.1021/jp053358w

Yger, P., Spampinato, G. L., Esposito, E., Lefebvre, B., Deny, S., Gardella, C., Stimberg, M., Jetter, F., Zeck, G., Picaud, S., Duebel, J., & Marre, O. (2018). A spike sorting toolbox for up to thousands of electrodes validated with ground truth recordings in vitro and in vivo. *ELife*, *7*. https://doi.org/10.7554/eLife.34518

Yi, G. S., Wang, J., Tsang, K. M., Wei, X. Le, & Deng, B. (2015). Biophysical insights into how spike threshold depends on the rate of membrane potential depolarization in Type I and Type II neurons. *PLoS ONE*, *10*(6), e0130250. https://doi.org/10.1371/journal.pone.0130250

Yoder, E. J. (2002). In vivo microscopy of the mouse brain using multiphoton laser scanning techniques. *Multiphoton Microscopy in the Biomedical Sciences II*, *4620*, 14–29. https://doi.org/10.1117/12.470705

Young, E. W. K., Berthier, E., & Beebe, D. J. (2013). Assessment of enhanced autofluorescence and impact on cell microscopy for microfabricated thermoplastic devices. *Analytical Chemistry*, *85*(1), 44–49. https://doi.org/10.1021/ac3034773

Zhang, F., Gradinaru, V., Adamantidis, A. R., Durand, R., Airan, R. D., De Lecea, L., & Deisseroth, K. (2010). Optogenetic interrogation of neural circuits: Technology for probing mammalian brain structures. *Nature Protocols*, *5*(3), 439–456. https://doi.org/10.1038/nprot.2009.226

Zhao, S., Ting, J. T., Atallah, H. E., Qiu, L., Tan, J., Gloss, B., Augustine, G. J., Deisseroth, K., Luo, M., Graybiel, A. M., & Feng, G. (2011). Cell type–specific channelrhodopsin-2 transgenic mice for optogenetic dissection of neural circuitry function. *Nature Methods*, *8*(9), 745–752. https://doi.org/10.1038/nmeth.1668

Zheng, D., Pisano, F., Collard, L., Balena, A., Pisanello, M., Spagnolo, B., Mach-Batlle, R., Tantussi, F., Carbone, L., De Angelis, F., Valiente, M., de la Prida, L. M., Ciracì, C., De Vittorio, M., & Pisanello, F. (2023). Toward plasmonic neural probes: SERS detection of neurotransmitters through gold-nanoislands-decorated tapered optical fibers with sub-10 nm gaps. *Advanced Materials*, 2200902. https://doi.org/10.1002/adma.202200902